Measurements and Computational Analysis of the Turbulent Corner Flow on the NASA Juncture-Flow Model with a Symmetric Wing

Michael A. Kegerise, Andrew N. Leidy, Judith A. Hannon, and Christopher L. Rumsey
Langley Research Center, Hampton, Virginia

NASA STI Program Report Series

Since its founding, NASA has been dedicated to the advancement of aeronautics and space science. The NASA scientific and technical information (STI) program plays a key part in helping NASA maintain this important role.

The NASA STI program operates under the auspices of the Agency Chief Information Officer. It collects, organizes, provides for archiving, and disseminates NASA's STI. The NASA STI program provides access to the NTRS Registered and its public interface, the NASA Technical Reports Server, thus providing one of the largest collections of aeronautical and space science STI in the world. Results are published in both non-NASA channels and by NASA in the NASA STI Report Series, which includes the following report types:
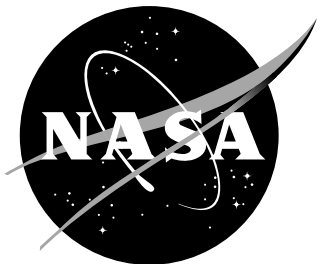
- TECHNICAL PUBLICATION. Reports of completed research or a major significant phase of research that present the results of NASA Programs and include extensive data or theoretical analysis. Includes compilations of significant scientific and technical data and information deemed to be of continuing reference value. NASA counterpart of peer-reviewed formal professional papers but has less stringent limitations on manuscript length and extent of graphic presentations.

- TECHNICAL MEMORANDUM. Scientific and technical findings that are preliminary or of specialized interest, e.g., quick release reports, working papers, and bibliographies that contain minimal annotation. Does not contain extensive analysis.

- CONTRACTOR REPORT. Scientific and technical findings by NASA-sponsored contractors and grantees.

- CONFERENCE PUBLICATION. Collected papers from scientific and technical conferences, symposia, seminars, or other meetings sponsored or co-sponsored by NASA.

- SPECIAL PUBLICATION. Scientific, technical, or historical information from NASA programs, projects, and missions, often concerned with subjects having substantial public interest.

- TECHNICAL TRANSLATION. English-language translations of foreign scientific and technical material pertinent to NASA's mission.

Specialized services also include organizing and publishing research results, distributing specialized research announcements and feeds, providing information desk and personal search support, and enabling data exchange services.

For more information about the NASA STI program, see the following:

- Access the NASA STI program home page at http://www.sti.nasa.gov

- Help desk contact information:

https://www.sti.nasa.gov/sti-contact-form/
and select the "General" help request type.

NASA/TP–20240004000

Measurements and Computational Analysis of the Turbulent Corner Flow on the NASA Juncture-Flow Model with a Symmetric Wing

Michael A. Kegerise, Andrew N. Leidy, Judith A. Hannon, and Christopher L. Rumsey
Langley Research Center, Hampton, Virginia

April 2024

Abstract

The NASA Juncture Flow Experiment is designed to acquire high-quality flowfield data deep in the corner of a wing-fuselage junction for the purpose of computational fluid dynamics (CFD) validation and turbulence model improvement. This report presents and discusses the results of a recent experiment with the Juncture Flow Model in the NASA Langley 14- by 22-Foot Subsonic Tunnel. The main objective of the test was to expand the existing juncture-flow dataset with a symmetric wing case that displays fully attached, incipient separation, and separated flow in the corner of the wing-fuselage junction, depending on the model angle of incidence. Laser Doppler velocimetry (LDV) measurements were made at three model angles of incidence ($0°$: fully attached, $1°$: incipient separation, and $5°$: separated flow) and for each angle, mean-flow and Reynolds-stress data were obtained on the fuselage and at several locations along the corner of the wing-fuselage junction. Supporting measurements were made during the test campaign and include model and tunnel wall static pressures, tunnel wall boundary-layer profiles, oil-flow visualizations, and laser-based measurements of the as-built model geometry and model position in the test section. A companion set of Reynolds-averaged Navier-Stokes (RANS) CFD simulations were also performed and those results were used to support the discussion of the experimental test results.

1

Contents

Nomenclature

b	model half span, 1663.5 mm
c	chord length at wing planform break, 580.716 mm
c_f	skin-friction coefficient
C'	14x22 facility calibration function
C_p	surface pressure coefficient
c_r	chord length at wing root, 1052.8 mm
H	boundary layer shape factor
i	ith sample or ith component
k	turbulent kinetic energy, m^2/s^2
K_{pr}	pitot loss coefficient, 0.998
ℓ_v	viscous length scale, μm
M	Mach number
N	number of samples
p	pressure, Pa
p'	fluctuating pressure, Pa
q	dynamic pressure, Pa
R_a	roughness average, μm
Re_c	Reynolds number based on chord length at wing planform break
Re_θ	Reynolds number based on momentum thickness
R_q	roughness rms, μm
T_a	ambient temperature, K
U_{ref}	reference velocity, m/s
U_i	(U_1, U_2, U_3) Cartesian velocity components (U, V, W), m/s
u'_i	(u_1, u_2, u_3) velocity fluctuation (u, v, w), m/s
u_τ	friction velocity, m/s
x_i	(x_1, x_2, x_3) Cartesian coordinates (x, y, z), m (mm where noted)
x_{LE}	x location of the wing root leading edge, mm
$\hat{x}$	non-dimensional distance along wing root, $(x - x_{LE})/c_r$
y_o	y location of the fuselage surface, mm
α	angle of incidence, deg
δ	boundary-layer thickness, mm
δ^*	displacement thickness, mm
θ	momentum thickness, mm
ν	kinematic viscosity, m^2/s
ν_T	turbulent or eddy viscosity, m^2/s
Π	wake-strength parameter
ρ	density, kg/m^3
τ_i	particle transit time through the measurement volume for the ith sample, s
ψ	mean flow angle or surface angle, deg
ω_i	$(\omega_1, \omega_2, \omega_3)$ Cartesian vorticity components $(\omega_x, \omega_y, \omega_z)$, s^{-1}
$\langle \cdot \rangle$	mean value

Subscripts

EC	entrance cone
SC	settling chamber
t	total condition
TS	test section
∞	freestream condition

List of Tables

List of Figures

1 Introduction

Junction flows, such as those formed around a wing-fuselage or a wing-pylon intersection, often exhibit regions of flow separation that can adversely impact aircraft performance. For wing-fuselage junction flows, separation in the turbulent corner-flow region near the wing trailing edge can impact the maximum lift coefficient and may also significantly modify the stall characteristics of an aircraft [1]. As such, there is a strong desire to predict the onset and progression of separation reliably and accurately for this flow, but that remains a challenge for computational fluid dynamics (CFD) methods. To address this challenge, NASA has developed a CFD validation experiment for a generic full-span wing-fuselage junction model that experiences corner-flow separation at subsonic flow conditions [2–5]. In the present context, "CFD validation experiment" refers to the overall combined CFD/experimental effort necessary to produce validation-quality data [6]. A primary goal of this effort was to provide high-quality flowfield data in the turbulent corner-flow region of the junction suitable for CFD validation and turbulence model improvements. To that end, significant resources were also focused on the collection of data for boundary conditions, model geometry, and uncertainty quantification—all of which allow for an unambiguous comparison of the flowfield data to the CFD simulations.

Two test campaigns with the NASA Juncture Flow (JF) model were previously conducted in the NASA Langley 14- by 22-Foot Subsonic Tunnel (14x22) [3, 5]. There, the JF model was configured with a truncated F6 wing, which is a cambered wing design for a generic twin engine wide body aircraft [7]. This configuration experienced corner-flow separation near the trailing edge of the wing-fuselage junction, with the onset location moving upstream with increasing model angle of incidence. Furthermore, corner-flow separation occurred for all angles of incidence considered, from $-10°$ to $+10°$. During these test entries, mean velocity and turbulent flowfield data were collected at selected locations on the model fuselage and in the corner-flow region of the wing-fuselage junction using internally mounted laser Doppler velocimetry (LDV) systems. These LDV systems afforded velocity measurements with high-accuracy and high spatial resolution and allowed for measurements very near to the model surfaces. A complementary set of flowfield data in the corner-flow region was also collected with an internally mounted particle image velocimetry (PIV) system [5,8]. That PIV system afforded instantaneous snapshots of the corner flowfield, albeit at lower accuracy and lower spatial resolution and further away from the model surfaces as compared to the LDV measurements. In addition to the flowfield measurements, static and dynamic pressures were measured at selected locations on the model, infrared imaging was used to characterize boundary-layer transition, and oil flow was used to visualize the separated flow in the corner-flow region of the wing-fuselage junction. The as-built geometry and position of the model in the test section were measured via laser-based scanning techniques over the course of both test entries. Boundary conditions in the form of tunnel-wall pressures, diffuser pressures, and boundary-layer rake pressures were acquired and in an earlier test entry in the 14x22, the test section inflow conditions were documented using various measurement techniques [9]. All of the data from these test campaigns are available on the NASA Langley Turbulence Modeling Resource (TMR) website [10].

Comparisons with our JF measurements to date have shown that Reynolds-averaged Navier-Stokes (RANS) CFD methods used in conjunction with a linear eddy viscosity turbulence model tend to dramatically overpredict the size of the corner-flow separation. This is primarily due to the inability of linear turbulence models to correctly predict the anisotropy in the turbulent Reynolds normal-stress components in the corner-flow region. That anisotropy is responsible for the production of streamwise vorticity in the corner-flow region [11], which in our case acts to delay the onset of corner-flow separation. RANS CFD methods used in conjunction with nonlinear eddy viscosity models—such as Spalart-Allmaras (SA) with rotation-curvature (RC) correction and the quadratic constitutive relation (QCR2000 or QCR2013)—fared far better, but still overpredicted the size of the corner-flow separation by approximately 30%. As a direct result of comparisons between the JF flowfield measurements and RANS CFD methods, an improved version of the quadratic constitutive relation—QCR2020—was developed and this was found to provide better predictions of the

normal-stress anisotropy and consequently, better predictions for the onset of corner-flow separation on the JF configuration [5, 12].

The desired objective of the JF CFD validation experiment was to test the juncture-flow model with a single wing configuration that displayed a progression from fully attached corner flow to a large corner-flow separation with increasing model angle of incidence. Early in the project, risk-reduction tests in the Virginia Tech Stability Tunnel [13] and the 14x22 [14] were performed on smaller-scale models with several wing candidates, but none of them were found to display the desired behavior. The F6-based wing design did display a large corner-flow separation, but separation occurred for all the angles of incidence that were considered. A second wing configuration with a symmetric profile (based on NACA four-digit wing sections) did display a progression from fully attached corner flow to separated corner flow, but the size of the separated flow region remained very small. Since neither wing design was optimal in terms of our original goal, a decision was made to build both the F6 wing and the symmetric wing for the CFD validation experiment so that data for fully attached, incipient, and separated corner flow could be obtained.

As noted earlier, the F6 wing was the subject of two previous test entries in the 14x22. Recently, a third test campaign was conducted in the 14x22 with the symmetric wing configuration and similar to the previous test entries, the primary objective was to obtain flowfield data in the turbulent corner-flow region of the wing-fuselage junction. With this new configuration, the juncture-flow data set is expanded to include fully attached and incipient separation cases that can be used for the assessment of turbulence models at conditions near separation onset. A secondary objective was to quantify the natural transition location on the fuselage and wing surfaces. In this paper, we present the details of the third test entry related to the primary objective, present sample test results, and discuss the flow physics pertinent to these test results. A companion set of RANS CFD simulations using the SA-RC-QCR2020 turbulence model were also performed, and those results will be used to support the discussion of the experimental test results. The test details and results associated with measurements of natural transition on the JF model are reported separately in Leidy et al. [15].

2 Experimental details

2.1 Wind-tunnel facility

The experiment was conducted in the Langley 14- by 22-Foot Subsonic Tunnel which is a closed-circuit, atmospheric-pressure wind tunnel capable of operating in an open, partially closed, or closed test-section mode. Raising and lowering the north (port) and south (starboard) walls and ceiling creates the various modes of tunnel operation. Measurements for this study were made with the test section in the closed-wall configuration, resulting in a test section measuring 4.42 m high, by 6.63 m wide, by 13 m long, with a maximum free-stream velocity of 103 m/s. Flow conditioning is provided by a flow-straightening honeycomb, four square-mesh screens with a mesh count of 10 per inch and 64% open area[1], and a tunnel contraction ratio of 9 to 1. This arrangement achieves a low test-section turbulence intensity of between 0.07 and 0.08% at a dynamic pressure of 2.87 kPa—but that does vary somewhat with dynamic pressure and location in the test section [17]. Further details about the tunnel can be found in Gentry et al. [16].

Throughout all of the wind-tunnel runs, the tunnel controller held the chord Reynolds number, Re_c, at a constant value of 2.4 million to within ± 0.05 million. Since the facility does not have a temperature controller, the air temperature increased over the course of a given run due to viscous heating and therefore, the velocity was increased accordingly to maintain a constant Re_c. In addition, there were substantial changes in the nominal air temperature from day-to-day and over the course of the test entry due to prevailing outdoor conditions. As such, the nominal tunnel velocity

---

[1]It should be noted that Gentry et al. [16] reported that the 14x22 was configured with four progressively finer screens, with mesh counts of 15 to 25 per inch and open areas of 67% to 70%. In the late 1990s, those screens were replaced with the ones reported here.

Table 1: Nominal test conditions and associated ranges.

	Nominal value	Uncertainty	Range
Re_c	$2.4 \cdot 10^6$	$\pm 0.05 \cdot 10^6$	$[2.39, 2.41] \cdot 10^6$
M	0.189	± 0.002	$[0.171, 0.199]$
T_a, K	288.84	± 0.20	$[281, 309]$
U_{ref}, m/s	64.4	± 0.6	$[57.5, 69.9]$
q_∞, Pa	2385	± 47	$[2071, 2725]$

was again adjusted to maintain the target Re_c. The nominal test conditions for other freestream parameters of interest and their associated ranges over the course of the test entry are shown in Table 1. Here, the freestream Mach number (M), velocity (U_{ref}), and dynamic pressure (q_∞) are based on an empty test-section calibration, which was performed with a stand-mounted pitot-static probe located 5.41 m from the test-section inlet and on the test-section centerline [18].

As part of the validation experiment, several characteristics of the wind-tunnel facility were measured to assist in the creation of a computational model of the wind tunnel for use in CFD simulations of the juncture-flow experiment. These measurements include: 1) Geographic Information System (GIS) laser scans of the wind tunnel high speed leg (contraction, test section, and diffuser) with an associated CAD model, 2) static pressures along the length of the test-section side walls and ceiling, 3) boundary-layer rake measurements on the north and south walls and ceiling at a streamwise location upstream of the model, and 4) an inflow planar survey of the empty tunnel with a 5-hole probe that yielded the total-pressure distributions at a streamwise location 1.615 m downstream of the test-section inlet [9]. Further details on these facility measurements, along with the data sets (excluding item 4), can be found on the Turbulence Modeling Resource (TMR) website [10].

2.2 Juncture-flow model

The JF model is a full-span wing-fuselage body with a modular design that can be configured with different fuselage nose sections and different wing designs. In addition, each wing design has a removable leading-edge insert at the root that allows the wing to be configured with or without a leading-edge root extension that mitigates the leading-edge horseshoe vortex of the wing-fuselage junction. The fuselage has flat side walls with six locations for instrumentation inserts (three on each flat side of the fuselage) that provide access to the fuselage nose section boundary layer, the fuselage boundary layer near the wing leading edge, and the wing-fuselage corner flow. For this test entry, the inserts were configured with either static-pressure ports or thin (1 mm) antireflection coated acrylic windows that provided optical access for the LDV probes stowed within the model. Removable hatches on the top and bottom of the model fuselage provided access to the internal model instrumentation. All of the model parts were painted with a black lusterless polyurethane paint suitable for both infrared imaging and oil-flow visualizations on the model surface. The average roughness, R_a, and the rms roughness, R_q, for the painted model surface was 2.70 ± 0.94 μm and 3.33 ± 1.12 μm, respectively.

For the present study, the JF model was configured with the shorter of two available fuselage nose sections (to date, the longer nose has not been used in any test), and symmetric wings with leading-edge root extensions. A top and side view of the model geometry for this configuration is shown in figure 1. The symmetric wing design is a gradual blending of an NACA 0015 section at the root, an NACA 0012 section at the wing break, and an NACA 0010 section at the wing tip. The wing has a leading-edge sweep angle of 37.3° and a planform break located 869.7 mm from the model centerline. The as-designed planform break chord length, c, was 580.716 mm and this was used as the reference length for Re_c. The overall length, height and width of the fuselage for this configuration was 4.839 m, 0.630 m, and 0.472 m, respectively, and the tip-to-tip wing span was
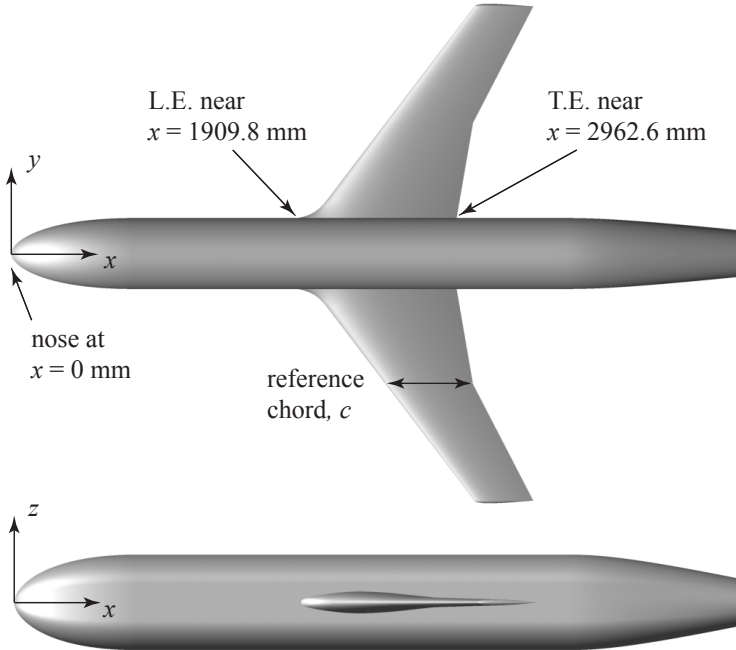
Figure 1: Top and side views of the wing-fuselage junction model geometry.

3.327 m. A port-side view of the model installed in the 14x22 is shown in figure 2 [2]. Here, we see that the model is attached—via a long sting cannon—to a motorized sting mast that allows for adjustments to the model pitch and yaw angles, as well as the model height. The height adjustment allows for a reference point on the model (located 2.448 m from the model nose tip and on the fuselage centerline) to be kept near the center of the test section during a pitch-angle adjustment. In addition, the sting cannon was motorized for adjustments to the model roll angle. Both the pitch and roll angles were measured with a pair of accelerometer-based model-attitude sensors located inside the model fuselage, and both sensors had an accuracy of $\pm 0.01°$. Further details on the model-attitude sensors can be found in Finley and Tcheng [19].

The as-built, as-tested geometry of the JF model was measured with a portable laser-based coordinate measuring machine with a reported accuracy of less than 0.1 mm. In addition, lower fidelity GIS laser scans of the JF model, the sting, and the sting-mast positions in the tunnel were performed for the model angles of incidence at which LDV data were acquired. The latter information can be used for in-tunnel CFD simulations of the juncture-flow experiment. The laser-scan data and a general discussion of it can be found on the TMR website [10].

To ensure a turbulent boundary layer on the fuselage and wing surfaces, commercially-produced trip-dot tape was used to fix the transition location. The trip dots were cylindrical with a diameter of 1160 μm and a center-to-center spacing of 2470 μm. On the fuselage, trip dots with a height of 289.4 μm were placed at a nominal distance of $x = 336$ mm from the fuselage nose tip. On the upper and lower wing surfaces, trip dots with a height of 218.4 μm were placed along the wing span at an arc distance from the leading edge equal to 6.4% of the local chord length. A second row with a height of 205.7 μm was placed on the outer 75% of the wing span at 1.6% of the local chord length. That row was used to eliminate a laminar leading edge separation bubble that was observed for model angles of incidence greater than $7°$. Images of the trip dots on the JF model are

---

[2]Considering the pilot's view, port refers to the left side of the model, while starboard refers to the right side of the model.

Figure 2: Port-side view of the wing-fuselage junction model installed in the 14- by 22-Foot Subsonic Tunnel.

shown in figure 3. Transition to turbulent flow via the trip-dot arrays was confirmed with infrared imaging of the model surfaces over angles of incidence ranging from $-10°$ to $+10°$. As an example
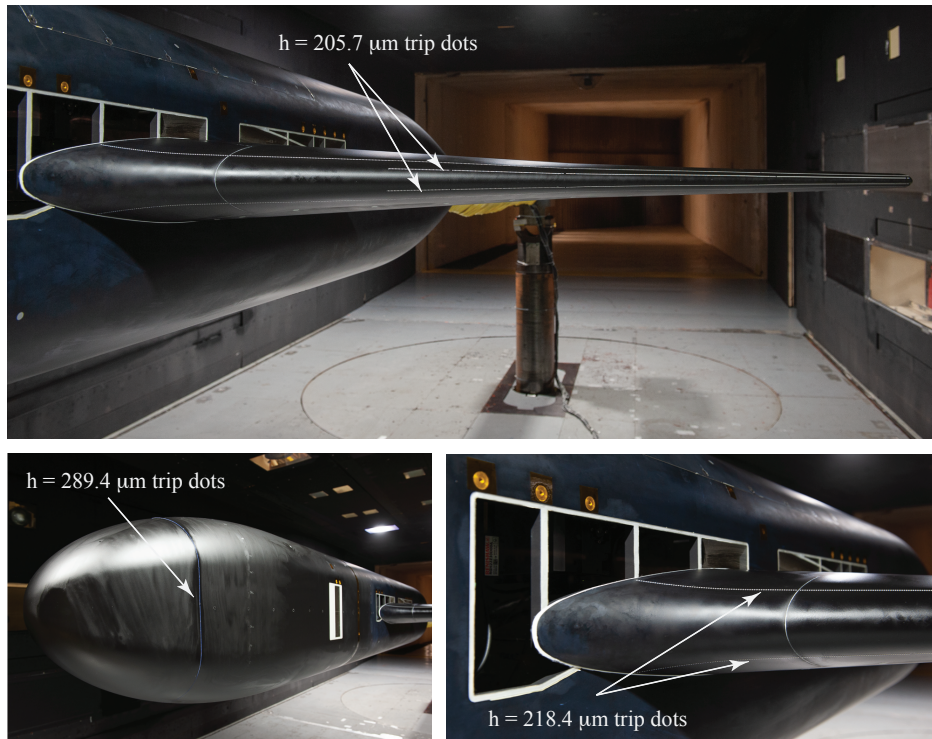
Figure 3: Images of the boundary-layer trip dots on the JF model fuselage and wing surfaces.
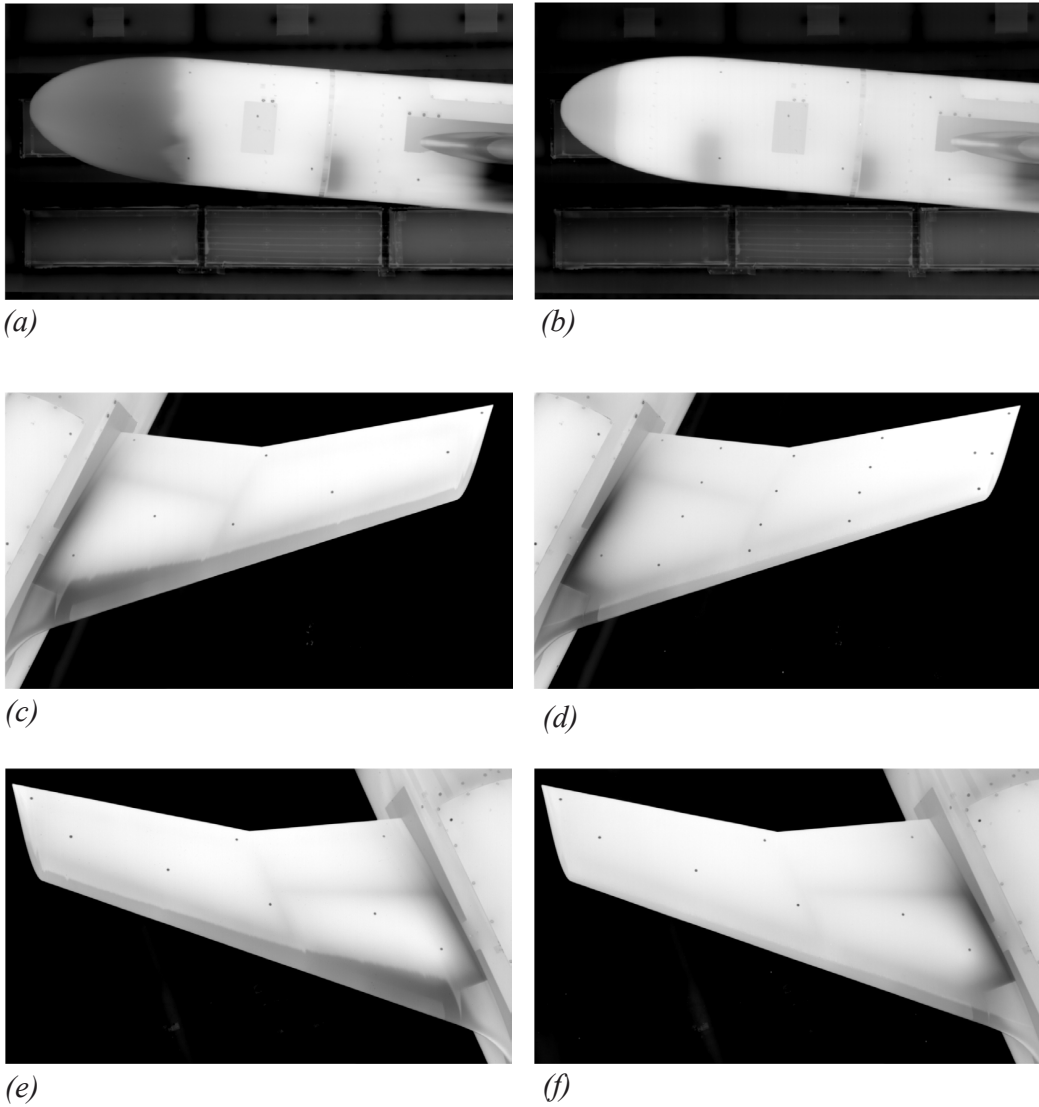
Figure 4: Infrared images of the juncture-flow model at $\alpha = 5°$, with and without boundary layer trip dots. (*a, c, e*) fuselage nose, port wing, and starboard wing without trip dots. (*b, d, f*) fuselage nose, port wing, and starboard wing with trip dots applied.

of that confirmation, infrared images of the fuselage nose (port side), the upper surface of the port wing, and the upper surface of the starboard wing for baseline (no trip dots, natural transition) and tripped conditions at $\alpha = 5°$ are shown in figure 4. When these images were acquired, the air temperature was higher than the model surface temperature. In that case, the darker image tones are associated with lower surface temperatures and indicate laminar flow, while the lighter image tones are associated with higher surface temperatures and indicate turbulent flow. The infrared images for tripped conditions (figure 4b, d, and f) display an abrupt jump in the surface temperature at the trip-dot locations, indicating that transition to turbulent flow is fixed at those locations.

14

2.3   Oil-flow visualizations

Oil-flow visualizations were performed near the trailing edge of the wing-fuselage junction and these were used to determine the model angles of incidence at which the corner flow was fully attached, near incipient separation, or separated. For the separated flow case, approximate measurements of the length and width of the corner-flow separation were used to guide the selection of spatial locations for flowfield measurements with the LDV system. The oil-flow material was a mixture of 1 part titanium dioxide (TiO_2), 2 parts kerosene, and 0.3 parts oleic acid, applied to the model with foam paint brushes. A live video feed was used to monitor the oil-flow development as the tunnel was ramped up to the desired chord Reynolds number of 2.4 million. The ramp-up time was typically less than 1 minute, and once on condition, the tunnel was run for several minutes until no motion of the oil-flow material was observed. Post-run images of the oil-flow patterns were acquired with a 12 megapixel digital SLR camera.

2.4   Static-pressure measurements

The JF model was instrumented with 244 static pressure ports on the fuselage and 289 static pressure ports on the symmetric wings[3]. Electronically scanned pressure (ESP) modules, which were stowed in the JF model, were used to measure the mean pressure at each port. The full-scale range of the differential-pressure modules was 6.89 kPa (1psi) or 34.47 kPa (5 psi) depending on the expected pressure range of the ports connected to the module, and the modules were pneumatically referenced to the ambient pressure in the control room of the 14x22 for stability. As noted in Section 2.1, additional mean pressure measurements were made at static pressure ports on the ceiling, the port-side wall, and the starboard-side wall of the test section. The mean total pressures from a set of boundary-layer rakes mounted to the ceiling, the port-side wall, and the starboard-side wall were also acquired. The static pressure data were collected for model angles of incidence ranging from $-10°$ to $+10°$ in $2.5°$ increments, and with the model both upright and inverted. An additional set of static pressure data was collected with the model at $1°$ angle of incidence, but only for the upright position. Given the port-starboard and top-bottom symmetry of the JF model, the fuselage static pressures from the port and starboard sides were combined into a single one-sided data set for each angle of incidence. Similarly for the wing, the port and starboard side data, along with the upright and inverted data, were combined into a single one-sided data set. For these combined data sets, the effects of any flow nonuniformity, flow angularity, and model geometric differences on the measurement uncertainty were captured. Note that the static pressure data on the JF model were not corrected for wall effects and do not include flow-angularity corrections.

In the standard data-reduction routines for the 14x22, the static-pressure coefficients, C_p, are based on a calibrated freestream dynamic pressure, q_∞, and the freestream static pressure, p_∞. The aforementioned calibrated dynamic pressure is based on an empty-tunnel calibration with a stand-mounted pitot-static probe located on the tunnel centerline, 5.41 m from the test-section inlet. As discussed in Carlson [20], the freestream dynamic pressure is calculated as:

$$q_\infty = C'\ K_{pr}\ q_{indicated} \tag{1}$$

where C' is the calibration coefficient, K_{pr} is a pitot-static probe loss coefficient, and

$$q_{indicated} = p_{t,SC} - p_{EC}. \tag{2}$$

Here, $p_{t,SC} - p_{EC}$ it the measured pressure difference between the total pressure in the settling chamber and the static pressure in the entrance cone. The freestream static pressure is then calculated as:

$$p_\infty = p_{t,SC} - q_\infty. \tag{3}$$

---

[3]The locations of the static pressure ports can be found in the data files that are available through the NASA TMR website [10].

15

Further details on the data-reduction procedure for 14x22 can be found in Carlson [20]. It should be noted, however, that there is a small deficit between the total pressure measured in the settling chamber and the total pressure measured at the calibration location. To account for that, the empty tunnel calibration data was used to develop an empirical relation for the total pressure deficit as a function of $q_{indicated}$:

$$p_{t,SC} - p_{t,TS} = f(q_{indicated}) \qquad (4)$$

where $p_{t,TS}$ is the total pressure at the stand-mounted pitot-static probe. With that, the freestream static pressure was calculated as:

$$p_\infty = [p_{t,SC} - f(q_{indicated})] - q_\infty. \qquad (5)$$

In applying this correction for the total-pressure deficit, it was assumed to be constant across the span of the model, even though that may not be strictly correct. Nevertheless, the resulting difference in C_p between the standard data-reduction (using equation 3) and the modified one used here (using equation 5) is +0.018. On the model wings, this C_p difference is hardly noticeable, but it is important for C_p values near zero, such as on the model fuselage and the tunnel walls. The upshot of the modified data reduction is improved accuracy in the C_p measurements and better agreement between the experimental data and CFD.

2.5 Laser Doppler velocimetry measurements

Flowfield velocity measurements were made with a pair of miniature laser Doppler velocimetry (LDV) probes that were located inside the junction model, and each probe was mounted to a three-axis traverse system. One LDV probe was located near the wing trailing edge and was used to survey the wing-fuselage corner flow. The other LDV probe was alternately used to survey the boundary layer on the fuselage nose section, the fuselage boundary layer in the vicinity of the wing leading edge, and the wing-fuselage corner flow near the wing leading edge.

The LDV systems are a custom design comprised of a photonics system that provides laser light, a fiber-optic-based probe head with off-axis receiving optics, photomultipliers to detect Doppler bursts, and a data acquisition computer with a high-speed A/D board and burst-processing software. Details of this system were previously reported in Kegerise et al. [3], so only the salient features of the system are listed here. The LDV probe emits seven laser beams, five at a wavelength of 532 nm (green) and two at a wavelength of 488 nm (blue). The five green beams form three overlapping, frequency-shifted (-80, -200, and 350 MHz) measurement volumes with nominal diameter and length of 140 μm and 960 μm, respectively, at a working distance of 90 mm. The measurement directions defined by these three measurement volumes are nonorthogonal and depend on the probe-head orientation inside the model. Therefore, a linear transformation was developed to convert the measured velocity components to those in the orthogonal body-fixed coordinate system (as defined in figure 1). To that end, each of the beam unit vectors were measured in situ and then used to calculate the measurement directions, the measurement volume fringe spacings, and the linear transformation.

The two blue beams form a frequency shifted (-200 MHz) measurement volume with a converging set of fringes along their bisector that overlaps the green beam measurement volumes. Using the Doppler-shifted frequency measured with this measurement volume and the velocity measured by the green beam measurement volumes (which have a uniform fringe spacing), the local fringe spacing of the blue beam measurement volume can be calculated. Then, using a simple linear model for the converging fringe pattern and the calculated fringe spacing, the position of the particle along the bisector of the measurement volume is calculated. When performing these calculations, only coincident data (i.e., from the same particle) measured with the blue- and green-beam measurement volumes is considered. A key advantage of this capability is that the particle positions can be used to achieve submeasurement-volume spatial resolution. Details on the theory and development of this particle-position-resolving capability can be found in Lowe [21, 22] and Brooks and Lowe [23].

16

Scattered light from the measurement volume was collected with a 110 mm focal length lens oriented at approximately $35°$ to the optical axis of the probe head and subsequently focused onto a multimode fiber with a diameter of 105 μm. With this off-axis arrangement, the effective length of the measurement volumes was approximately 180 μm.[4] The multimode fiber was then connected to a pair of photomultipliers (PMTs), each fitted with a filter that passed either green or blue wavelengths. The amplified signals from the PMTs were sampled with an 8 bit, 1 GHz sample rate data acquisition card. Burst detection for each channel was performed in the time domain and Doppler-shifted frequencies were extracted from the power-spectral densities of the sampled burst signals. Specific details on the burst-processing algorithm can be found in Lowe [21]. For the blue channel burst signals, a single Doppler-shifted frequency associated with the measurement volume was present, while for the green channel burst signals, three Doppler-shifted frequencies—associated with the three measurement volumes—were present when coincidence was satisfied. For the green channel, the frequency shift for each measurement volume was separated far enough apart in the frequency domain so that no signal ambiguity could occur for our flow conditions.

Seeding for the LDV measurements was provided by a smoke generator that uses a low-residue mineral oil and produces a narrow distribution of particle sizes with a nominal diameter of 0.94 μm. The smoke generator was placed in the wind tunnel settling chamber ahead of the honeycomb and was operated continuously during a wind-tunnel run so that adequate burst data rates were achieved. Depending on where the measurement volume was located in the flowfield, validated (i.e., coincidence was satisfied) burst data rates on the order of 100 to 500 bursts/s were typically observed.

For each spatial location in a flowfield survey, a fixed number of validated Doppler bursts were sampled and the measured Doppler-shifted frequencies from the three measurement volumes formed by the five green laser beams were used to calculate three nonorthogonal velocity components. The histograms of those velocity components were then calculated and the histogram-clipping routine of Ölçmen and Simpson [24] was applied for removal of noise and outliers. The nonorthogonal velocity components were then transformed to orthogonal velocity components in the body-fixed coordinate system. Histograms of those components were calculated and once again, the histogram-clipping routine was applied. The processed velocity samples—which were sampled with random spacing in time—were then used to calculate several statistical moments. To account for velocity bias effects on the statistical moments, each sample was weighted by the particle transit time (or burst duration, which was recorded by the burst processor for each sample) through the measurement volume [25]. With this weighting factor, the mean x component of velocity was calculated as:

$$\langle U \rangle = \frac{\sum_i^N U_i \tau_i}{\sum_i^N \tau_i}, \tag{6}$$

where U_i is the instantaneous x component of velocity for a given sample i, τ_i is the transit time for a given sample i, and N is the total number of samples. Similar equations were used to calculate the mean y component, $\langle V \rangle$, and the mean z component, $\langle W \rangle$, of velocity. The Reynolds-stress components were calculated as:

$$\langle uv \rangle = \frac{\sum_i^N \left(U_i - \langle U \rangle\right)\left(V_i - \langle V \rangle\right)\tau_i}{\sum_i^N \tau_i}, \tag{7}$$

where U_i and τ_i are as defined above, and V_i is the instantaneous y component of velocity for a given sample i. Similar relations were defined for the other five independent components of Reynolds stress: $\langle u^2 \rangle$, $\langle v^2 \rangle$, $\langle w^2 \rangle$, $\langle uw \rangle$, and $\langle vw \rangle$. Strictly speaking, the Reynolds-stress tensor is defined by $R_{ij} \equiv -\langle \rho u_i u_j \rangle$. In the literature, however, the velocity correlation, $\langle u_i u_j \rangle$, is often referred to as the Reynolds stress, with $\langle u_i u_j \rangle \approx -R_{ij}/\langle \rho \rangle$, for subsonic flow. Here, we adopt this naming

---

[4]As a point of reference, this is approximately 25 times the viscous length scale for the turbulent boundary layer on the fuselage nose section.
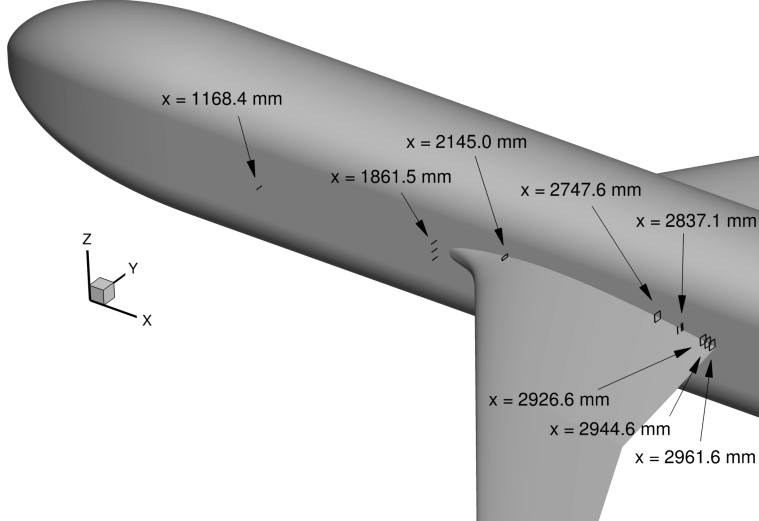
Figure 5: LDV measurement locations on the fuselage and in the wing-fuselage junction region.

convention. In addition, for the presentation of the mean-velocity and Reynolds-stress components in the results section, U_{ref} is used for nondimensionalization. Typically, 15,000 samples were used to calculate the statistical moments and for the data rates that were achieved (100 to 500 samples/s), many of the samples were statistically independent, being separated in time by at least two times the integral time scale [25]. The number of samples collected was also found to be more than sufficient to obtain well-converged statistical moments.

Most of the LDV measurements were made with the LDV probes operated solely with the five green laser beams to obtain velocity measurements. For measurements on the fuselage nose section however, the LDV probe was operated with all seven lasers beams to measure both velocity and particle position. In that case, the measurement volume bisector was oriented normal to the fuselage window surface so that particle positions were measured in that direction. By making a series of closely-spaced and overlapping measurements in the wall-normal direction, a composite point cloud of particle position versus velocity was formed. The particle positions and associated velocity components were then divided into bins along the wall-normal direction, each with a width of 50 μm, and statistical moments for the samples in each bin were calculated. This approach allowed for finer spatial resolution in the near-wall region of the fuselage boundary layer.

For a given model angle of incidence, LDV data were collected at several x locations on the port side of the JF model as depicted in figure 5. On the fuselage, data were collected during wall-normal surveys at selected (x,z) locations. In the wing-fuselage corner region, data were primarily collected during (y,z) planar surveys, an example of which is shown in figure 6. Here, the planar survey consisted of 420 measurement locations, with grid spacings ranging from 0.5 mm to 2 mm. Repeat (or replicate) measurements at all x locations were performed to aid in the development of uncertainty estimates. Three model angles of incidence were considered for the LDV measurements: $0°$, $1°$, and $5°$, which correspond to fully attached, incipient, and separated corner flow as determined via oil-flow visualization (see section 4.1 for details).

The uncertainties in the instantaneous velocity components derived from the LDV measurements were estimated to be $\delta U = 0.0065\|\vec{U}\|$, $\delta V = 0.0295\|\vec{U}\|$, and $\delta W = 0.0079\|\vec{U}\|$, where $\|\vec{U}\|$ is the magnitude of the velocity vector [3]. To estimate the uncertainties in the various statistical moments, a statistical analysis of residuals method, as described by Aeschliman and Oberkampf [26], was employed. That involved comparisons of replicate measurements made over the course of the LDV data collection, which transpired over a period of days to several weeks. Replicate measure-
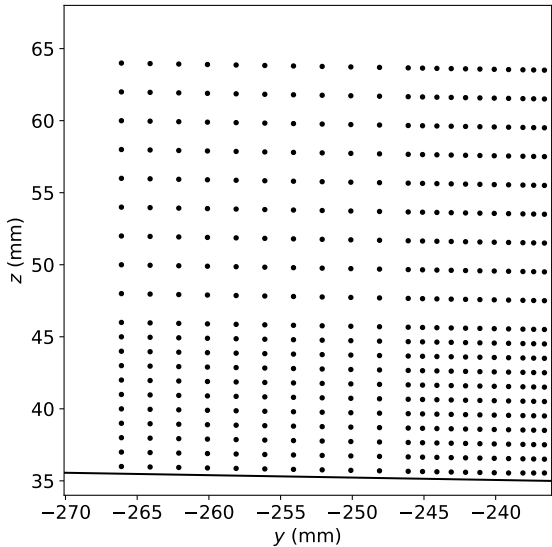
Figure 6: Example (y, z)-plane survey grid in the wing-fuselage junction region.

ments made at the same nominal Reynolds number, model angle of incidence, test-section location, and flowfield location yielded information about the random component of uncertainty. Replicate measurements made before and after a physical repositioning of the LDV hardware, which required a remeasurement of the probe beam unit vectors, yielded information about that effect on the measurement uncertainty. Combining both factors, the statistical analysis of residuals yielded a three-standard-deviation (99.7% confidence interval) uncertainty estimate for each point in a flowfield survey.

3   Numerical methods

The NASA FUN3D code [27, 28] was used for all computations in this paper. FUN3D is an unstructured three-dimensional, implicit, Navier-Stokes code that is nominally second-order spatially accurate. Roe's flux difference splitting [29] was employed. Other details regarding the code can be found in the extensive bibliography that is accessible at the FUN3D website [30].

The RANS computations here were all performed in "free air" (tunnel walls were not accounted for). Previous JF studies have looked at the influence of tunnel walls on CFD results [31, 32]. Although quantifiable, the wall effects on most of the JF flowfield quantities of interest were relatively small. In the current free-air studies, a farfield Riemann invariant boundary condition was imposed on the outer boundary, no-slip solid wall boundary conditions were applied on the test article, and symmetry conditions were used on the x-z symmetry plane. The default turbulence model employed was Spalart-Allmaras [33] with Rotation-Curvature correction [34] and QCR2020 [12] (SA-RC-QCR2020). The computations used a series of meshes ranging from 13 million nodes to 87 million nodes. The predicted separation sizes, surface pressures, velocity profiles, and Reynolds stresses did not vary significantly with this mesh variation, indicating reasonable mesh convergence properties for these quantities of interest on this test case. Only CFD results on the finest mesh are reported herein.

19

4 Results

In this section, a sampling of the experimental data will be presented and the key flow physics associated with that data will be highlighted and discussed. The RANS CFD results will also be used to support the discussions of the experimental results where appropriate. The full set of data for the test can be found on the NASA TMR website [10].

4.1 Surface visualizations in the wing-fuselage junction region

Oil-flow visualizations were first used to characterize the corner flow surface topology near the wing trailing edge for a range of model angles of incidence. Here, we focus the discussion on the three angles of incidence at which detailed flowfield measurements were performed with the LDV systems. At $\alpha = 0°$ (figure 7a), the oil flow suggests that the corner flow is fully attached and no back flow of the oil-flow material was observed. At $\alpha = 1°$ (figure 7c), the oil-flow again suggests fully attached corner flow, but it is on the verge of separating (which here, we define as incipient separation). With a slight increase in α to $1.25°$ (not shown), oil-flow material began to accumulate in the corner, signaling the formation of a separated-flow region with back flow. With further increases in α, a nodal point of separation in the wing-fuselage corner was observed to move upstream and a line of separation emanating from the nodal point was observed on the wing surface. Figure 7e shows the small corner-flow separation that forms at $\alpha = 5°$. For this case, the separation length (defined as the straight line distance from the nodal point to the trailing edge) and width (defined as the distance along the trailing edge from the fuselage to the point where the separation line intersects the trailing edge) were 23.5 ± 3.7 mm and 3.5 ± 0.8 mm, respectively.

For comparison to the oil-flow visualizations, the computed skin-friction coefficient contours and limiting streamlines in the vicinity of the trailing edge corner region for $\alpha = 0°$, $1°$, and $5°$ are shown in figures 7b, d, and f, respectively. In contrast to the experiment, the CFD predicts a corner-flow separation for all three angles of incidence. Here, the nodal point of separation moves upstream and the line of separation emanating from it moves outboard along the wing span as the model angle of incidence is increased. For $\alpha = 5°$ in particular, the CFD predicts a separation length and width of 45.9 mm and 7.3 mm, respectively, which is roughly twice that observed in the oil flow. Later, when we discuss the flowfield measurements, we will highlight some key differences between the experimental measurements and the CFD simulations that may result in this predicted early onset of corner-flow separation.

Since the oil-flow visualizations provide only a qualitative and time-averaged picture of the surface-flow topology, it is of interest to examine how the velocity samples from LDV measurements very close to the junction corner correlate with the oil flow. To that end, figure 8 shows the joint probability distributions for the instantaneous velocity components tangential, U_s/U_{ref}, and normal, W_s/U_{ref}, to the wing surface at x locations of 2926.6 mm, 2944.6 mm, and 2961.6 mm ($\hat{x} = 0.966$, 0.983, and 0.999) and $(\delta y, \delta z) = (500 \ \mu m, 500 \ \mu m)$ from the corner. The probability density functions (PDFs) for each component are included on the top and right side of each plot in the figure, and the plus symbol in the plots denotes the mean velocity ($\langle U_s \rangle, \langle W_s \rangle$). The three x locations were selected on the basis of the oil-flow visualization at $\alpha = 5°$, where $x = 2926.6$ mm is located approximately one separation length upstream from the nodal point of separation, $x = 2944.6$ mm is near the nodal point of separation, and $x = 2961.6$ mm is approximately 1 mm upstream from the wing trailing edge.

For $\alpha = 0°$ (figures 8a–c), the mean velocity vector points downstream for each x location, supporting the conclusion from the oil-flow visualization that the corner flow is fully attached in a time-averaged sense. At the most downstream location (figure 8c), however, the joint distribution indicates that the instantaneous flow experiences intermittent reversed flow approximately 3% of the time. Here, presumably, the mean velocity magnitude is low enough such that large-scale structures in the corner flow boundary layers can induce an intermittent reversed flow near the corner. For $\alpha = 1°$ (figures 8d–f), the mean velocity vector for each x location again points downstream,
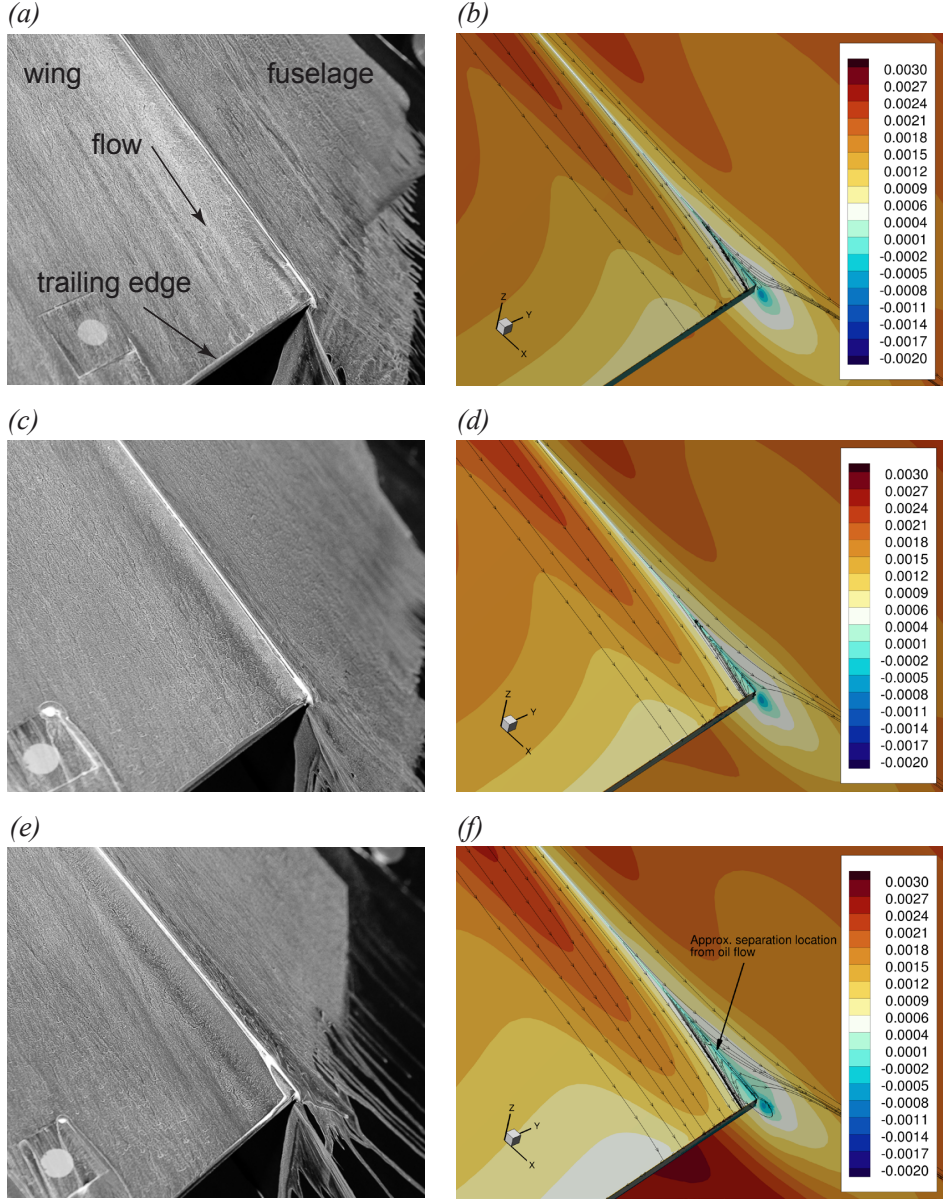
Figure 7: (*a*), (*c*), and (*e*) Oil-flow visualizations near the trailing edge of the wing-fuselage junction at $\alpha = 0°$, $1.0°$, and $5.0°$. (*b*), (*d*), (*f*) Computed skin friction coefficient contours and limiting streamlines near the trailing edge of the wing-fuselage junction at $\alpha = 0°$, $1.0°$, and $5.0°$.

supporting the observation from the oil-flow that the corner flow is still fully attached. However, the magnitudes of the mean velocity vectors at each location are reduced relative to the $\alpha = 0°$ case, and the joint distribution at the most downstream location (figure 8f) shows that the instantaneous flow experiences an increase in intermittent reversed flow to approximately 9% of the time. For $\alpha = 5°$ (figures 8g–i), the mean velocity vectors at $x = 2926.6$ mm and 2944.6 mm are further reduced in magnitude, but still point downstream, supporting the observation from the oil flow that the corner flow is attached up to the nodal point of separation. The joint distribution for $x = 2944.6$ mm (figure 8h) also shows that the instantaneous flow is beginning to experience intermittent reversed flow as
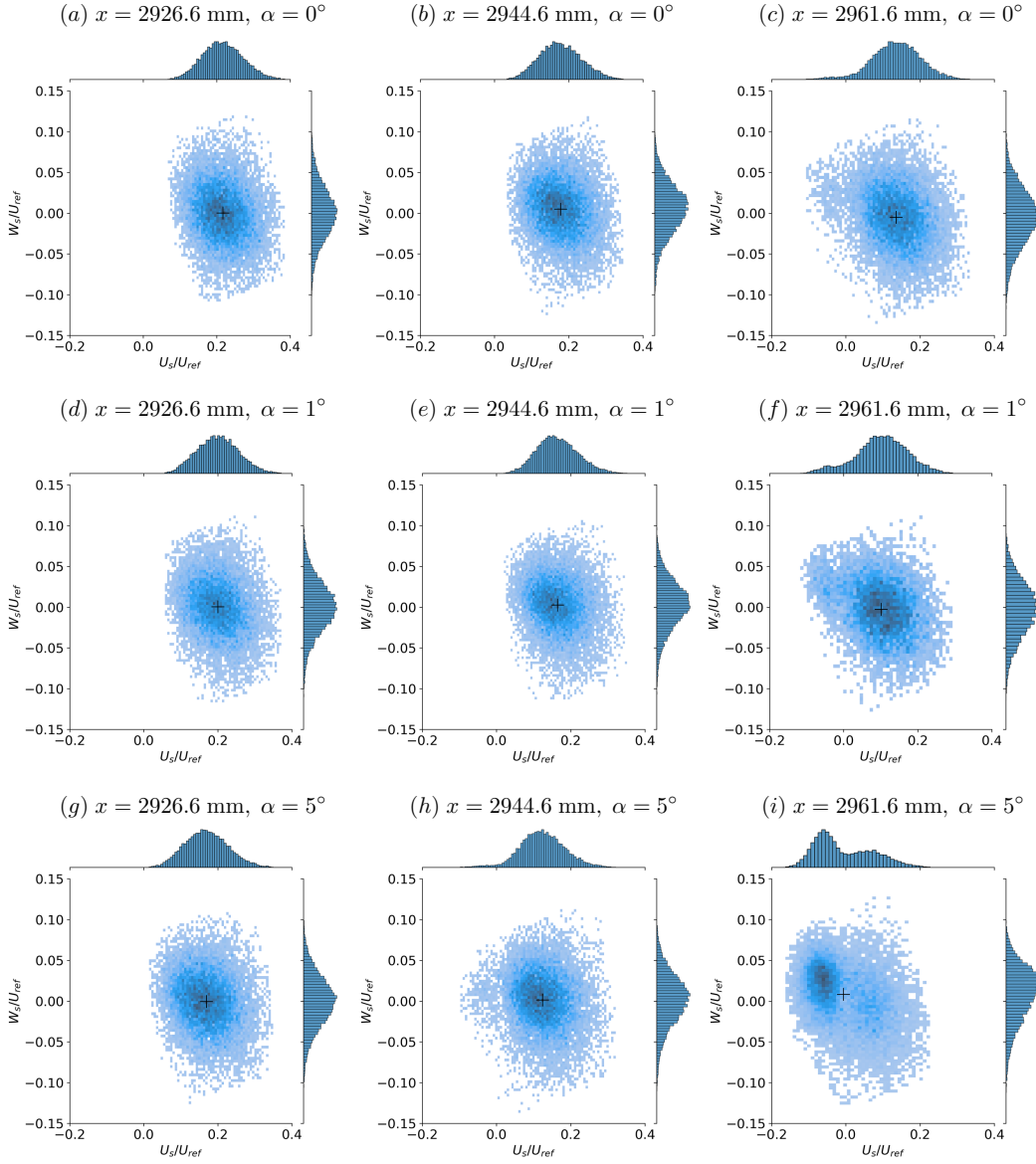
Figure 8: Joint probability distributions for velocity components tangential (U_s/U_{ref}) and normal (W_s/U_{ref}) to the wing surface at (δy, δz) = (500 μm, 500 μm) from the junction corner. (*a*), (*b*), and (*c*) x = 2926.6 mm, 2944.6 mm, and 2961.6 mm at $\alpha = 0°$. (*d*), (*e*), and (*f*) x = 2926.6 mm, 2944.6 mm, and 2961.6 mm at $\alpha = 1.0°$. (*g*), (*h*), and (*i*) x = 2926.6 mm, 2944.6 mm, and 2961.6 mm at $\alpha = 5.0°$. The + symbol in the plots denotes the mean value ($\langle U_s \rangle$, $\langle W_s \rangle$).

the nodal point of separation is approached. In contrast, the mean velocity vector at x = 2961.6 mm points upstream, which indicates reversed flow and confirms that the corner flow is separated at this location. Here, the joint distribution (figure 8i) shows that the instantaneous flow experiences reversed flow 59% of the time. The bi-modal nature of the joint distribution for this case—indicating intermittent forward and reversed flow—is likely caused by the unsteady growth and shrinkage of the corner-flow separation over time. That view is supported by PIV measurements of the corner-flow separation on the juncture-flow model configured with the F6 wing geometry [8]. There, the

corner-flow separation was also found to be highly unsteady, and the region of reversed flow was observed to grow and shrink in both the vertical and longitudinal directions.

4.2 Model surface static pressures

In this section, we examine the static pressure measurements on the model surface, and again focus the discussion on the three angles of incidence at which LDV measurements were performed. Figures 9a, c, and e show the computed surface pressure coefficient (C_p) distributions on the model surface for $\alpha = 0°$, $1°$, and $5°$, respectively. The spanwise locations of the static pressure ports on the wing are also annotated in the figures. Figures 9b, d, and f show the measured and computed C_p distributions at a spanwise location of $y = -254$ mm ($y/b = -0.153$) for the three model angles of incidence. This spanwise location is close to the junction corner (which is located at $y = -236.1$ mm) and provides an indication of the pressure gradient imposed on the corner flow boundary layer. For $\alpha = 0°$ (figure 9b), the C_p distribution indicates that the corner flow is exposed to a favorable pressure gradient over the first 36% of the root chord length, followed by an adverse pressure gradient to the wing trailing edge. As the model angle of incidence is increased, the favorable pressure gradient increases in magnitude, but the chordwise extent decreases (to 29% for $\alpha = 5°$). This is accompanied by an increasingly stronger adverse pressure gradient in the corner flow region after the suction peak. The consequences of this pressure-gradient history on the corner flow boundary layer development will be evident later, when we discuss the the flowfield measurements.

Figure 10 shows the measured and computed C_p distributions on the wing for spanwise locations at the wing planform break ($y = -869.7$ mm or $y/b = -0.523$) and near the wing tip ($y = -1635.76$ mm or $y/b = -0.983$) for all three angles of incidence. The most notable feature of these C_p distributions is the development of a strong suction peak near the wing leading edge of these thinner airfoil sections as α is increased. That, coupled with the strong adverse pressure gradient following the suction peak, resulted in the formation of a laminar separation bubble near the leading edge when only a single row of trip dots were positioned at 6.4% of the local chord length. As mentioned earlier in section 2.2, a second set of trip dots were added to the wing ahead of the leading-edge separation bubble (at 1.6% of the local chord length) to eliminate it, and for the data shown here, both sets of trip dots were in place.

Figures 11a, c, and e show a wider view of the computed C_p distribution on the model surface for $\alpha = 0°$, $1°$, and $5°$, respectively, with annotated x locations for the static pressure ports on the fuselage. In figures 11b, d, and f, the measured and computed C_p distributions along the fuselage at a spanwise location of $y = -76.2$ mm ($y/b = -0.046$) are plotted for all three angles of incidence. Figure 12 shows the measured and computed circumferential C_p distributions in terms of the angular coordinate θ at selected x locations for each angle of incidence. In view of the pressure distributions shown in figures 9–12, the computed C_p values are generally within the experimental uncertainty bars which represent a 95% confidence interval. This good quantitative agreement between the experimental data and the CFD allows us to use the CFD for context when later interpreting and discussing the flowfield measurements on the model.

4.3 Flowfield measurements on the fuselage

In this section, we present boundary-layer profile measurements on the port side of the fuselage at a couple of (x, z) locations. To provide context for the profile measurements, the computed surface pressure coefficient and skin-friction coefficient magnitude on the fuselage nose section are shown in figure 13 for the three model angles of incidence at which LDV measurements are available. Included in the plots are the (x, z) locations of the profile measurements and the limiting streamlines that pass through those locations. The first measurement location of interest is at $x = 1168.4$ mm and $z = 0$ mm, which is far upstream of the wing-fuselage junction and on the symmetry plane of the flat fuselage side wall. For $\alpha = 0°$ (figure 13a), the C_p distribution indicates that the boundary layer at this location is developing under a mild adverse pressure gradient along the length of the
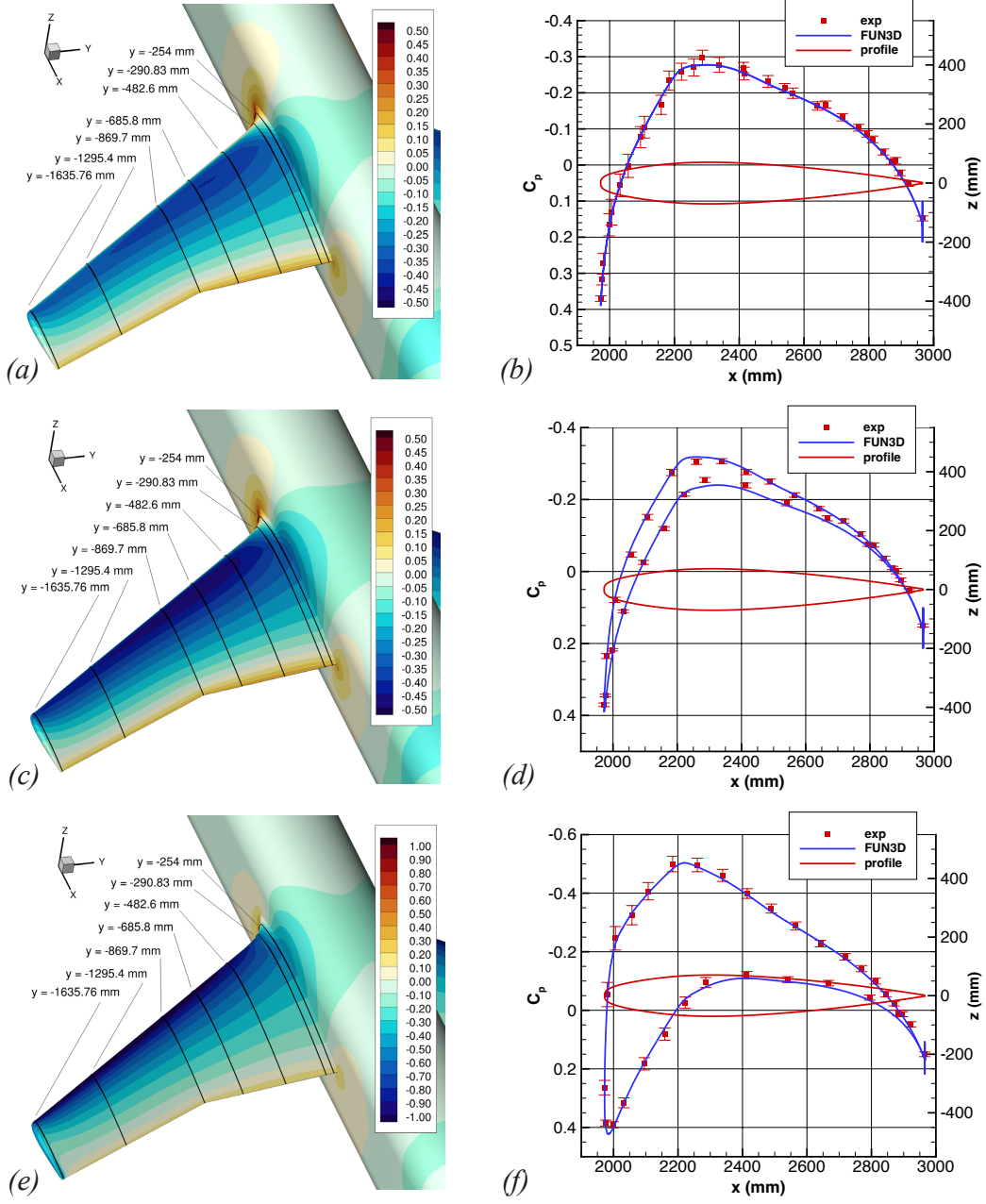
Figure 9: (*a*), (*c*), and (*e*) Computed surface pressure coefficients and spanwise locations of static pressure ports for $\alpha = 0°$, $1.0°$, and $5.0°$. (*b*), (*d*), and (*f*) Experimental and computed surface pressure coefficients at a spanwise location of $y = -254$ mm for $\alpha = 0°$, $1.0°$, and $5.0°$.

fuselage. This is similarly true for $\alpha = 1°$ (figure 13c) and $\alpha = 5°$ (figure 13e), but there is also now a weak favorable pressure gradient in the positive z direction that turns the flow toward the leeward side of the fuselage. The second measurement location of interest is at $x = 1861.5$ mm and $z = 0$ mm, which is just upstream of the wing-fuselage junction (≈ 48 mm). Here, the boundary layer is developing under a stronger pressure gradient as the junction leading edge is approached,
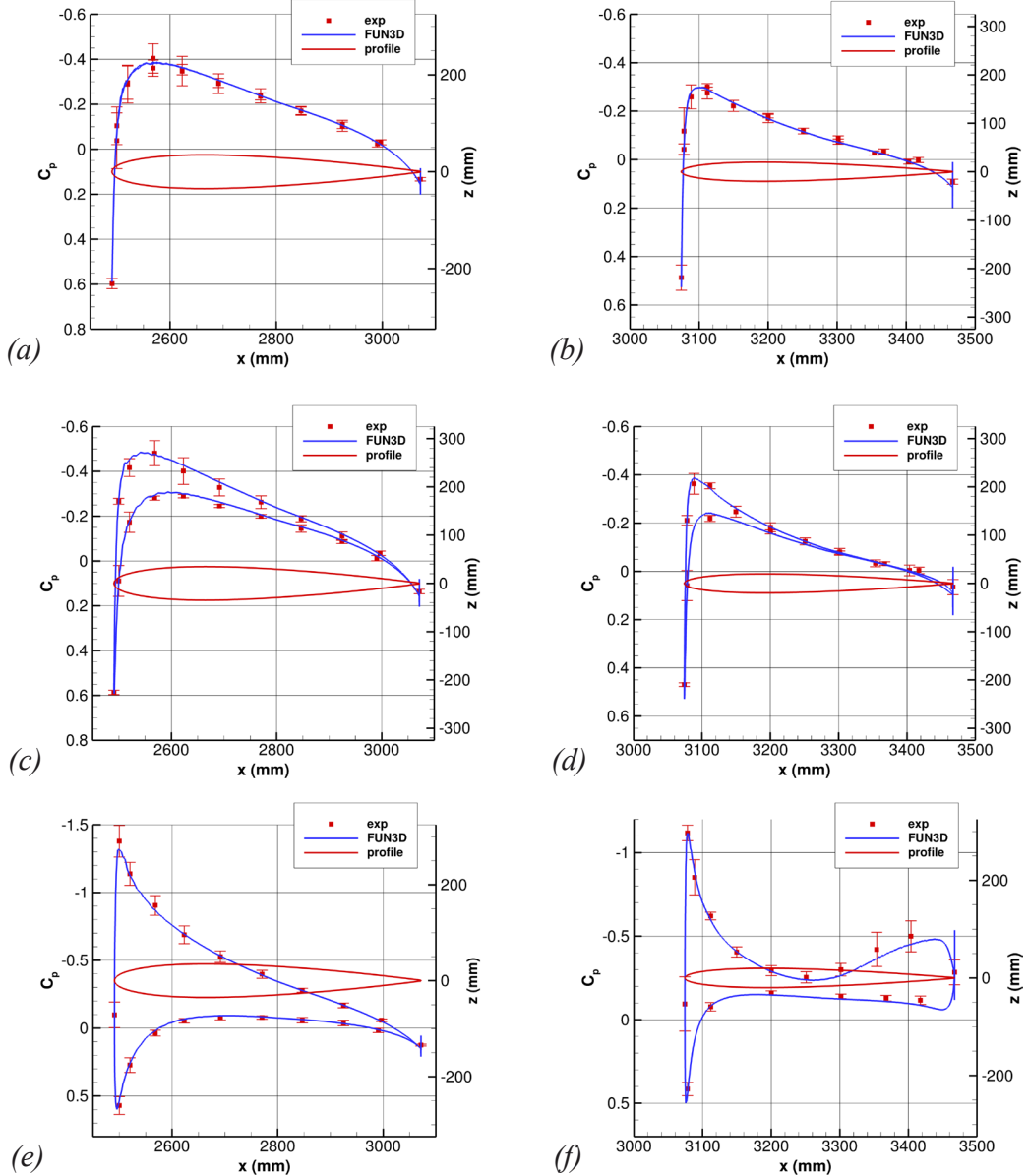
Figure 10: (*a*), (*c*), and (*e*) Experimental and computed surface pressure coefficients at a spanwise location of $y = -869.7$ mm for $\alpha = 0°$, $1.0°$, and $5.0°$. (*b*), (*d*), and (*f*) Experimental and computed surface pressure coefficients at a spanwise location of $y = -1635.76$ mm for $\alpha = 0°$, $1.0°$, and $5.0°$.

but the flow is still attached at this location for all three angles of incidence. The favorable pressure gradient in the positive z direction is also larger at this location and that leads to more significant flow turning for the positive angles of incidence.

One notable feature of the computed skin friction coefficient contours in figure 13 is the sudden jump in skin friction near the nose of the fuselage. As discussed earlier, boundary-layer transition on the fuselage was fixed in the experiment by a row of trip dots placed around the circumference of
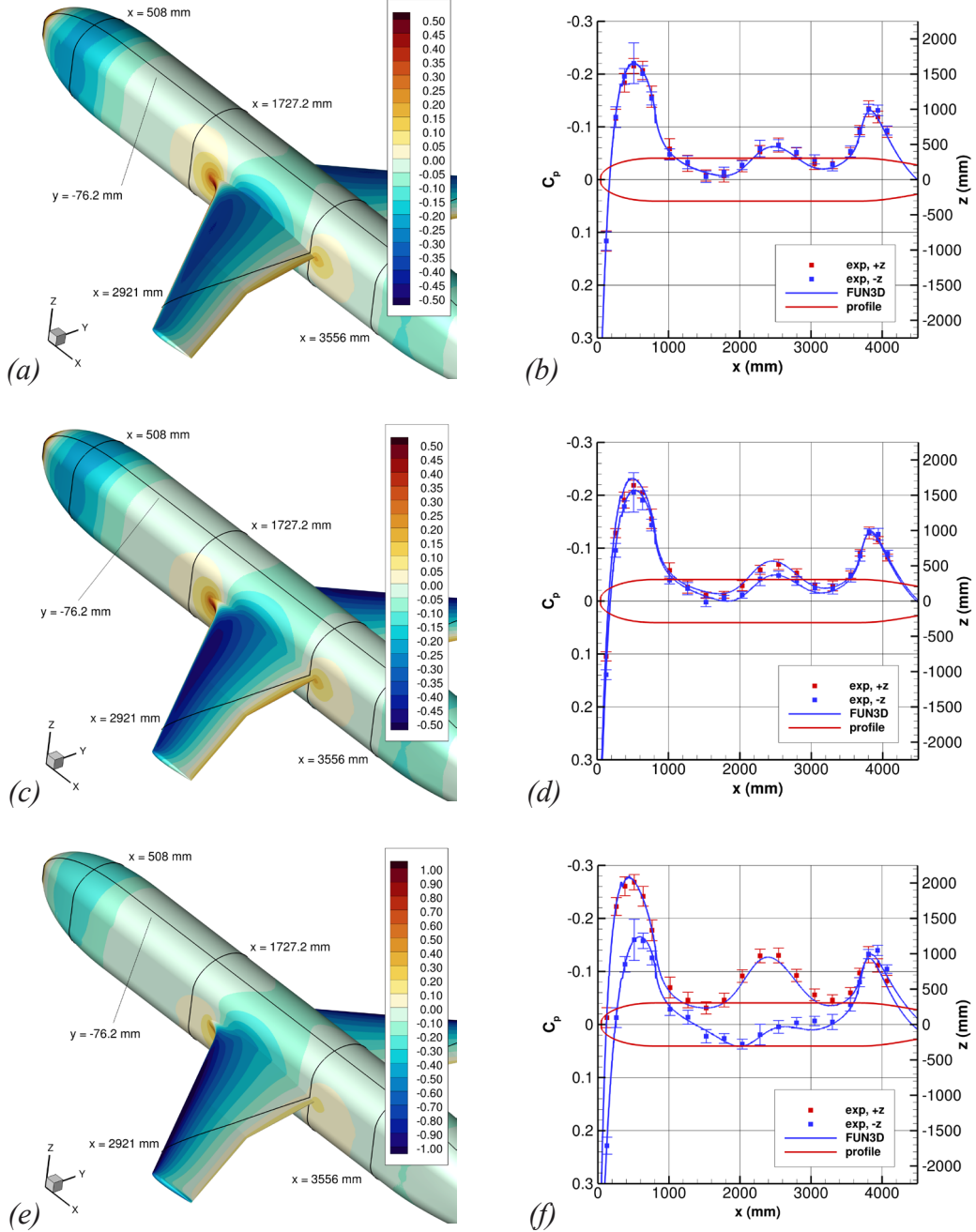
Figure 11: (*a*), (*c*), and (*e*) Computed surface pressure coefficients and locations of static pressure ports for $\alpha = 0°$, $1.0°$, and $5.0°$. (*b*), (*d*), and (*f*) Experimental and computed surface pressure coefficients at a spanwise location of $y = -76.2$ mm for $\alpha = 0°$, $1.0°$, and $5.0°$.

the fuselage at $x \approx 336$ mm. In the computations, however, the trip dots were not directly modeled. Instead, the transition location was imposed by zeroing out the production terms in the turbulence model ahead of the $x = 336$ mm location. Shortly downstream of that location, the computed boundary layer becomes fully turbulent and that is reflected by the sharp rise in the skin-friction
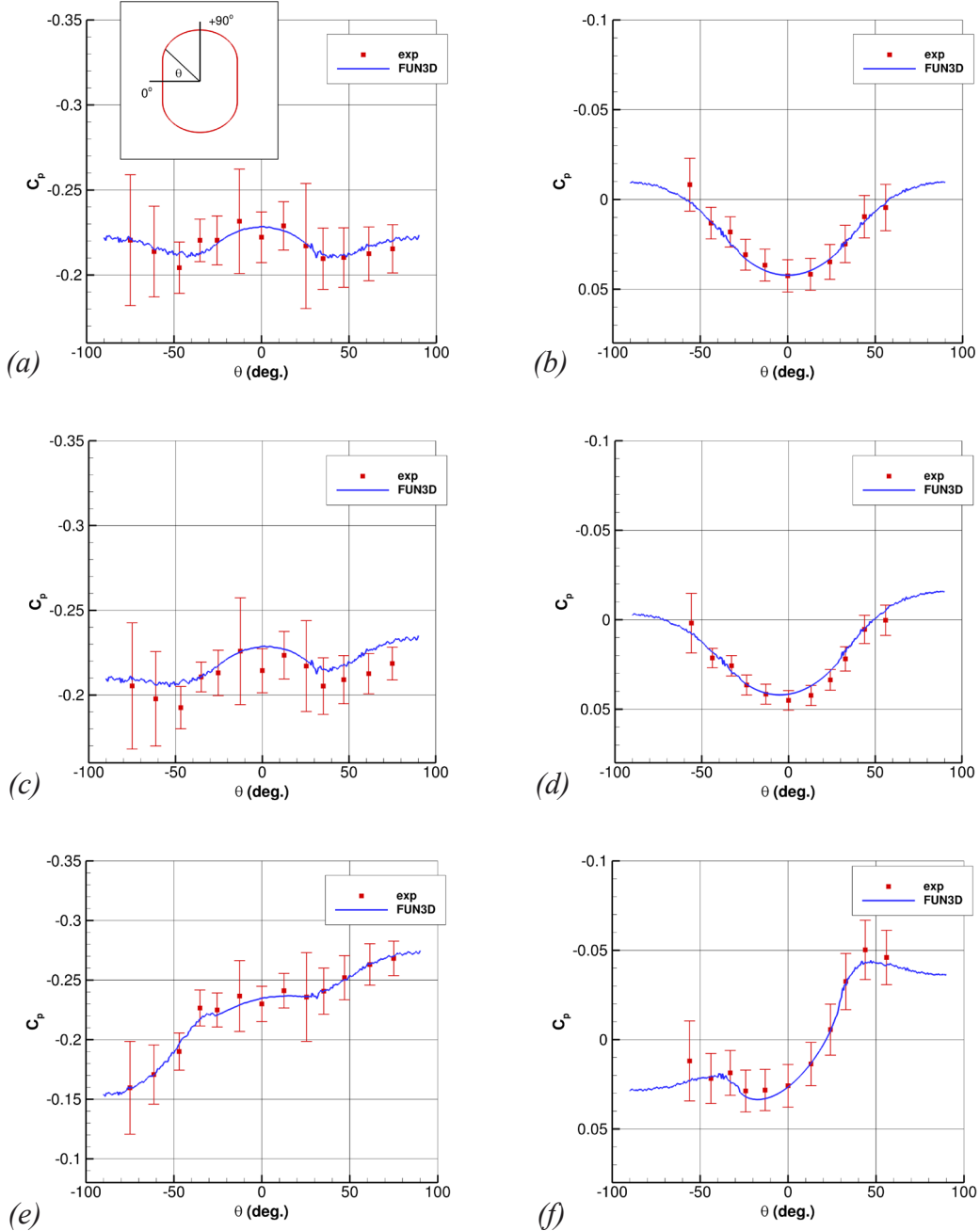
Figure 12: (*a*), (*c*), and (*e*) Experimental and computed surface pressure coefficients at an x location of $x = 508$ mm for $\alpha = 0°$, $1.0°$, and $5.0°$. (*b*), (*d*), and (*f*) Experimental and computed surface pressure coefficients at an x location of $x = 1727.2$ mm for $\alpha = 0°$, $1.0°$, and $5.0°$.

coefficient observed in figures 13b, d, and f.

The mean-velocity and Reynolds-stress profiles at $x = 1168.4$ mm and $z = 0$ mm for $\alpha = 0°$, $1°$, and $5°$ are shown in figure 14. Here, the experimental data are represented by symbols with shaded bands for the measurement uncertainty and the computed boundary layer profile quantities

27
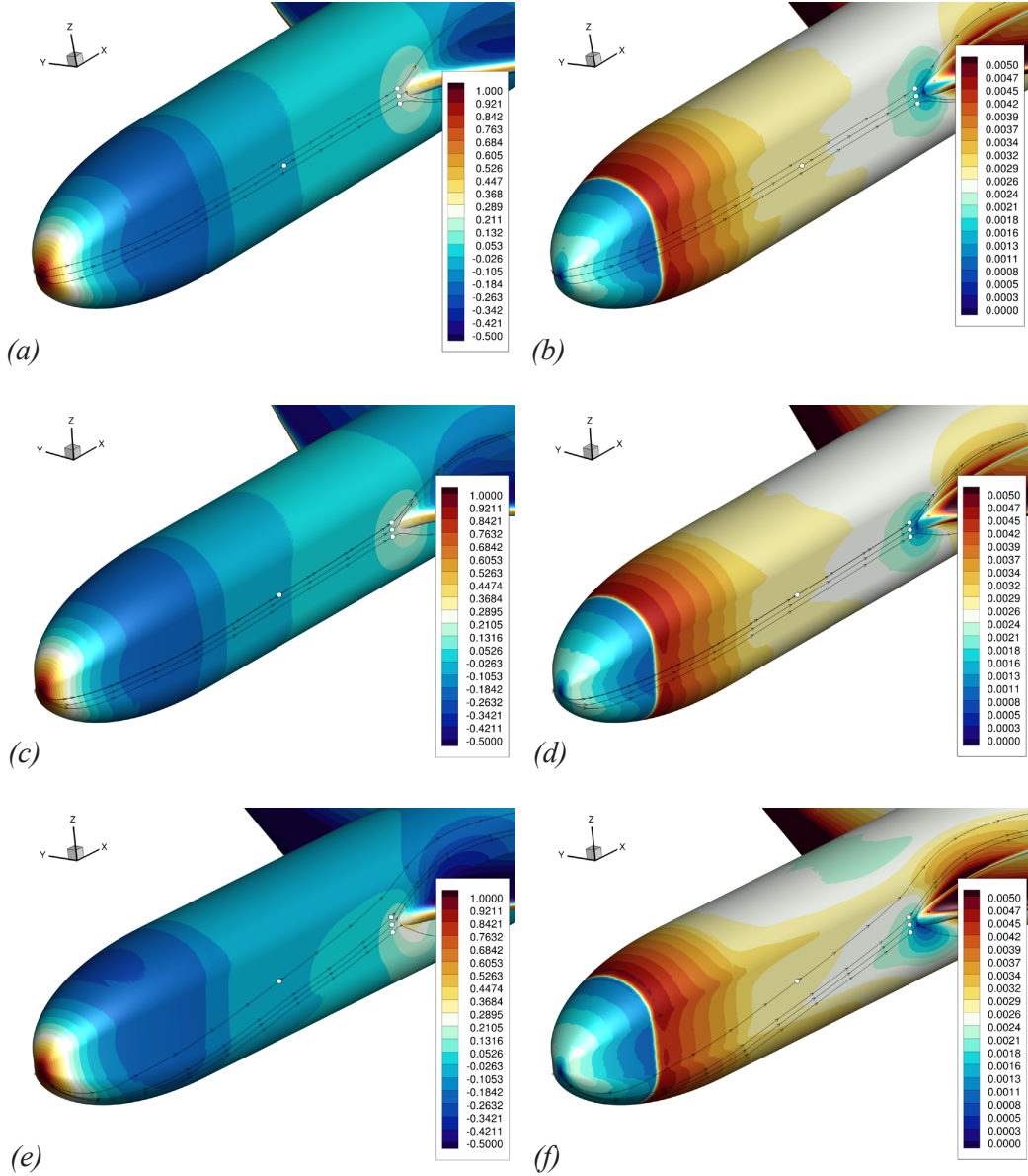
Figure 13: (*a*), (*c*), and (*e*) Computed surface pressure coefficient on the fuselage nose for $\alpha = 0°$, $1.0°$, and $5.0°$. (*b*), (*d*), and (*f*) Computed skin friction coefficient magnitude on the fuselage nose for $\alpha = 0°$, $1.0°$, and $5.0°$. Limiting streamlines passing through the (x, z)-locations of the boundary layer profile measurements on the fuselage (filled circles) are also shown.

are represented by solid lines. For the abscissa label in the plots, y_o denotes the fuselage surface location and is equal to -236.1 mm ($y/b = -0.142$). The x-component of mean velocity, $\langle U \rangle$, is characteristic of an incompressible turbulent boundary layer, with a distinct log region followed by a wake region in the outer portion of the boundary layer. At $\alpha = 0°$ (figure 14a), the z-component of mean velocity, $\langle W \rangle$, is nearly zero since the measurement location is on the symmetry plane of the fuselage. As α is increased (figures 14c and e), the weak favorable pressure gradient in the positive z direction begins to turn the flow toward the leeward side of the fuselage and $\langle W \rangle$
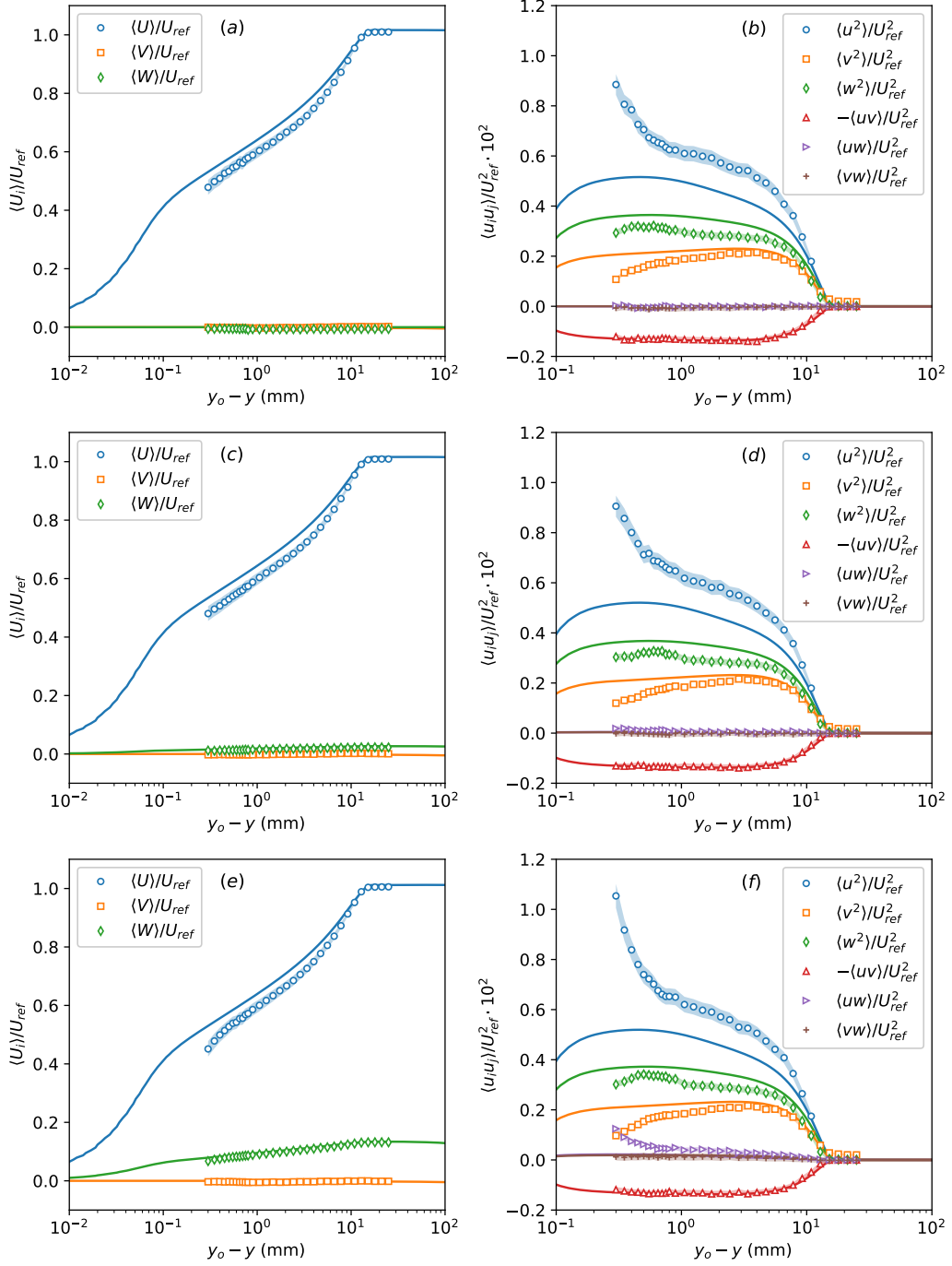
Figure 14: (*a*), (*c*), and (*e*) Measured (symbols) and computed (lines) mean-velocity profiles on the fuselage at $x = 1168.4$ mm, $z = 0$ mm for $\alpha = 0°$, $1.0°$, and $5.0°$. (*b*), (*d*), and (*f*) Measured (symbols) and computed (lines) Reynolds-stress profiles on the fuselage at $x = 1168.4$ mm, $z = 0$ mm for $\alpha = 0°$, $1.0°$, and $5.0°$.

29
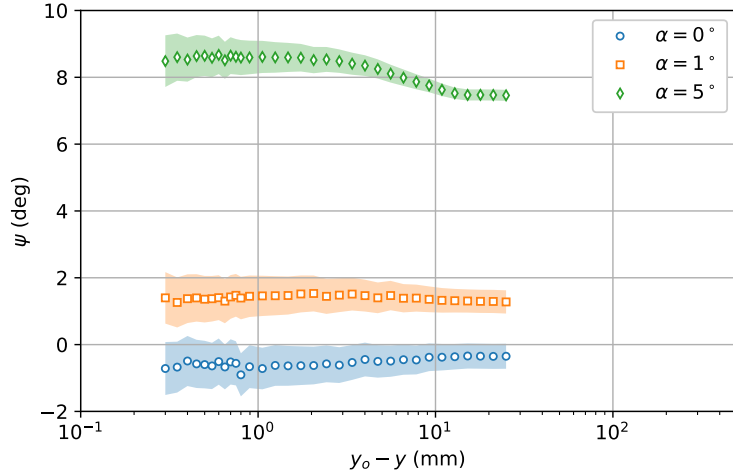
Figure 15: Mean-flow angles, $\psi = \arctan\left(\langle W \rangle / \langle U \rangle\right)$, for the measured boundary layer profiles on the fuselage at $x = 1168.4$ mm, $z = 0$ mm.

becomes increasingly positive. The corresponding mean-flow angle, $\arctan\left(\langle W \rangle / \langle U \rangle\right)$, for each α is shown in figure 15. At $\alpha = 0°$, the measured mean-flow angle is slightly negative. In theory, this should be zero, but a small mismatch between the geometric angle of incidence, α, and the freestream flow angle may be responsible for the negative mean-flow angle. On the other hand, the uncertainty interval for many of the points in the profile includes the zero mean-flow angle and so this difference from zero is not statistically significant. For $\alpha = 1°$, where the flow begins to turn toward the leeward side of the fuselage, the mean-flow angle is now positive. For $\alpha = 5°$, the mean-flow angle is even larger and it now varies across the boundary layer. This indicates mean-flow skewing of the boundary-layer profile, where the near-wall low-momentum fluid exhibits more flow turning than the outer freestream flow.

The Reynolds-stress profiles shown in figure 14 have distributions similar to those for a moderate Reynolds number, incompressible zero-pressure-gradient boundary layer [35]. One notable difference from that canonical flow is related to the Reynolds shear-stress components $\langle uw \rangle$ and $\langle vw \rangle$. For $\alpha = 0°$ (figure 14b), both of these shear-stress components are zero due to the geometric symmetry at this measurement location and that is similar to the canonical boundary layer. As α increases, however, both of these shear-stress components begin to deviate from zero, particularly near the wall. As shown in Rumsey et al. [5], both shear-stress components are nearly zero when viewed in a streamline oriented coordinate system, indicating that part of that deviation is due to the coordinate system in which the Reynolds stresses are calculated. Even then, small deviations from zero still exist for these shear-stress components due to the weak three-dimensionality of the boundary layer and the associated mean-flow skewing at this location on the fuselage.

To this point, we have focused the discussion only on the experimental data shown in figure 14, so it is now worthwhile to compare that data to the computed boundary layer profile quantities. For the mean-velocity profiles, the most notable difference is in the x-component of mean velocity, particularly in the log region of the boundary-layer profile. Here, the predicted CFD is shifted up relative to the measured $\langle U \rangle$ velocity. This implies that the predicted skin-friction coefficient at this location is higher than the experiment. Although the exact reason for this difference is not clear, it may stem from the trip dots used to fix transition in the experiment, which introduce a momentum loss in the boundary layer that persists far downstream and that effect is not captured in the CFD due to the way in which transition is imposed. When comparing the Reynolds normal-stress components from the experiment to the CFD, we see that the CFD generally overpredicts the $\langle v^2 \rangle$

Table 2: Boundary-layer parameters at $x = 1168.4$ mm, $z = 0$ mm for $\alpha = 0°$

Parameter	Experiment	CFD	ZPG TBL [37]
δ	15.2	16.6	–
δ^*	2.6	2.3	–
θ	1.8	1.7	–
H	1.42	1.36	1.33
c_f	0.0024	0.0027	$0.0028 - 0.0027$
Re_θ	7559	7093	$7451 - 7599$
Π	1.08	0.63	0.55
ℓ_v, μm	6.96	6.46	–

and $\langle w^2 \rangle$ components and underpredicts the $\langle u^2 \rangle$ component, with the largest deviation occurring near the wall. Those trends are typical of many RANS turbulence models, but the QCR2020 modification used in the present study was previously shown to offer significant improvements in the normal-stress predictions over earlier versions of QCR [12]. In contrast, the Reynolds shear-stress component $\langle uv \rangle$ is predicted very well by the CFD. For the shear-stress components $\langle uw \rangle$ and $\langle vw \rangle$, both are zero for the experiment and CFD at $\alpha = 0°$ due to symmetry at the measurement location. For $\alpha = 1°$ and $5°$, the predicted $\langle vw \rangle$ is in good agreement with the experimental data. In contrast, the predicted $\langle uw \rangle$ does not agree with the experimental data, particularly in the near-wall region. As discussed by Rumsey et al. [5] this disagreement is related to the underprediction of the normal-stress component in a streamline oriented coordinate system and how that factors into the calculation of $\langle uw \rangle$ in the body-fixed coordinate system.

Although the skin friction was not measured during the test entry, an estimate is desired so that several boundary-layer parameters at the $x = 1168.4$ mm location can be calculated. To that end, an explicit closed form expression for the velocity distribution of a smooth wall turbulent boundary layer was fit to the $\langle U \rangle$ profile for $\alpha = 0°$ using the method of least squares. This approach is considered reasonable given that the profile measurement was made on the symmetry plane of the flat fuselage side wall where the local boundary layer is effectively two dimensional at $\alpha = 0°$. The expression for the velocity distribution, originally developed by Musker [36], is parameterized by the friction velocity, u_τ, the boundary-layer thickness, δ, and the wake-strength parameter, Π. Using the friction velocity obtained from the curve fit, the wall shear stress and the skin-friction coefficient, c_f, were calculated. The curve fit was also used to calculate the integral properties of the boundary layer (i.e., the displacement thickness, δ^*, the momentum thickness, θ, and the shape factor, $H = \delta^*/\theta$), along with the momentum thickness Reynolds number, Re_θ, and the viscous length scale, $\ell_v = \nu/u_\tau$. These values are shown in table 2 along with a companion set of parameter values from the CFD calculations. As a point of reference, the values of H, c_f, and Π for a zero-pressure-gradient (ZPG) turbulent boundary layer are included in the table and those parameters were obtained from the tabulated values reported by Coles [37]. Here we see that the experimental H and Π are larger and c_f is smaller that those values for a ZPG turbulent boundary layer at the same Re_θ, which is consistent with a turbulent boundary layer developing under an adverse pressure gradient. Using the friction velocity from the curve fit, the boundary layer profile at $x = 1168.4$ mm and $\alpha = 0°$ is plotted with inner-layer scaling in figure 16. Here, the Musker curve fit is seen to provide a good correlation for the $\langle U \rangle$ velocity profile.

The mean-velocity and Reynolds-stress profiles at $x = 1861.5$ mm and $z = 0$ mm for $\alpha = 0°$, $1°$, and $5°$ are shown in figure 17 and profiles of the corresponding mean-flow angle are shown in figure 18. Recall that this location is near the leading edge of the wing-fuselage junction and here the boundary layer is developing under a stronger adverse pressure gradient. That results in an overall reduction in the $\langle U \rangle$ velocity throughout the boundary-layer profile and a more negative $\langle V \rangle$ velocity toward the boundary-layer edge. The latter is due to the increased boundary-layer growth as the flow
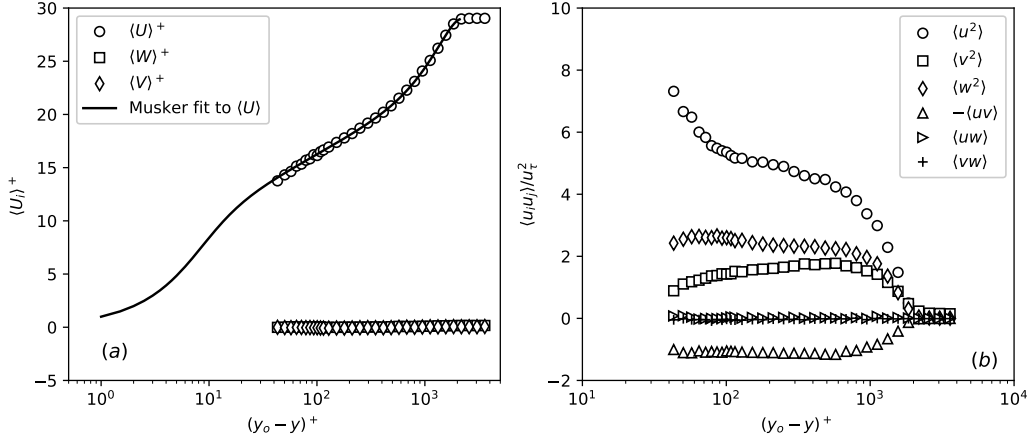
Figure 16: Measured boundary layer profile at $x = 1168.4$ mm, $z = 0$ mm for $\alpha = 0°$. (a) Mean-velocity components and Musker fit in wall units. (b) Reynolds stresses in wall units.

on the fuselage approaches the junction leading edge. The mean-flow angle at $\alpha = 0°$ is zero to within the measurement uncertainty. For $\alpha = 1°$ and $5°$, the mean-flow angle becomes positive as the favorable pressure gradient in the positive z direction turns the flow on the fuselage toward the upper side of the junction leading edge. There is also significant mean-flow skewing for these angles of incidence. In terms of the Reynolds-stress profiles, they are qualitatively similar to those at the upstream location (figure 14). The most notable differences are the development of a plateau in the $\langle u^2 \rangle$ normal-stress component in the log region of the boundary layer, and a stronger variation in the $\langle uw \rangle$ shear-stress component due to the more significant mean-flow skewing. Comparing the experimental data to the CFD calculations in figure 17, the predicted CFD is again shifted up relative to the measured $\langle U \rangle$ velocity profile. The predicted CFD also shows a further deviation from the two $\langle U \rangle$-profile points closest to the wall, and that is attributed to spatial averaging across the LDV measurement volume in the high-gradient region of the near-wall flow. In view of the Reynolds-stresses, the CFD generally overpredicts $\langle v^2 \rangle$ and $\langle w^2 \rangle$, underpredicts $\langle u^2 \rangle$, and provides a good prediction of $\langle uv \rangle$ and $\langle vw \rangle$. The CFD does not properly capture the distribution of $\langle uw \rangle$ for the reasons discussed earlier.

4.4 Flowfield measurements in the wing-fuselage corner region

In this section, we present measurements of the turbulent corner flow that is formed by the confluence of the fuselage and wing boundary layers. These measurements were performed at several x locations along the port-side wing-fuselage junction and here, we will focus the discussion on the $\alpha = 0°$ and $5°$ test cases. The data for $\alpha = 1°$ was found to be qualitatively similar to that for $0°$. The first location of interest is at $x = 2145$ mm ($\hat{x} = 0.22$), which is ahead of the local suction peak and so the corner flow is developing under a favorable pressure gradient. Contours of the measured mean-velocity components at this location are shown in figure 19 for $\alpha = 0°$ and $5°$. In these plots, the right side of the figures corresponds to the fuselage surface ($y = -236.1$ mm) and the black line denotes the wing surface. Note that the survey region at this x location was limited by the optical access provided by the fuselage window insert and that prevented us from positioning the LDV measurement volume along the downward-sloping surface of the wing. Nevertheless, some important features of the corner flow can still be measured, particularly in the immediate vicinity of the corner.

Toward the upper boundary of the measurement region, the $\langle U \rangle$-velocity contours near the fuselage surface display very high levels, indicating that the fuselage boundary layer has thinned considerably due to the favorable pressure gradient in this region of the corner-flow development. Down
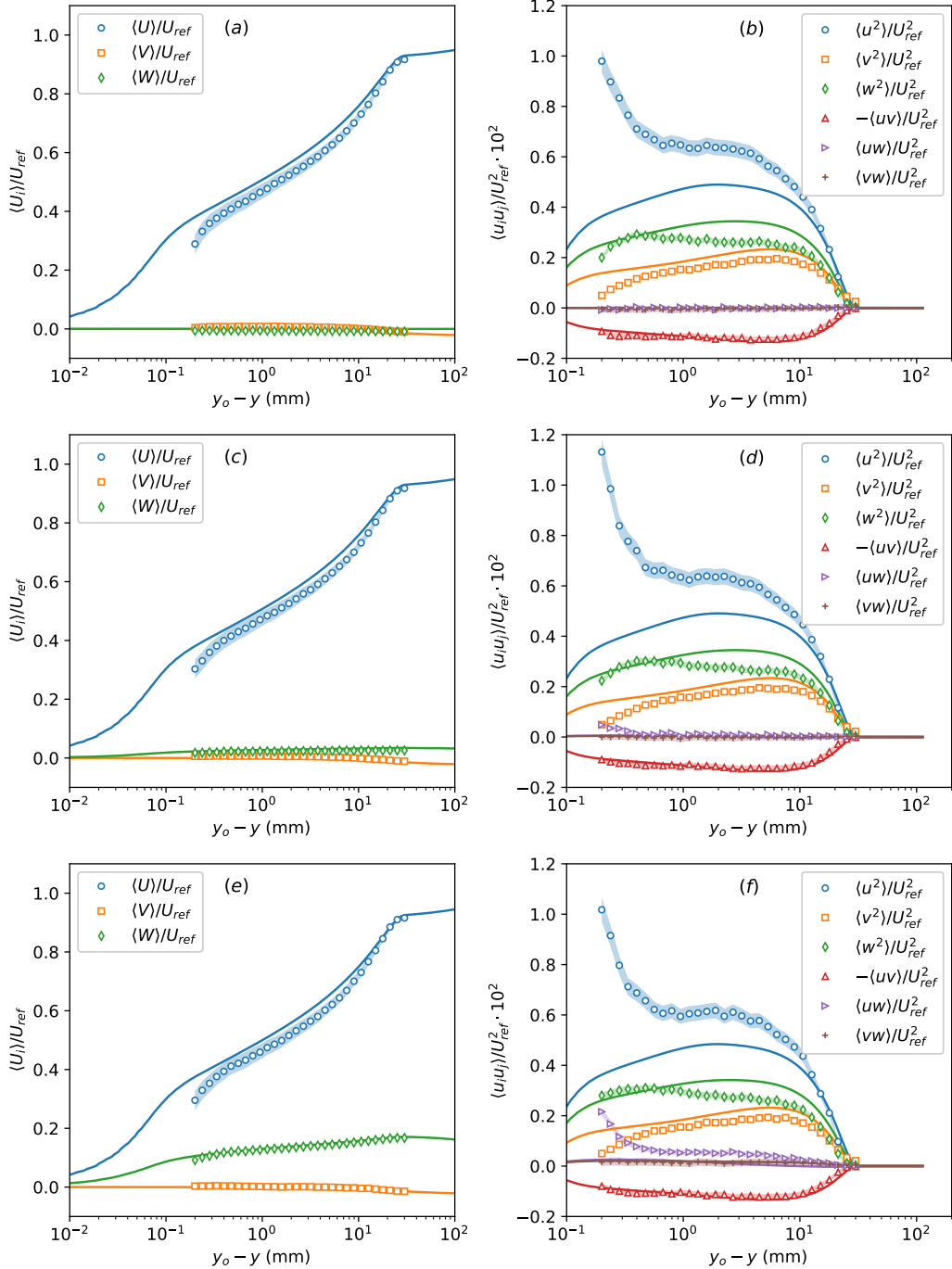
Figure 17: (*a*), (*c*), and (*e*) Measured (symbols) and computed (lines) mean-velocity profiles on the fuselage at $x = 1861.5$ mm, $z = 0$ mm for $\alpha = 0°$, $1.0°$, and $5.0°$. (*b*), (*d*), and (*f*) Measured (symbols) and computed (lines) Reynolds-stress profiles on the fuselage at $x = 1861.5$ mm, $z = 0$ mm for $\alpha = 0°$, $1.0°$, and $5.0°$.

33
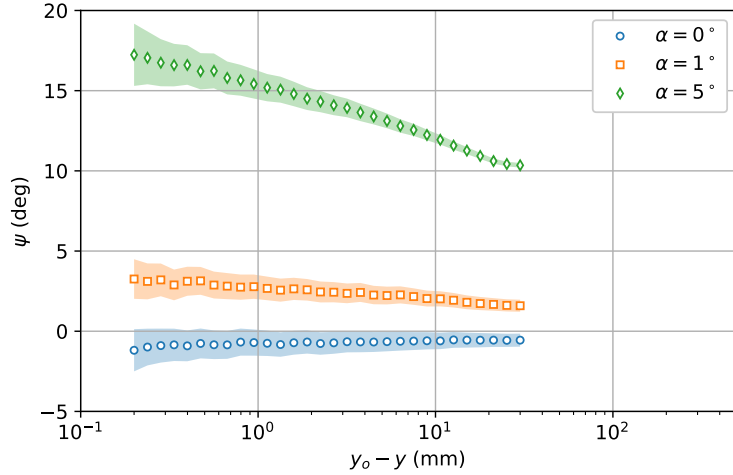
Figure 18: Mean-flow angles, $\psi = \arctan\left(\langle W \rangle / \langle U \rangle\right)$, for the measured boundary layer profiles on the fuselage at $x = 1861.5$ mm, $z = 0$ mm.

near the corner, the $\langle U \rangle$-velocity contours are locally distorted up and away from the wing surface and the distortion becomes more prominent as α increases. This mean-flow distortion is due to the secondary flow in the (y, z) plane, which is characterized by the mean-velocity components $\langle V \rangle$ and $\langle W \rangle$. More specifically, a close examination of the contours for the secondary-flow components suggest that a vortex—with clockwise rotation when looking upstream on the port side of the test article—has formed near the corner and is responsible for the local lift up in the $\langle U \rangle$-velocity contours. Going forward, we will refer to this vortex as a corner vortex. If we were to view a vector plot of the secondary-flow components, however, this corner vortex would not be evident and that is partly due to the coordinate system and the fact that the $\langle W \rangle$-velocity component is positive throughout the measurement region. Instead, consider the mean-velocity components in a coordinate system rotated about the y axis so that the x axis is approximately tangent to the wing surface. In that case we have:

$$\langle U_s \rangle = \langle U \rangle \cos \psi + \langle W \rangle \sin \psi, \tag{8}$$

$$\langle V_s \rangle = \langle V \rangle, \tag{9}$$

and

$$\langle W_s \rangle = -\langle U \rangle \sin \psi + \langle W \rangle \cos \psi \tag{10}$$

for this surface-aligned coordinate system, where $\psi = 6.2°$ is the approximate surface angle at $x = 2145$ mm. Contour plots of the $\langle U_s \rangle$-velocity component with superimposed secondary-flow vectors for this rotated coordinate system are shown in figure 20. Here, the secondary-flow vectors clearly show the corner vortex in the junction corner and indicate that it strengthens with an increase in α. The local lift up in the $\langle U_s \rangle$-velocity contours is also observed to correlate with the upwash side of the corner vortex.

Contours of the measured Reynolds normal-stress and shear-stress components for the $x = 2145$ mm location are shown in figures 21 and 22. Along the fuselage surface, the $\langle u^2 \rangle$ normal stress displays high levels that are confined to a thin region within a few millimeters of the wall. Similarly, the $\langle w^2 \rangle$ normal stress displays higher levels in the same region, but in contrast, the $\langle v^2 \rangle$ normal-stress levels are lower. The latter is due to the confining effect of the wall on the v-velocity fluctuations. In the upwash region of the corner vortex, the $\langle u^2 \rangle$ and $\langle v^2 \rangle$ normal-stress components are strongly enhanced, while the $\langle w^2 \rangle$ normal-stress components is enhanced to a much lesser degree. Generally, the normal-stress components in the upwash region of the corner vortex

34
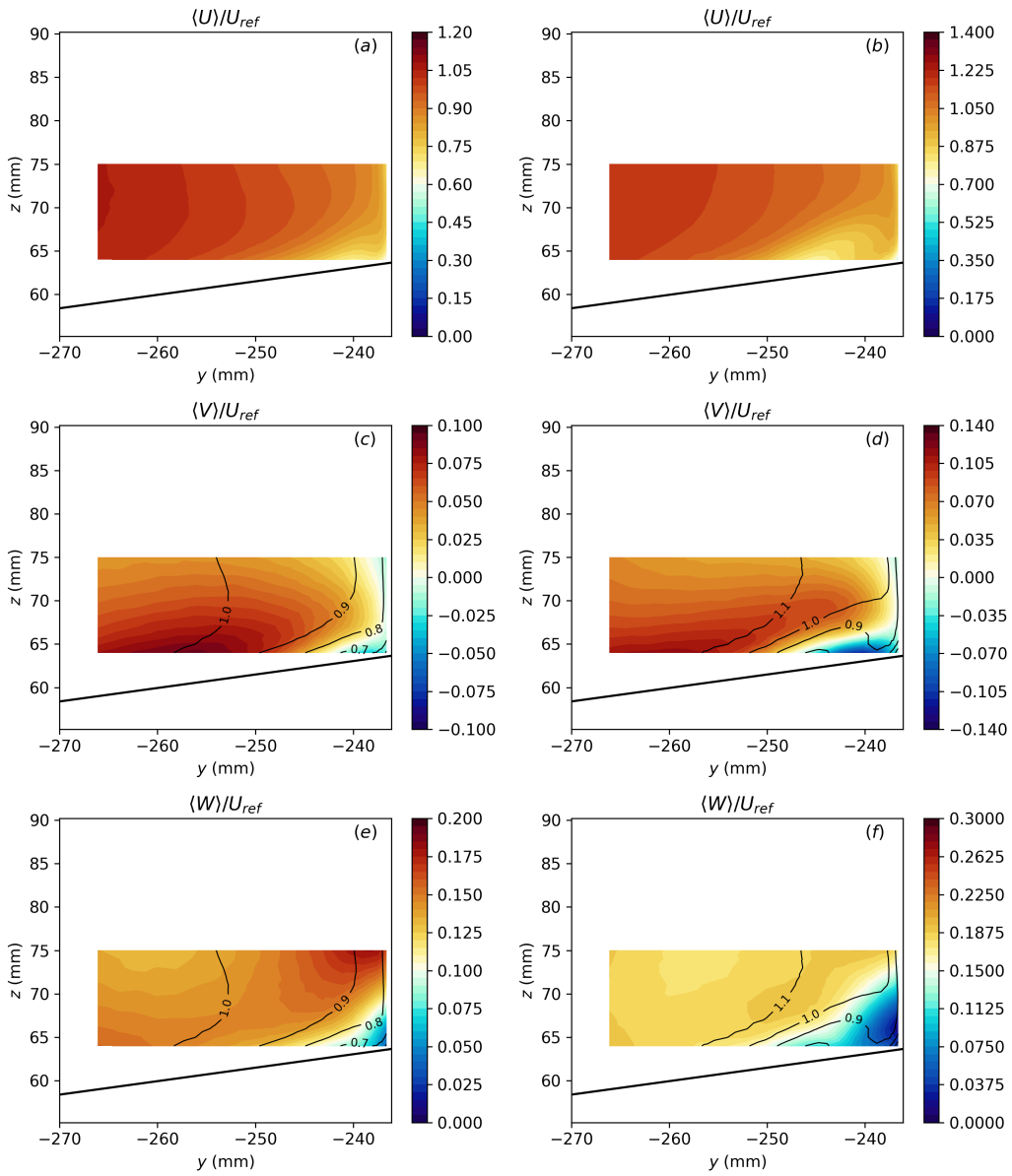
Figure 19: (*a*), (*c*), and (*e*) Contours of the measured mean-velocity components at $x = 2145.0$ mm for $\alpha = 0°$. (*b*), (*d*), and (*f*) Contours of the measured mean-velocity components at $x = 2145.0$ mm for $\alpha = 5°$. The labeled contour lines in the subfigures correspond to the mean velocity, $\langle U \rangle / U_{ref}$, and the solid black line denotes the wing surface.

increase in magnitude as α is increased and the corner vortex intensifies. The Reynolds shear-stress components all display significant modifications associated with the corner vortex. Both the $\langle uv \rangle$ and $\langle uw \rangle$ shear-stress components are enhanced on the upwash side of the corner vortex. In contrast, the $\langle vw \rangle$ shear-stress component displays enhancements in regions of the flow where the corner vortex directs the flow toward or away from the fuselage surface.

Figure 23 presents a comparison between contours of the measured and computed mean-velocity components at the $x = 2145$ mm location for $\alpha = 0°$. Here, the CFD is in good qualitative agree-
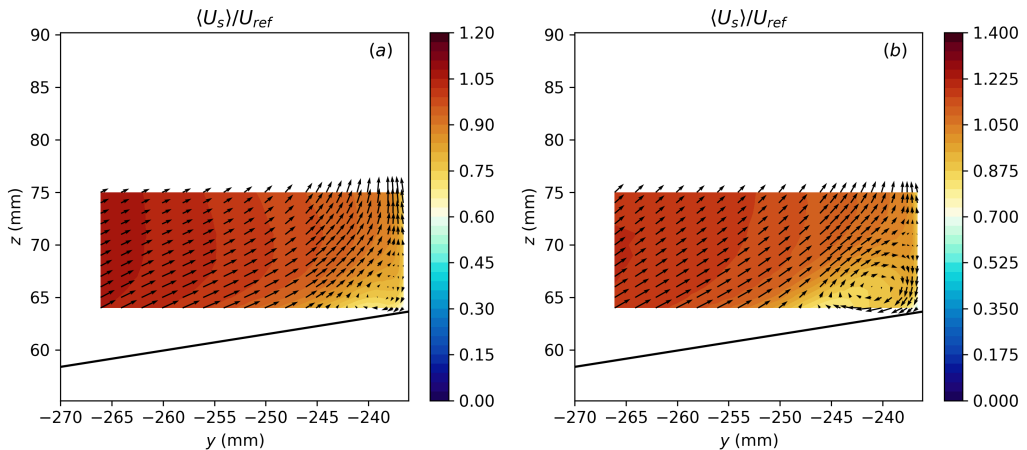
Figure 20: Contours of measured mean velocity, $\langle U_s \rangle / U_{ref}$, and secondary-flow vectors at $x = 2145.0$ mm in a coordinate system rotated about the y axis so that the x axis is approximately aligned to the local slope of the wing surface. (a) $\alpha = 0°$. (b) $\alpha = 5.0°$.

ment with the measurements, showing similar mean-flow distortion in the $\langle U \rangle$-velocity component and similar distributions for the secondary-flow components. As with the measurements, the predicted secondary-flow components also suggest the development of a corner vortex that drives the mean-flow distortion in $\langle U \rangle$. Although not shown here, similar qualitative agreement between the measurements and CFD was observed for the $\alpha = 5°$ case. Given the good agreement between the measurements and CFD, we can look to the computations for insight to the formation of the corner vortex. Figure 24 shows the computed surface pressure coefficient contours and limiting streamlines in the leading-edge region of the wing-fuselage junction for $\alpha = 0°$ and $5°$. The figures also include a rectangular outline of the measurement survey region at $x = 2145$ mm to provide a sense of scale. For the $\alpha = 0°$ case, a nodal point of separation is observed very close to the leading edge of the wing-fuselage junction and almost immediately downstream, there is a nodal point of attachment. As such, a small region of separated flow is formed near the junction leading edge. Several limiting streamlines emanating from a small region near the nodal point of attachment are observed to bend inward, toward the corner, due to the pressure gradient on the leading-edge extension. Further downstream, those limiting streamlines converge onto a local line of separation. This line then serves as the base for a new stream surface (or dividing surface) that extends into the flow [38] and on passage downstream, the stream surface rolls up to form the corner vortex. A similar surface topology exists for the $\alpha = 5°$ case, except here, the nodal points of separation and attachment are shifted down toward the lower surface of the leading-edge extension and the local line of separation is swept further outboard from the corner due to the increased favorable pressure gradient in the spanwise direction. It will be shown later in this section that the corner vortex persists downstream and extends all the way to the wing trailing edge for both α cases.

Another indication of the corner vortex is provided by infrared images of the JF model. For example, consider the infrared image of the junction leading-edge region for $\alpha = 5°$ shown in figure 25a. Here, a streak with a slightly lower image intensity than the surrounding pixels is observed near the corner and extends well downstream. In this case, the lower image intensity corresponds to a lower surface temperature. At $x = 2145$ mm, the spanwise location of this lower-temperature streak corresponds to that where the $\langle U \rangle$-velocity contours (figure 19) indicate a local thickening of the wing boundary layer near the upwash side of the corner vortex. It is hypothesized that the local thickening of the boundary layer lowers the convective heat transfer to the surface (here, the air temperature is warmer than the model surface) resulting in the slightly lower surface tempera-
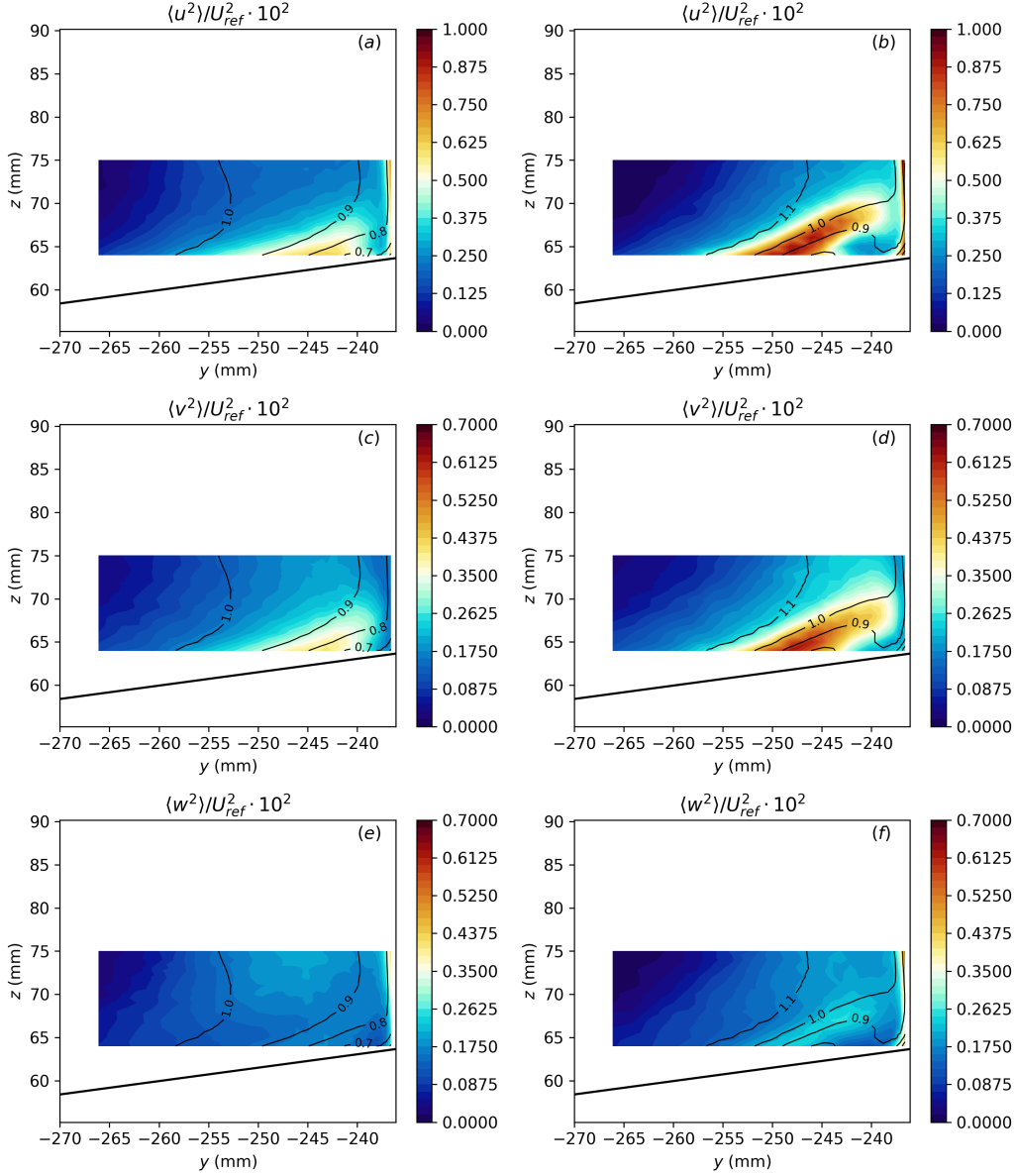
Figure 21: (*a*), (*c*), and (*e*) Contours of the measured Reynolds normal stress components at $x = 2145.0$ mm for $\alpha = 0°$. (*b*), (*d*), and (*f*) Contours of the measured Reynolds normal stress components at $x = 2145.0$ mm for $\alpha = 5°$. The labeled contour lines in the subfigures correspond to the mean velocity, $\langle U \rangle / U_{ref}$, and the solid black line denotes the wing surface.

ture. This hypothesis is consistent with previous studies where longitudinal vortices imbedded in a turbulent boundary were shown to significantly influence the heat-transfer behavior [39, 40]. In particular, the convective heat transfer was found to decrease on the upwash side of the vortex where the momentum and thermal boundary layers are locally thickened by the secondary flow directed away from the wall.

The development of the corner vortex does not appear to be unique to the symmetric-wing geometry that is the focus of this report. Infrared images of the JF model configured with the F6 wing,
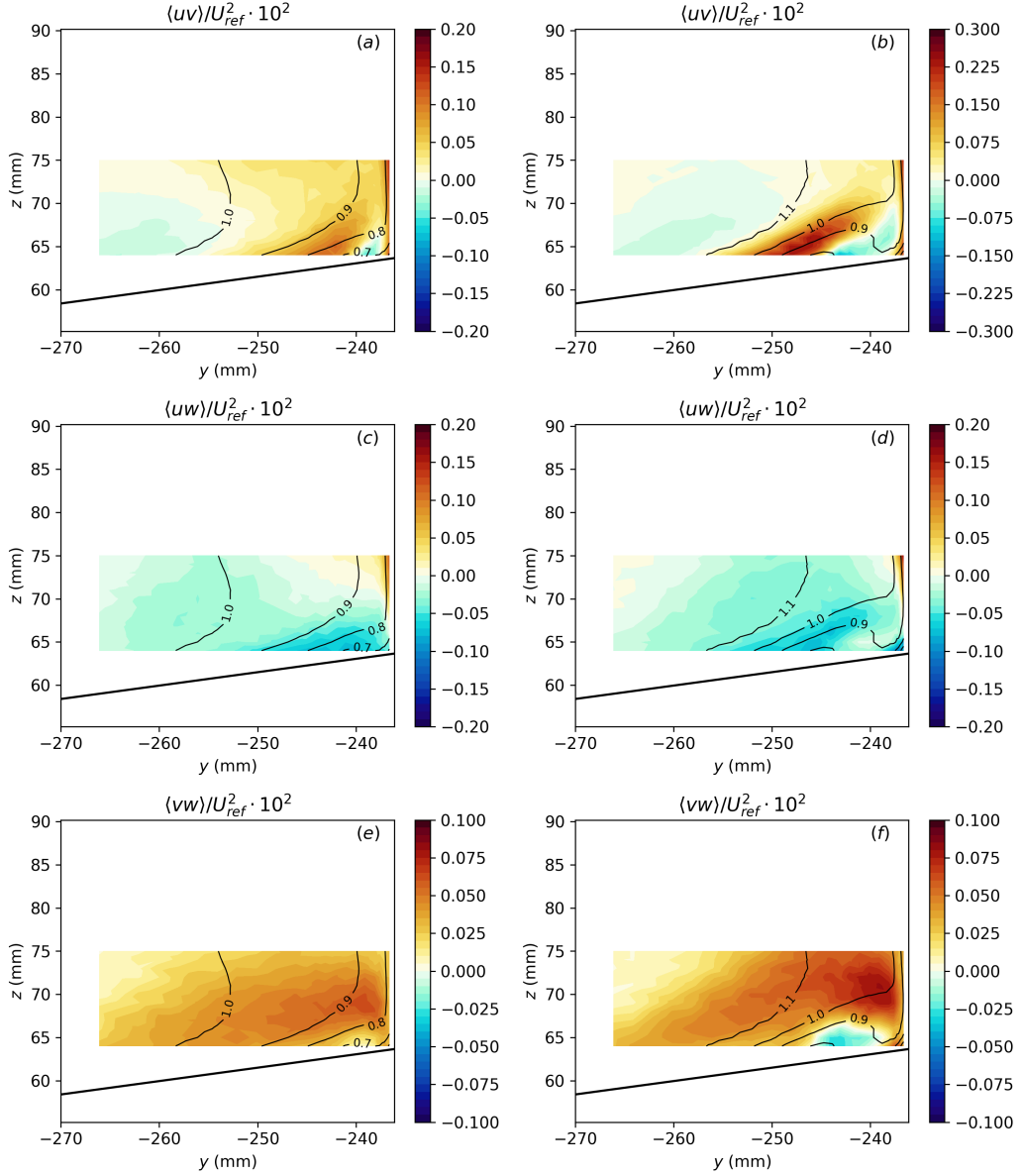
Figure 22: (*a*), (*c*), and (*e*) Contours of the measured Reynolds shear stress components at $x = 2145.0$ mm for $\alpha = 0°$. (*b*), (*d*), and (*f*) Contours of the measured Reynolds shear stress components at $x = 2145.0$ mm for $\alpha = 5°$. The labeled contour lines in the subfigures correspond to the mean velocity, $\langle U \rangle / U_{ref}$, and the solid black line denotes the wing surface.

with and without the leading-edge extension, are shown in figures 25b and c. Both images—which were acquired during previous test entries with the JF model—show evidence of a corner vortex near the wing-fuselage junction. Other studies of wing-surface junctions have documented the development of a corner vortex. Hazarika et al. [41] performed an experimental study of an unswept NACA 65-015 wing mounted to a flat plate and identified a corner vortex in the early development of the corner flow using total-pressure and hot-wire probes. More recently, Bordji et al. [42] performed RANS computations of an unswept NACA 0015 wing with washout twist that was mounted to a flat
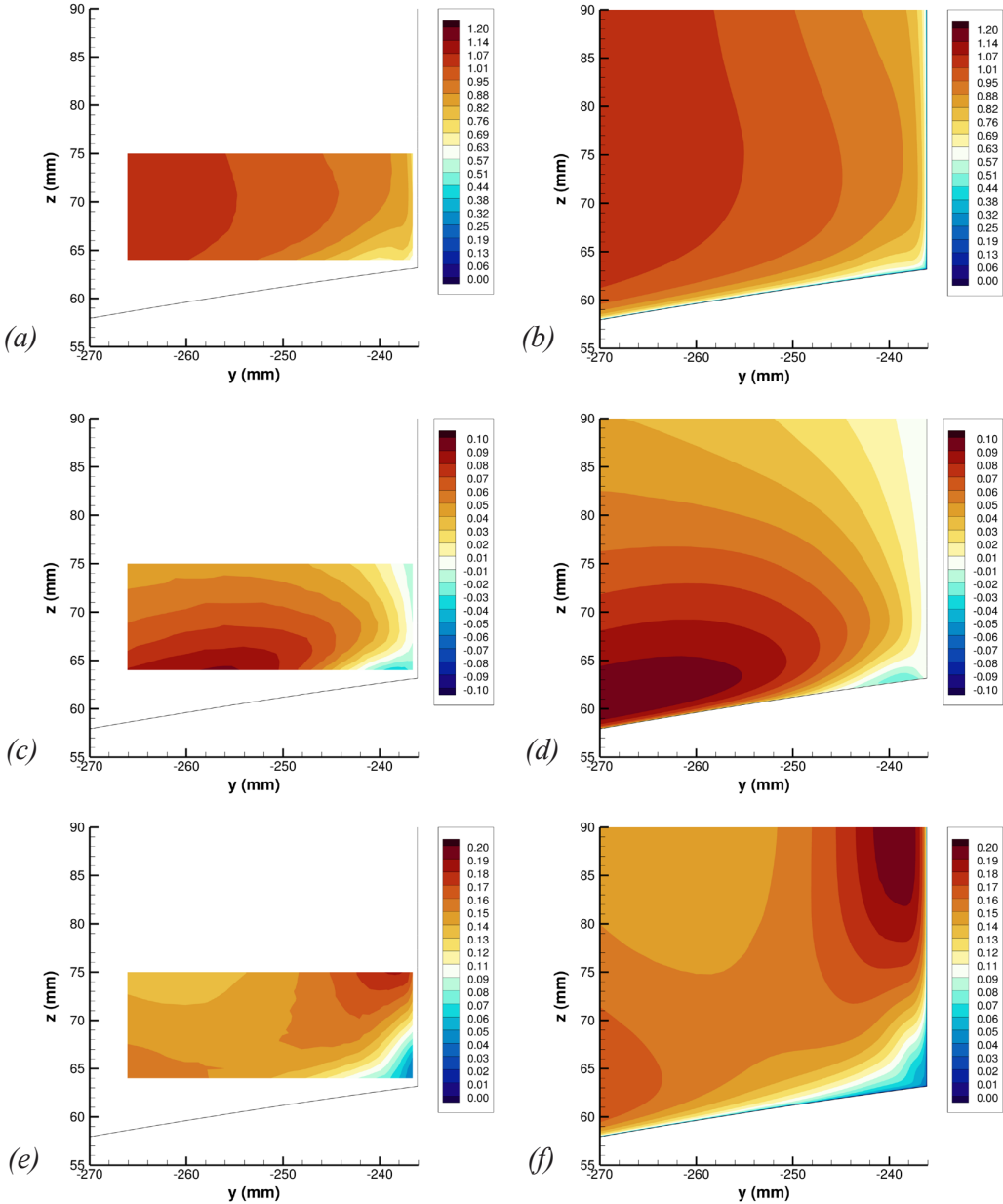
Figure 23: Contours of mean-velocity components at $x = 2145.0$ mm, $\alpha = 0°$. (*a*), (*c*), and (*e*) contours of measured $\langle U \rangle / U_{ref}$, $\langle V \rangle / U_{ref}$, and $\langle W \rangle / U_{ref}$. (*b*), (*d*), and (*f*) contours of computed $\langle U \rangle / U_{ref}$, $\langle V \rangle / U_{ref}$, and $\langle W \rangle / U_{ref}$.

plate and also predicted the occurrence of a corner vortex.

Next, we examine the measurements of the turbulent corner flow in the trailing-edge region of the wing-fuselage junction. Here, the corner flow is developing under an adverse pressure gradient as indicated by the C_p distributions shown in figure 9. Figure 26 presents (y, z)-plane contours of selected mean-flow quantities ($\langle U \rangle$, $\langle V \rangle$, and $\langle \omega_x \rangle$) for several x locations. Data for both $\alpha = 0°$ and $5°$ are included in the plots. The x component of mean vorticity, $\langle \omega_x \rangle = \partial \langle W \rangle / \partial y - \partial \langle V \rangle / \partial z$, was calculated by fitting cubic splines to the $\langle V \rangle$ and $\langle W \rangle$ measurements and then evaluating the
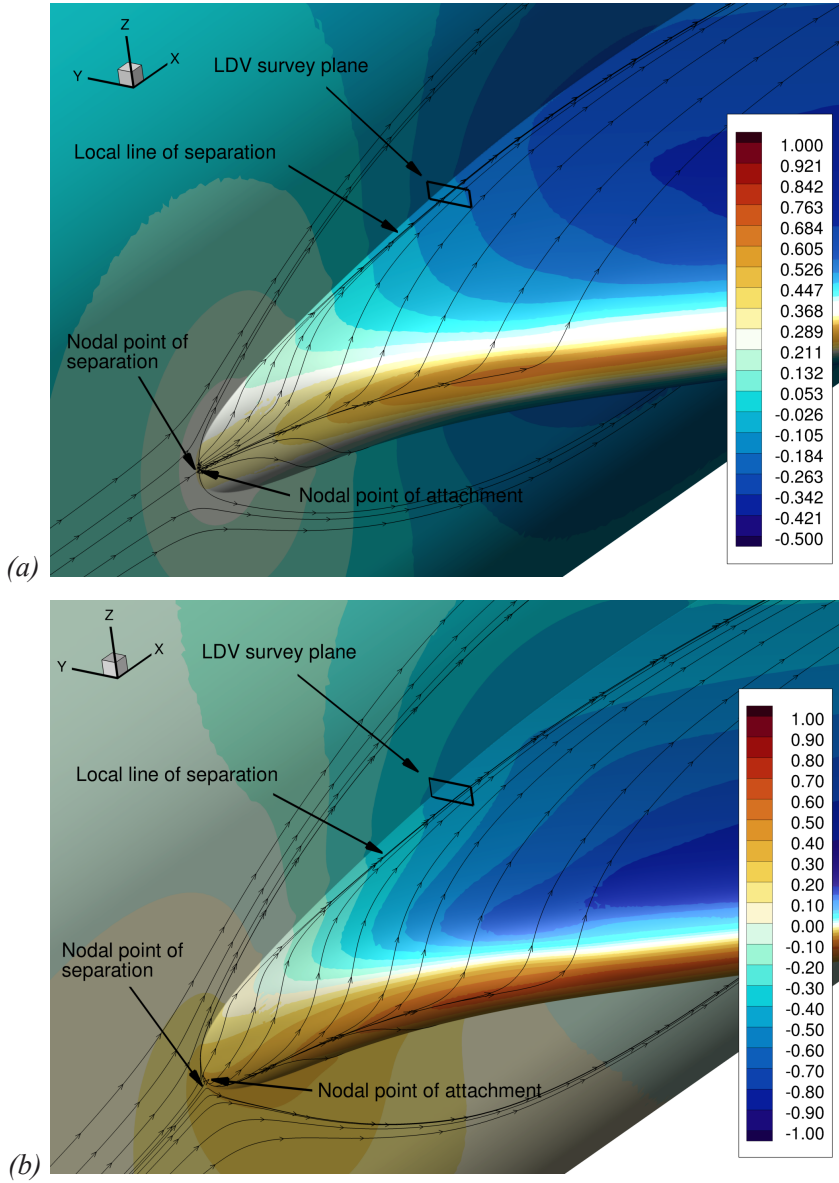
Figure 24: Computed surface pressure coefficient (C_p) contours and limiting streamlines in the leading-edge region of the wing-fuselage junction. (a) $\alpha = 0°$. (b) $\alpha = 5.0°$.

spline derivatives analytically. The contour plots shown in figure 26 provide an overall view and spatial context for the streamwise evolution of the turbulent corner flow in the trailing-edge region.

Figures 27 to 28 provide more detailed views of the contours for the mean-velocity components and the x component of mean vorticity at $x = 2747.6$ mm, 2926.6 mm, and 2961.6 mm ($\hat{x} = 0.796$, 0.966, 0.999) for $\alpha = 0°$ and $5°$. Consider first the $\alpha = 0°$ case, where the corner flow is fully attached all the way to the junction trailing edge. The $\langle U \rangle$-velocity contours (figures 27a, c, and e) show the overall deceleration of the flow with increasing x location due to the adverse pressure gradient and show the growth of the corner flow boundary layers. The $\langle U \rangle$-velocity contours also display significant mean-flow distortion and this is due to the secondary flow in the (y, z) plane. In
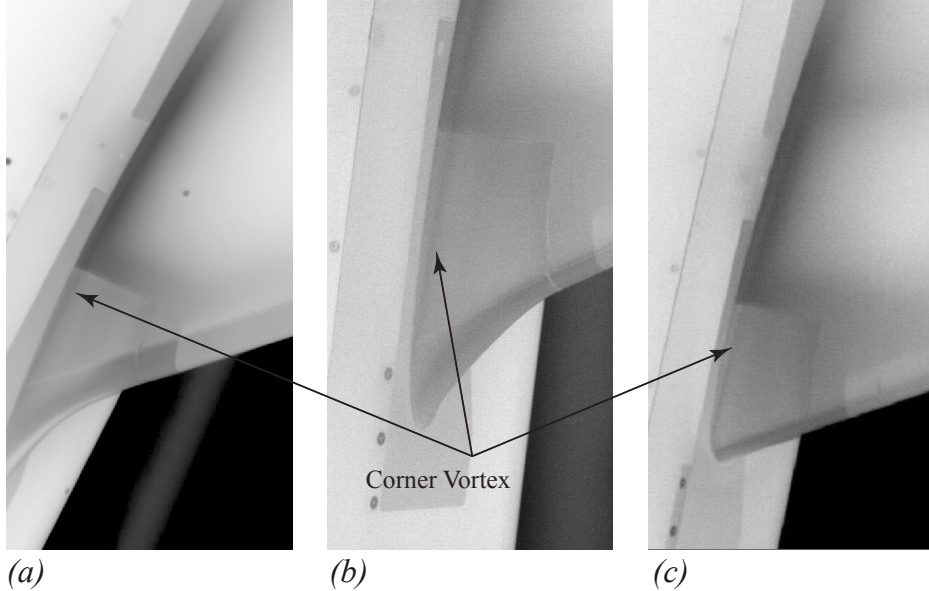
Figure 25: Infrared images of the upper surface of the wing-fuselage junction for $\alpha = 5°$. (*a*) Symmetric wing with leading-edge extension. (*b*) F6 wing with leading-edge extension. (*c*) F6 wing without leading-edge extension.

particular, the mean-flow distortion along the wing surface is driven by the secondary flow associated with the corner vortex that was shown to develop far upstream. The corner vortex, with clockwise rotation when looking upstream, produces a region of negative $\langle \omega_x \rangle$ above the wing surface as seen in figures 28a, c, and e. On the downwash side of the corner vortex, the $\langle U \rangle$ velocity contours along the wing surface indicate local thinning of the boundary layer and on the upwash side, they indicate local thickening of the boundary layer. This pattern of mean-flow distortion, and the associated region of negative $\langle \omega_x \rangle$, is also observed to migrate outboard with increasing x location and that is due to the outboard migration of the corner vortex. Since the spanwise pressure gradient of the swept wing is fairly weak in this region of the corner flow, the outboard migration of the corner vortex is primarily driven by the induced motion from the image vortex beneath the wing surface.

The $\langle U \rangle$-velocity contours display an additional, but more subtle, distortion near the junction corner. This is driven by the secondary flow associated with a stress-induced vortex that has developed deep in the junction corner. This vortex is a key feature of turbulent corner flows that is known to arise from the production of streamwise vorticity by spatial gradients of the Reynolds stresses [11]. The stress-induced vortex, with counterclockwise rotation when looking upstream, produces a local region of increased positive $\langle \omega_x \rangle$ as seen in figures 28a, c, and e. On the downwash side of the stress-induced vortex, the $\langle U \rangle$-velocity contours bend toward the junction corner and on the upwash side, the contours bend away from the fuselage surface.

The mean secondary flow components, $\langle V \rangle$ and $\langle W \rangle$ (figures 29 and 30), display distributions that are consistent with the presence of the corner vortex. Near the wing surface and beneath the corner-vortex core, there is a local region of relatively high negative $\langle V \rangle$ velocity where flow is directed outboard. This enhanced $\langle V \rangle$ velocity, which was previously observed in studies of a longitudinal vortex embedded in a turbulent boundary layer [39,43], suggests the presence of an image vortex beneath the wing surface. Above the corner-vortex core, the $\langle V \rangle$ velocity takes on positive values, directing flow toward the fuselage. The $\langle W \rangle$-velocity contours require careful interpretation. Note that the $\langle W \rangle$ velocity is negative everywhere in the measurement planes (figure 30a, c, and e) and this is due to the chosen body-fixed coordinate system. The flow at these x locations
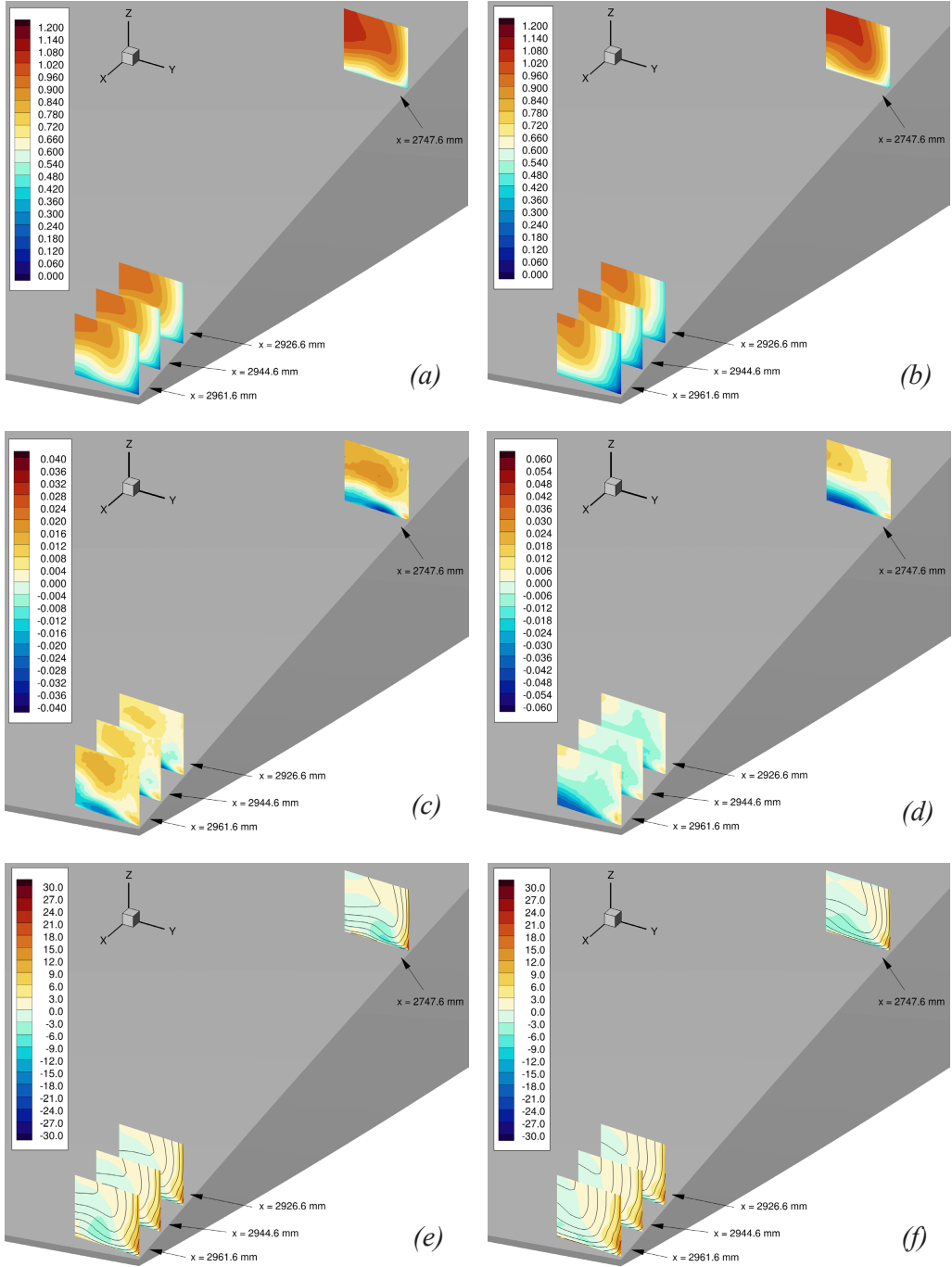
Figure 26: Measured (y, z)-plane contours of selected mean-flow quantities near the wing trailing edge for several x locations. (*a*) and (*b*) $\langle U \rangle / U_{ref}$ at $\alpha = 0°$ and $5°$. (*c*) and (*d*) $\langle V \rangle / U_{ref}$ at $\alpha = 0°$ and $5°$. (*e*) and (*f*) $\langle \omega_x \rangle c / U_{ref}$ at $\alpha = 0°$ and $5°$.

42
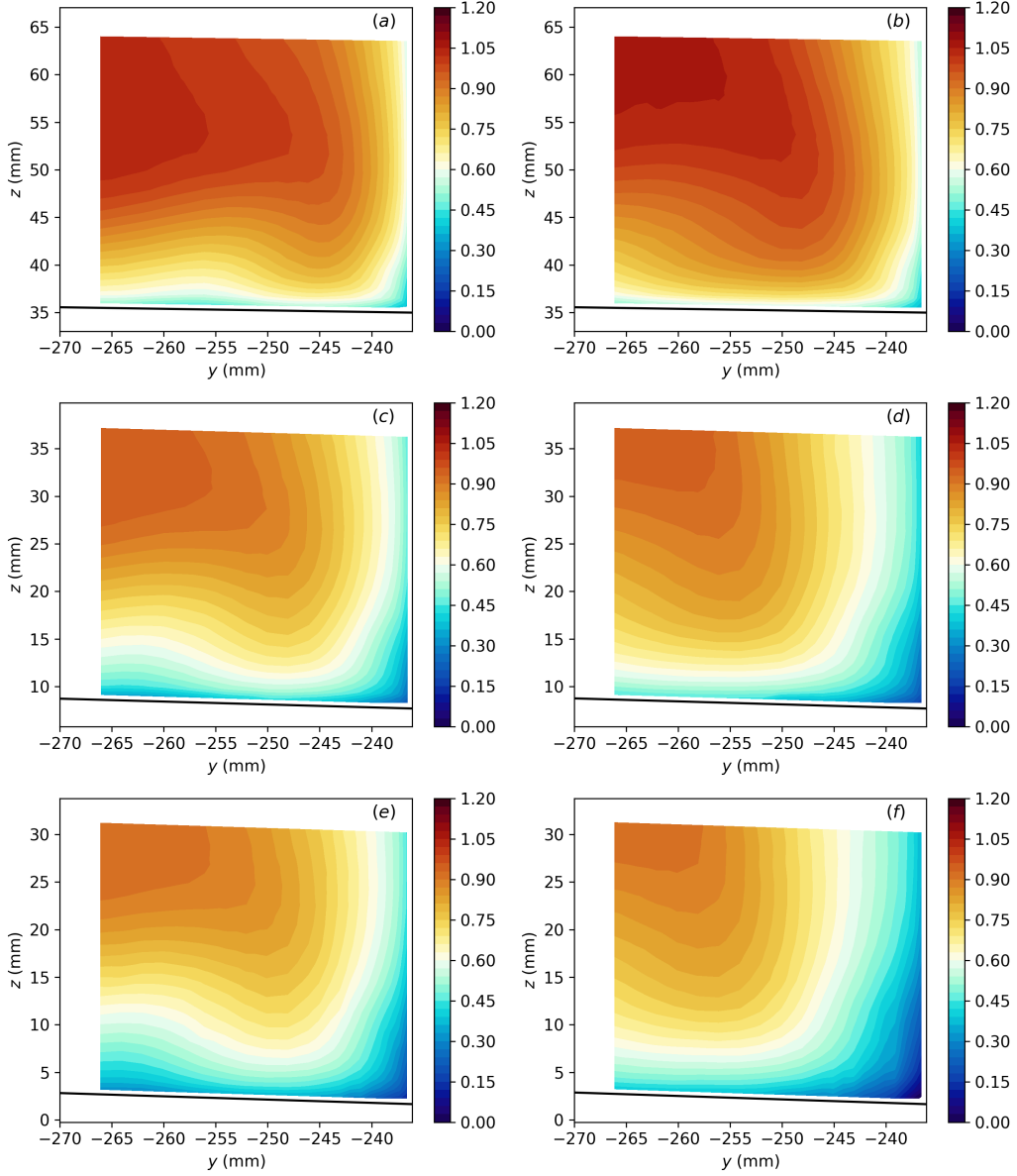
Figure 27: Measured (y, z)-plane contours of $\langle U \rangle / U_{ref}$ for several x locations. (*a*), (*c*), and (*e*) $x = 2747.6$ mm, 2926.6 mm, and 2961.6 mm at $\alpha = 0°$. (*b*), (*d*), and (*f*) $x = 2747.6$ mm, 2926.6 mm, and 2961.6 mm at $\alpha = 5.0°$.

is directed down along the downward-sloping surface of the wing and in the body-fixed coordinate system, this results in a negative $\langle W \rangle$ velocity component. However, there are local variations in the $\langle W \rangle$-velocity contours indicative of the corner vortex. In particular, on the downwash side of the vortex, $\langle W \rangle$ takes on larger negative values and on the upwash side, $\langle W \rangle$ takes on smaller negative values.

The distributions for $\langle V \rangle$ and $\langle W \rangle$ near the junction corner are also consistent with the presence of the stress-induced vortex. Deep in the corner, there is a local region of positive $\langle V \rangle$, where the stress-induced vortex directs the secondary flow toward the corner. Directly above that, there is a
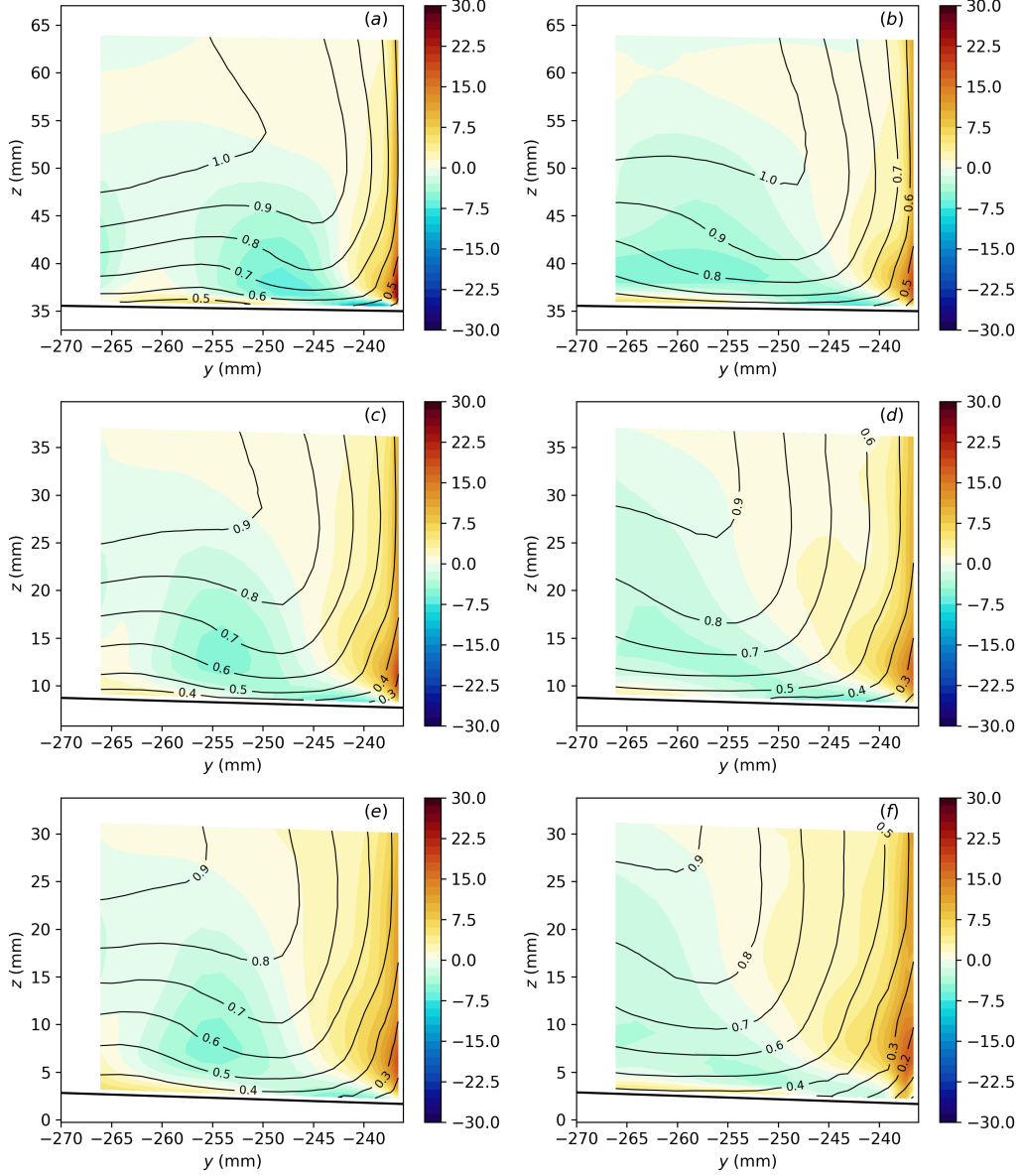
Figure 28: Measured (y, z)-plane contours of $\langle\omega_x\rangle c/U_{ref}$ for several x locations. (*a*), (*c*), and (*e*) $x = 2747.6$ mm, 2926.6 mm, and 2961.6 mm at $\alpha = 0°$. (*b*), (*d*), and (*f*) $x = 2747.6$ mm, 2926.6 mm, and 2961.6 mm at $\alpha = 5.0°$. The black contours lines denote $\langle U \rangle /U_{ref}$ in increments of 0.1.

local region of negative $\langle V \rangle$ where the stress-induced vortex directs the secondary flow away from the fuselage surface and here, the $\langle U \rangle$-velocity contours are observed to bend away from the fuselage surface. The $\langle W \rangle$-velocity contours display a region near the corner and along the fuselage surface where $\langle W \rangle$ has smaller negative values as the stress-induced vortex directs the secondary flow up and away from the corner.

Consider next the $\alpha = 5°$ case, where the corner flow separates near the junction trailing edge (subfigures b, d, and f of figures 27 to 28). In general, the mean-velocity contours and the $\langle\omega_x\rangle$ contours for this case are qualitatively similar to the $\alpha = 0°$ case and most of the foregoing discussion
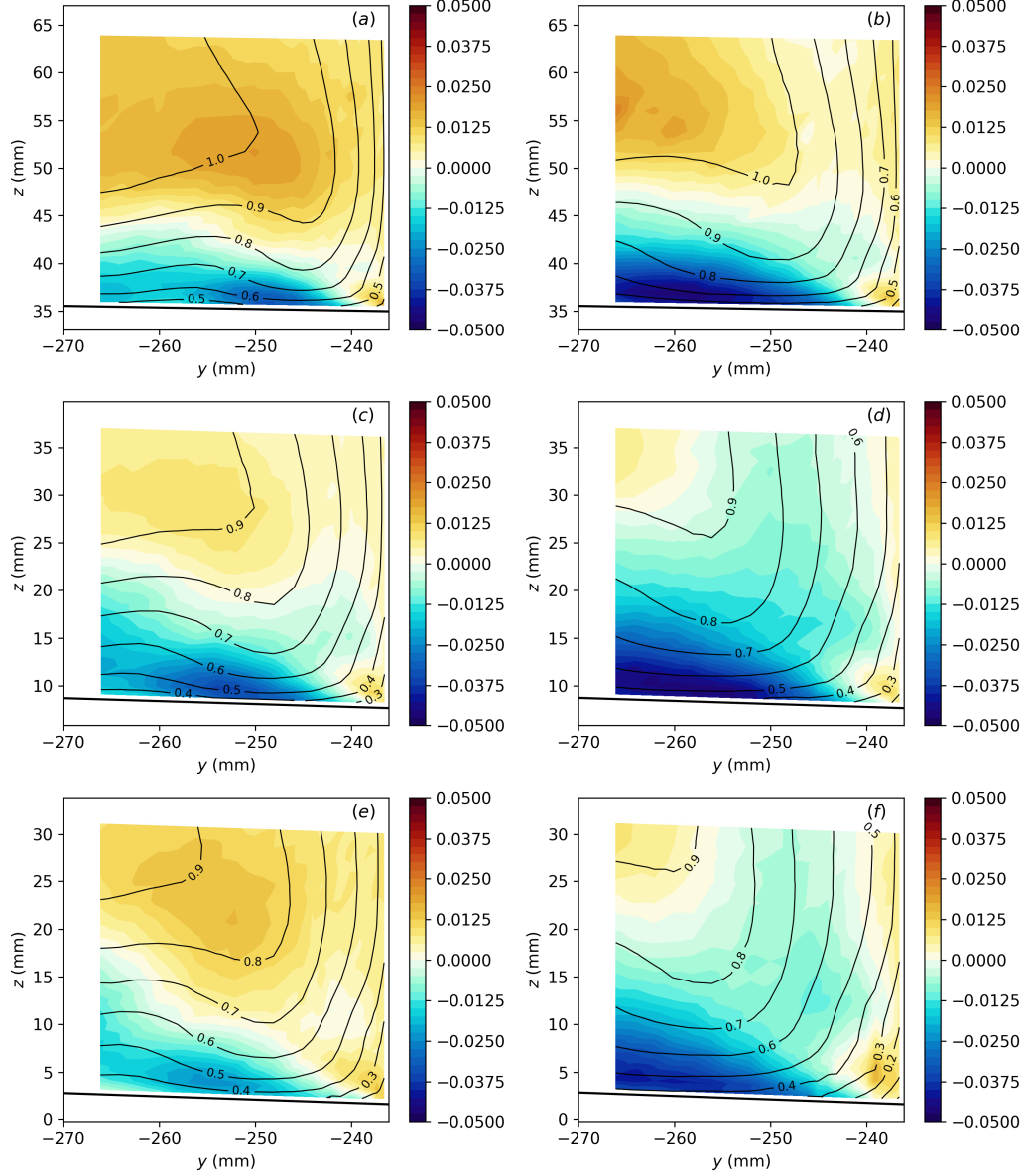
Figure 29: Measured (y, z)-plane contours of $\langle V \rangle / U_{ref}$ for several x locations. (*a*), (*c*), and (*e*) $x = 2747.6$ mm, 2926.6 mm, and 2961.6 mm at $\alpha = 0°$. (*b*), (*d*), and (*f*) $x = 2747.6$ mm, 2926.6 mm, and 2961.6 mm at $\alpha = 5.0°$. The black contours lines denote $\langle U \rangle / U_{ref}$ in increments of 0.1.

applies here. There are, however, a few notable differences. The $\langle U \rangle$-velocity contours indicate a thicker fuselage boundary layer which is due to the increased adverse pressure gradient imposed on the corner flow. In connection with that is a larger region of decelerated flow near the corner, and at the last x location near the trailing edge (figure 27f), there is a small region of reversed flow near the corner where the corner-flow separation has formed. The mean-flow distortion in $\langle U \rangle$, which is associated with the corner vortex, is also observed to move outboard with the increase in α. In part, that is due to the increased strength of the corner vortex and the stronger induced motion from the image vortex. The local region of relatively high negative $\langle V \rangle$ velocity along the wing surface and

45
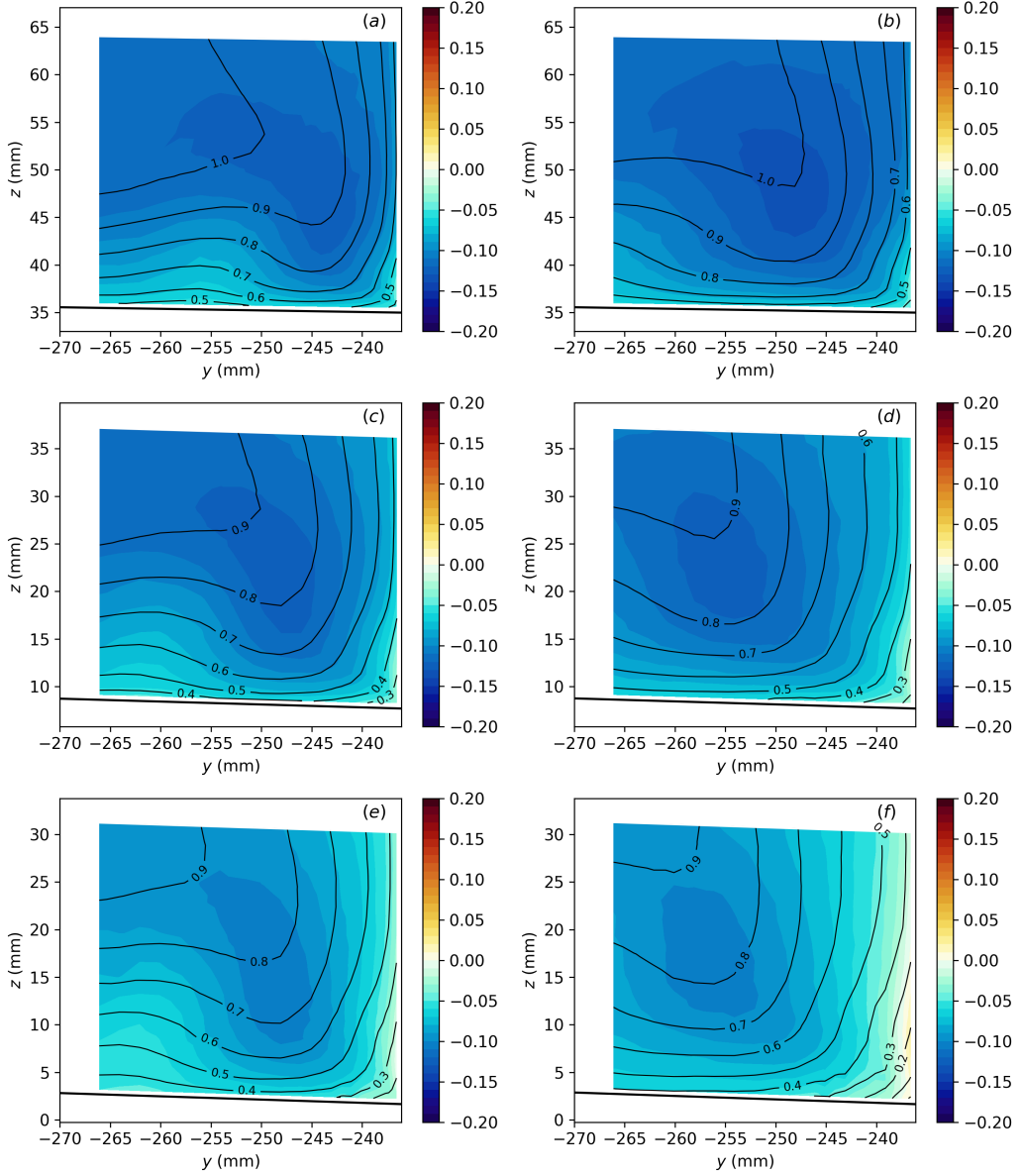
Figure 30: Measured (y, z)-plane contours of $\langle W \rangle / U_{ref}$ for several x locations. (a), (c), and (e) $x = 2747.6$ mm, 2926.6 mm, and 2961.6 mm at $\alpha = 0°$. (b), (d), and (f) $x = 2747.6$ mm, 2926.6 mm, and 2961.6 mm at $\alpha = 5.0°$. The black contours lines denote $\langle U \rangle / U_{ref}$ in increments of 0.1.

below the corner-vortex core (figures 29b, d, and f) again suggests the presence of an image vortex. In this case, however, the magnitude of $\langle V \rangle$ in this region is larger than that for the $\alpha = 0°$ case due to the increased strength of the corner vortex.

Figures 31 to 33 show contours plots of the Reynolds normal-stress components at the foregoing x locations in the junction trailing-edge region for both $\alpha = 0°$ and $\alpha = 5°$. The $\langle u^2 \rangle$ normal-stress distributions (figure 31) show high levels in the fuselage and wing boundary layers. Additionally, the $\langle u^2 \rangle$ normal-stress distributions along the wing surface are strongly distorted by the secondary flow associated with the corner vortex. In the downwash region, high levels of $\langle u^2 \rangle$ are confined
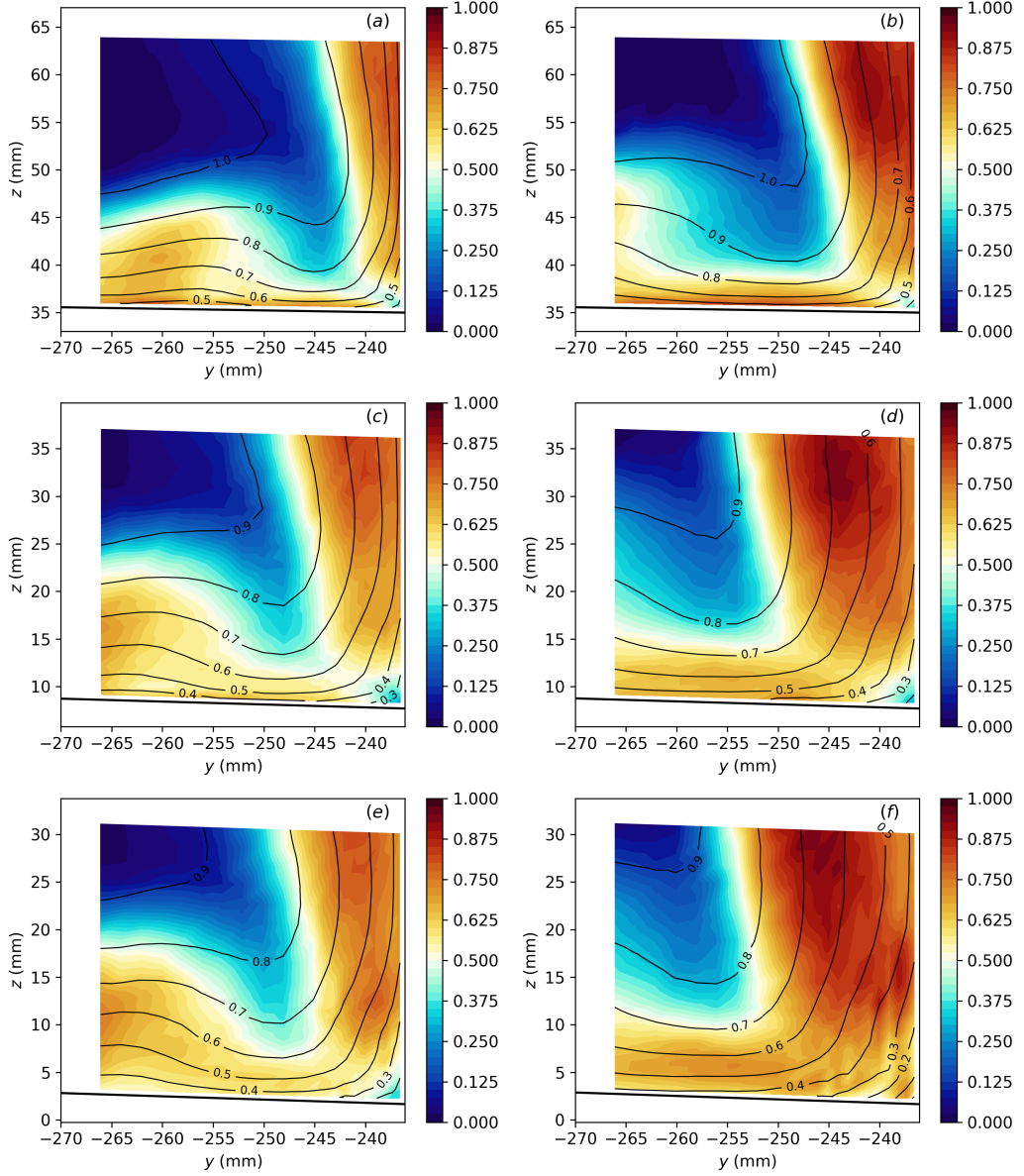
Figure 31: Measured (y, z)-plane contours of $\langle u^2 \rangle / U_{ref}^2 \cdot 10^2$ for several x locations. (a), (c), and (e) $x = 2747.6$ mm, 2926.6 mm, and 2961.6 mm at $\alpha = 0°$. (b), (d), and (f) $x = 2747.6$ mm, 2926.6 mm, and 2961.6 mm at $\alpha = 5.0°$. The black contours lines denote $\langle U \rangle / U_{ref}$ in increments of 0.1.

to a relatively thin layer near the wing surface and in the upwash region, high levels of $\langle u^2 \rangle$ extend up and away from the wall. Deep in the corner of the wing-fuselage junction, the $\langle u^2 \rangle$ levels are attenuated. The $\langle u^2 \rangle$ normal-stress distributions for $\alpha = 0°$ (figures 31a, c, and e) and $\alpha = 5°$ (figures 31b, d, and f) are qualitatively similar, except for $x = 2961.6$ mm at $\alpha = 5°$, where the $\langle u^2 \rangle$ levels deep in the junction corner are high due to the unsteady flow associated with the corner-flow separation for this case. The contours for the $\langle v^2 \rangle$ (figure 32) and $\langle w^2 \rangle$ (figure 33) normal stresses are qualitatively similar to those for $\langle u^2 \rangle$, but have a lower magnitude. Along the fuselage

47
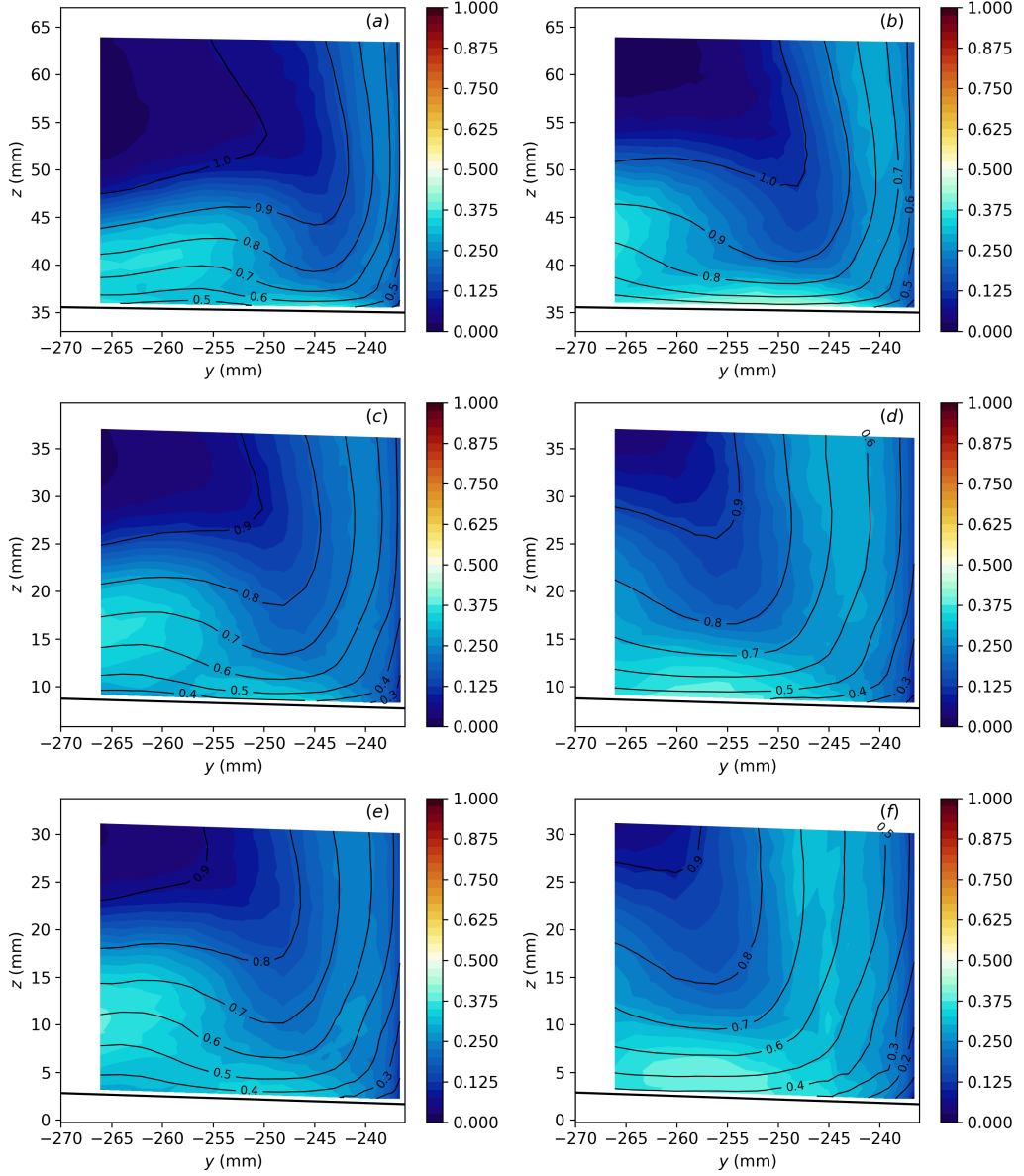
Figure 32: Measured (y, z)-plane contours of $\langle v^2 \rangle /U_{ref}^2 \cdot 10^2$ for several x locations. (a), (c), and (e) $x = 2747.6$ mm, 2926.6 mm, and 2961.6 mm at $\alpha = 0°$. (b), (d), and (f) $x = 2747.6$ mm, 2926.6 mm, and 2961.6 mm at $\alpha = 5.0°$. The black contours lines denote $\langle U \rangle /U_{ref}$ in increments of 0.1.

surface, $\langle v^2 \rangle$ is less than $\langle w^2 \rangle$ due to the constraining effects of the wall, while the opposite is true along the wing surface. This anisotropy in the normal stresses is more readily observed in figure 34, where contours of the difference, $\langle v^2 \rangle - \langle w^2 \rangle$, are plotted. As shown by Perkins [11], gradients of this normal-stress difference contribute to the production of $\langle \omega_x \rangle$, which is an important driver for the generation of the stress-induced vortex that was identified earlier in the mean-velocity contours.

Contours of the Reynolds shear-stress components at the same x locations and angles of incidence are shown in figures 35, 36, and 37. The measured distributions for the primary shear-stress
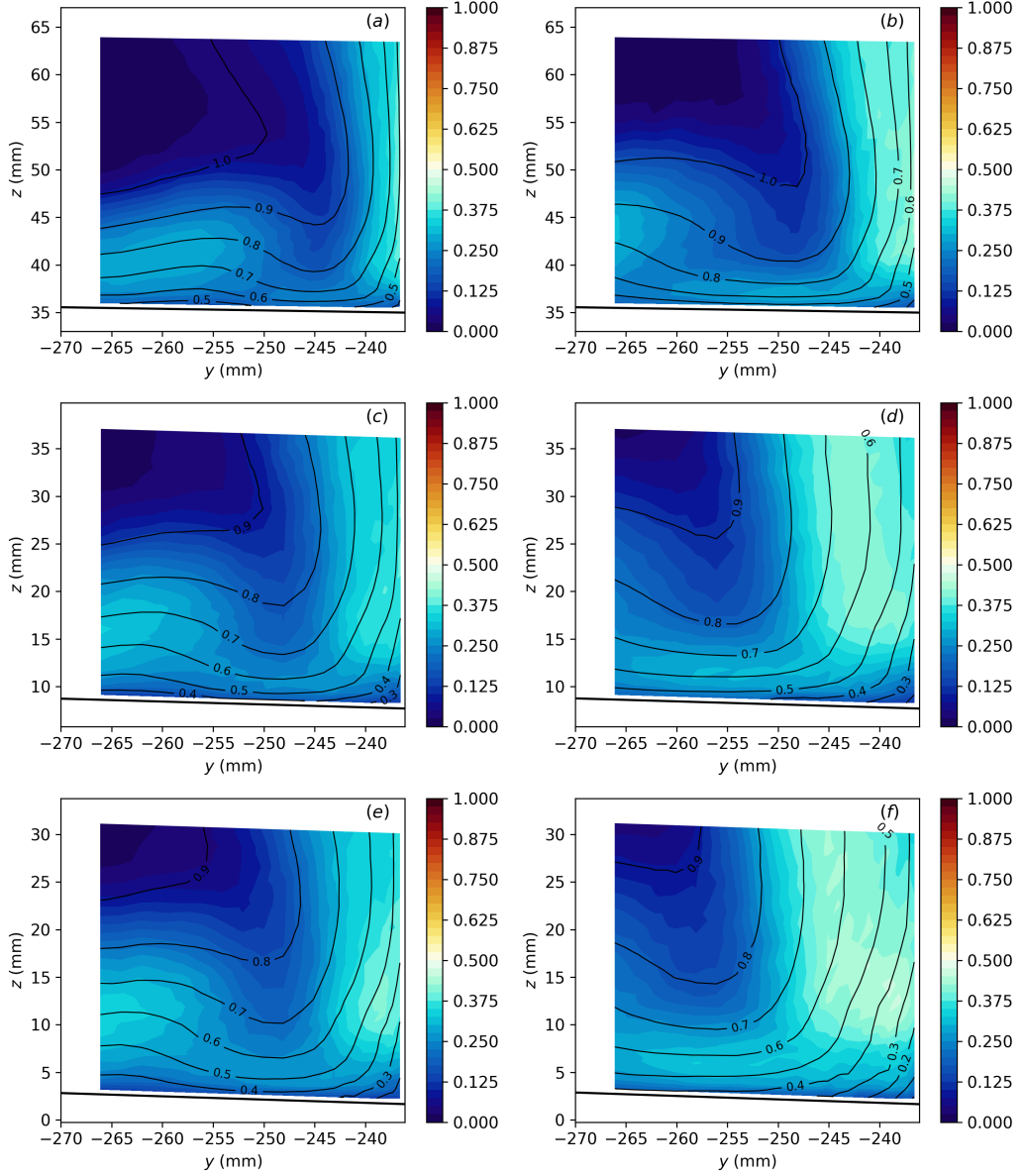
Figure 33: Measured (y, z)-plane contours of $\langle w^2 \rangle / U_{ref}^2 \cdot 10^2$ for several x locations. (a), (c), and (e) $x = 2747.6$ mm, 2926.6 mm, and 2961.6 mm at $\alpha = 0°$. (b), (d), and (f) $x = 2747.6$ mm, 2926.6 mm, and 2961.6 mm at $\alpha = 5.0°$. The black contours lines denote $\langle U \rangle / U_{ref}$ in increments of 0.1.

components, $\langle uv \rangle$ and $\langle uw \rangle$, can be understood in view of a linear eddy-viscosity model:

$$\langle u_i u_j \rangle = -\nu_T \left(\frac{\partial \langle U_i \rangle}{\partial x_j} + \frac{\partial \langle U_j \rangle}{\partial x_i} \right) + \frac{2}{3} k \delta_{ij}, \qquad (11)$$

where ν_T is the turbulent or eddy viscosity and k is the turbulent kinetic energy. Previous studies of turbulent corner flows by Perkins [11] and Bordji et al. [42] support this relationship for the primary
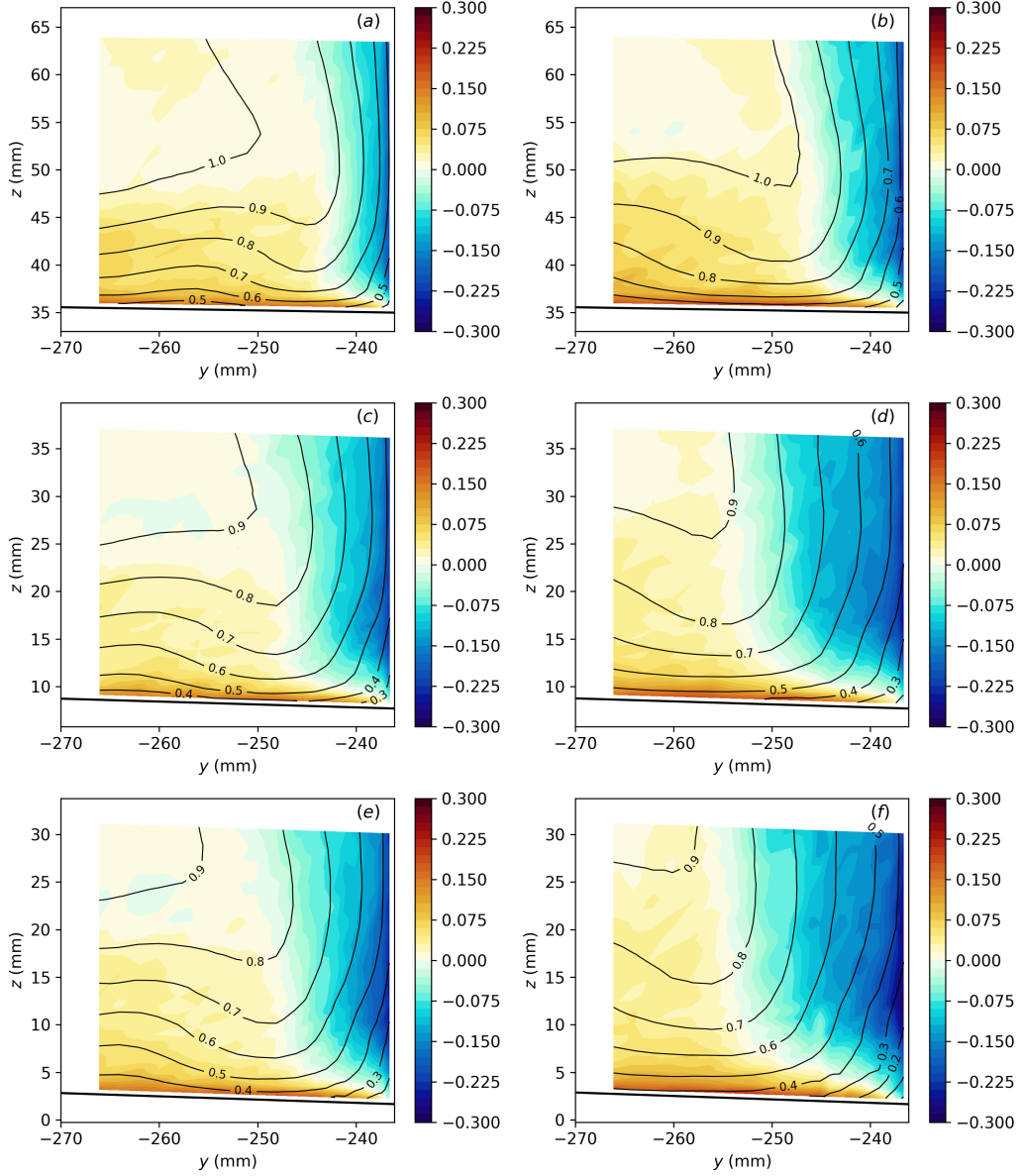
Figure 34: Measured (y, z)-plane contours of the anisotropy of the Reynolds normal stresses, $\left(\langle v^2 \rangle - \langle w^2 \rangle\right) / U_{ref}^2 \cdot 10^2$, for several x locations. (a), (c), and (e) $x = 2747.6$ mm, 2926.6 mm, and 2961.6 mm at $\alpha = 0°$. (b), (d), and (f) $x = 2747.6$ mm, 2926.6 mm, and 2961.6 mm at $\alpha = 5.0°$. The black contours lines denote $\langle U \rangle / U_{ref}$ in increments of 0.1.

shear-stress components. Assuming that the flow is evolving slowly in the x direction we have:

$$\langle uv \rangle = -\nu_T \left(\frac{\partial \langle U \rangle}{\partial y} + \frac{\partial \langle V \rangle}{\partial x} \right) \approx -\nu_T \frac{\partial \langle U \rangle}{\partial y} \tag{12}$$

and

$$\langle uw \rangle = -\nu_T \left(\frac{\partial \langle U \rangle}{\partial z} + \frac{\partial \langle W \rangle}{\partial x} \right) \approx -\nu_T \frac{\partial \langle U \rangle}{\partial z}. \tag{13}$$

50
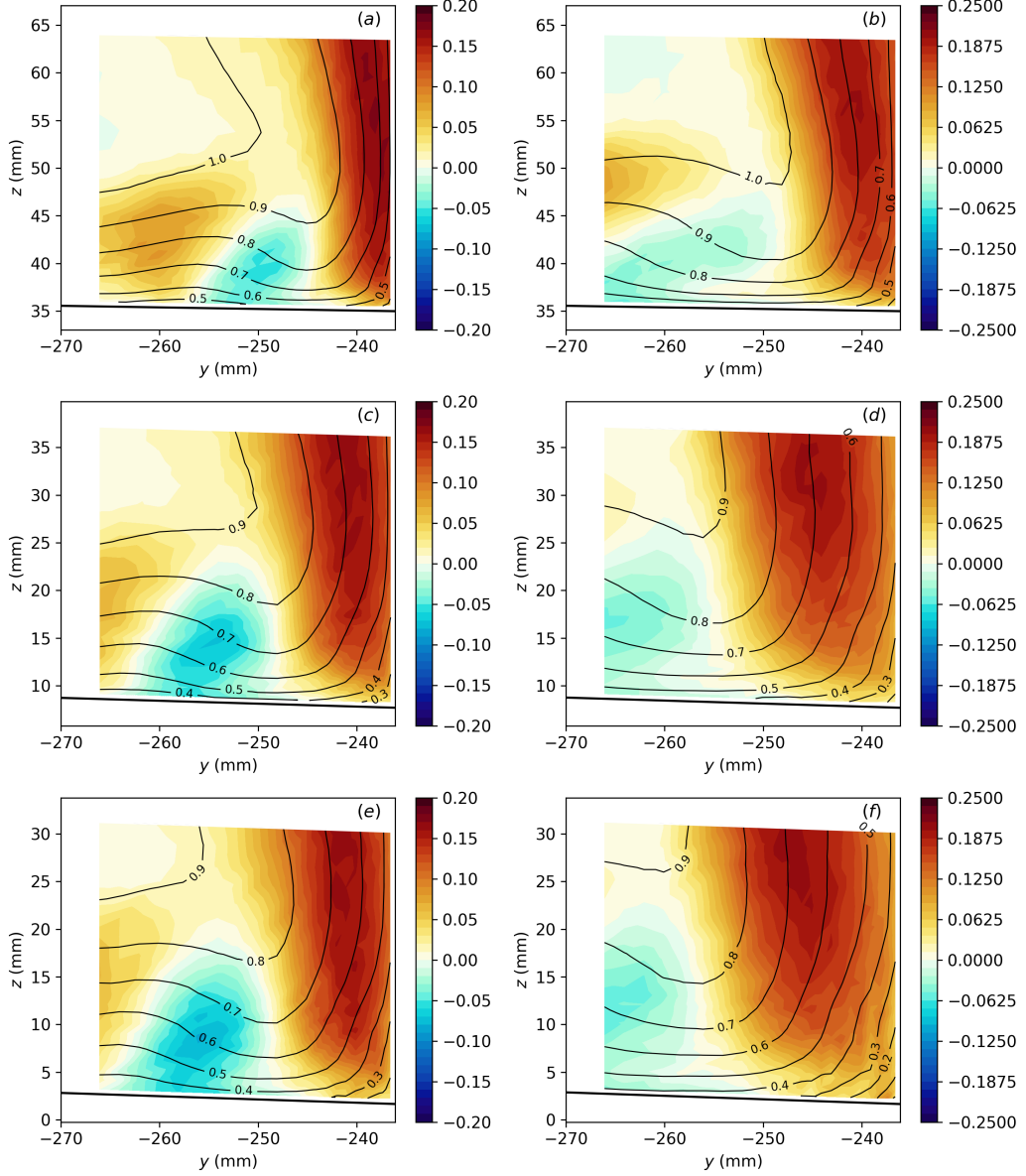
Figure 35: Measured (y, z)-plane contours of $\langle uv \rangle / U_{ref}^2 \cdot 10^2$ for several x locations. (*a*), (*c*), and (*e*) $x = 2747.6$ mm, 2926.6 mm, and 2961.6 mm at $\alpha = 0°$. (*b*), (*d*), and (*f*) $x = 2747.6$ mm, 2926.6 mm, and 2961.6 mm at $\alpha = 5.0°$. The black contours lines denote $\langle U \rangle / U_{ref}$ in increments of 0.1.

Consider first the contours for the primary shear stress, $\langle uv \rangle$, shown in figure 35. Near the fuselage surface, $\partial \langle U \rangle / \partial y$ becomes large and negative and we observe high levels of positive $\langle uv \rangle$ in accordance with equation 12. Along the wing surface, $\partial \langle U \rangle / \partial y$ changes sign across the upwash region of the corner vortex, with a negative local minimum on the outboard side and a positive local maximum on the inboard side. As such, there are corresponding local maximum and local minimum for $\langle uv \rangle$ on the outboard and inboard side of the upwash region, respectively. Next, consider the contours for the primary shear stress, $\langle uw \rangle$, shown in figure 36. Near the wing surface, $\partial \langle U \rangle / \partial z$
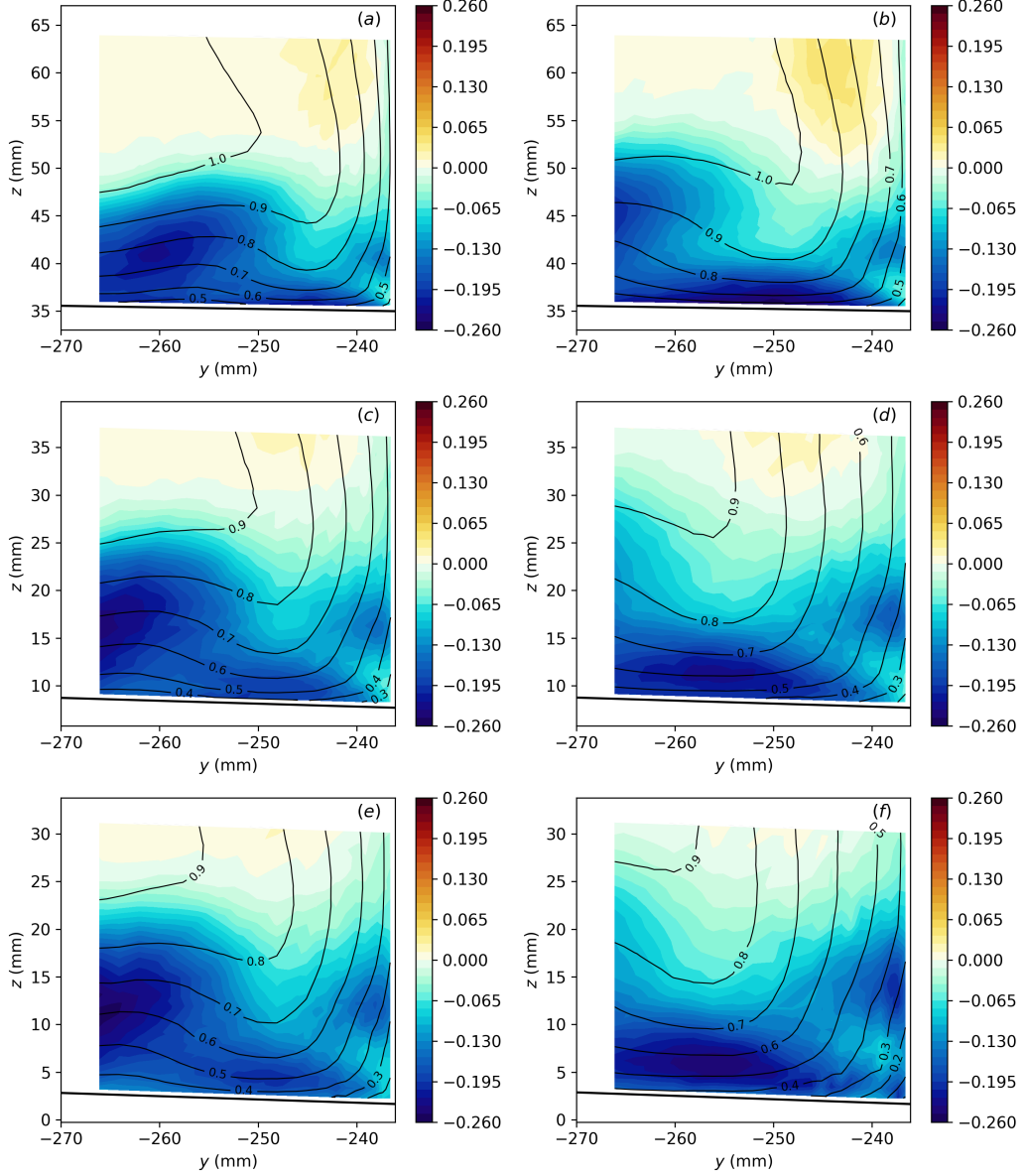
Figure 36: Measured (y, z)-plane contours of $\langle uw \rangle / U_{ref}^2 \cdot 10^2$ for several x locations. (a), (c), and (e) $x = 2747.6$ mm, 2926.6 mm, and 2961.6 mm at $\alpha = 0°$. (b), (d), and (f) $x = 2747.6$ mm, 2926.6 mm, and 2961.6 mm at $\alpha = 5.0°$. The black contours lines denote $\langle U \rangle / U_{ref}$ in increments of 0.1.

is large and positive and here we observe high levels of negative $\langle uw \rangle$ in accordance with equation 13. However, this shear stress is modulated by the distortions in $\langle U \rangle$ that are caused by the corner and stress-induced vortices. Up and away from the wing surface, where $\partial \langle U \rangle / \partial z$ is much less, the $\langle uw \rangle$ shear-stress levels are greatly reduced.

In view of the contours for the secondary shear stress, $\langle vw \rangle$ (figure 37), the most notable feature is the development of positive values roughly along the corner bisector, where the fuselage and wing boundary layers are merged. Unlike the primary shear stresses, however, the spatial distribution
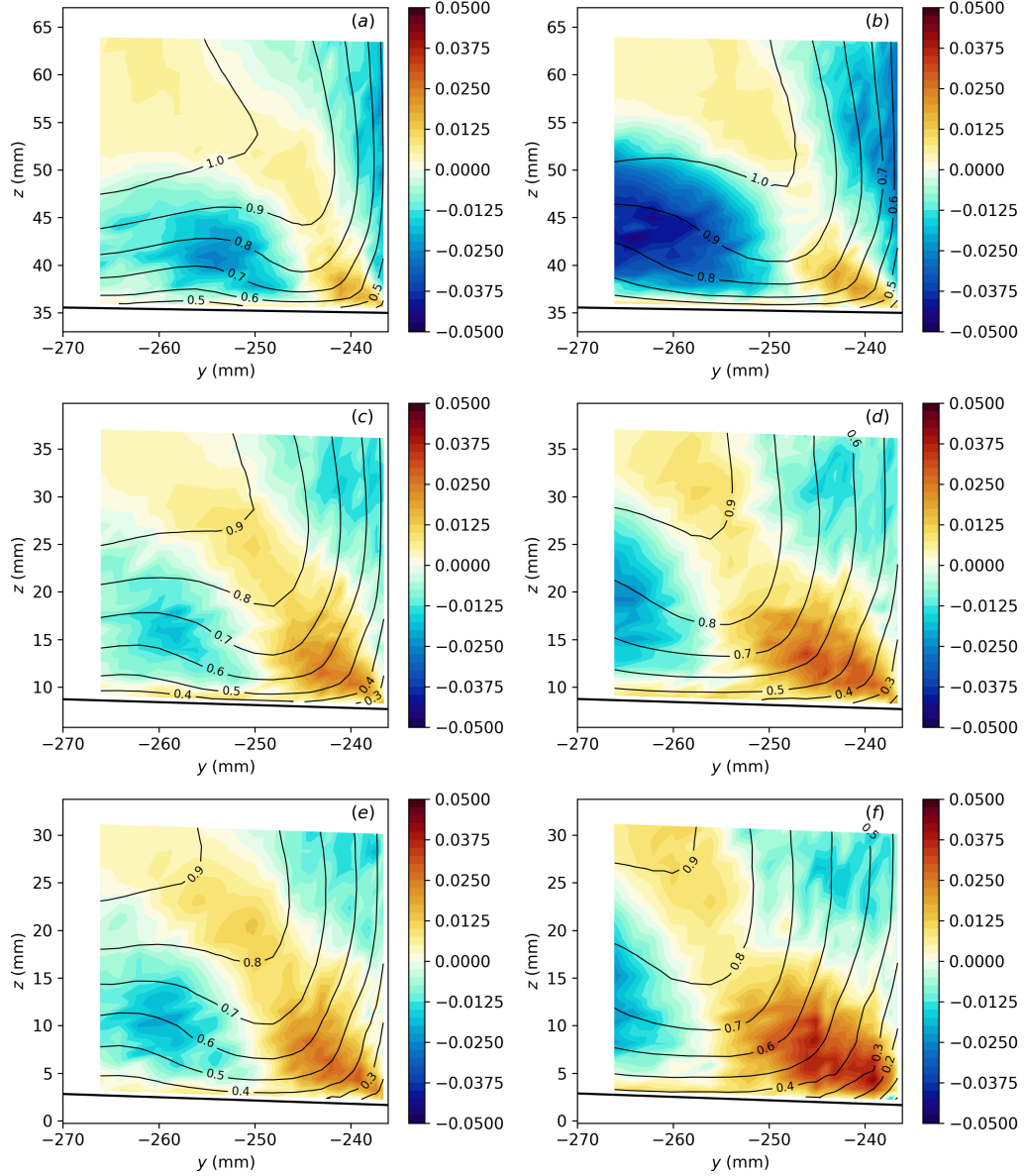
Figure 37: Measured (y, z)-plane contours of $\langle vw \rangle / U_{ref}^2 \cdot 10^2$ for several x locations. (a), (c), and (e) $x = 2747.6$ mm, 2926.6 mm, and 2961.6 mm at $\alpha = 0°$. (b), (d), and (f) $x = 2747.6$ mm, 2926.6 mm, and 2961.6 mm at $\alpha = 5.0°$. The black contours lines denote $\langle U \rangle / U_{ref}$ in increments of 0.1.

for $\langle vw \rangle$ cannot be described by a linear eddy-viscosity model. In other words, $\langle vw \rangle$ does not appear to be proportional to the mean strain rate $\partial \langle V \rangle / \partial z + \partial \langle W \rangle / \partial y$ as suggested by equation 11. This has important implications for computations of turbulent corner flows with RANS CFD used in conjunction with a linear eddy-viscosity model. In addition to gradients in the normal-stress difference, $\langle v^2 \rangle - \langle w^2 \rangle$, gradients in $\langle vw \rangle$ can also contribute to the production of $\langle \omega_x \rangle$ and therefore the generation of the stress-induced vortex [11]. Since neither of these quantities are properly predicted with a linear eddy-viscosity model, RANS CFD with such models cannot predict the occurrence of the stress-induced vortex. That has negative consequences for predicting the onset of corner-flow separation in wing-body junctions. The stress-induced vortex transports momentum into the corner and thereby reenergizes the corner boundary layer as it develops under an adverse pressure gradient. That, in turn, acts to delay or reduce the corner-flow separation. For RANS CFD with a linear eddy-viscosity model, the absence of the stress-induced vortex results in a corner-flow separation that occurs much earlier than what is shown by experimental measurements [12, 42].

Some additional insight to the Reynolds-stress distributions in the trailing-edge region of the junction corner can be obtained from the transport equation for the Reynolds stresses:

$$\frac{\partial}{\partial t} \langle u_i u_j \rangle + \langle U_k \rangle \frac{\partial \langle u_i u_j \rangle}{\partial x_k} = P_{ij} + \epsilon_{ij} + \Pi_{ij} - \frac{\partial C_{ijk}}{\partial x_k} + \nu \frac{\partial^2}{\partial x_k^2} \langle u_i u_j \rangle , \tag{14}$$

where

$$P_{ij} = - \langle u_i u_k \rangle \frac{\partial \langle U_j \rangle}{\partial x_k} - \langle u_j u_k \rangle \frac{\partial \langle U_i \rangle}{\partial x_k}, \tag{15}$$

$$\epsilon_{ij} = 2\nu \left\langle \frac{\partial u_i}{\partial x_k} \frac{\partial u_j}{\partial x_k} \right\rangle , \tag{16}$$

$$\Pi_{ij} = \left\langle p' \left(\frac{\partial u_i}{\partial x_j} + \frac{\partial u_j}{\partial x_i} \right) \right\rangle , \tag{17}$$

$$C_{ijk} = \langle u_i u_j u_k + p' u_i \delta_{jk} + p' u_j \delta_{ik} \rangle \tag{18}$$

are the production, dissipation, pressure-strain correlation, and third-order diffusion correlation, respectively. Unfortunately, many of the terms in the Reynolds-stress transport equation cannot be calculated with our available experimental data, and so we cannot perform a complete budget for the Reynolds stresses. For example, we do not have measurements of the fluctuating pressure, p', or the fluctuating strain rate, $\partial u_i / \partial x_k$. And although we can calculate the triple correlations $\langle u_i u_j u_k \rangle$ from our experimental data, they have relatively high uncertainties due to the low number of sample averages and so we cannot obtain reliable estimates for the turbulent diffusion term $\partial \langle u_i u_j u_k \rangle / \partial x_k$. However, assuming that the corner flow is developing slowly in the x direction and therefore neglecting the gradients in x, we can obtain estimates of the Reynolds-stress production terms from equation 15. To that end, gradients in the mean-velocity components were calculated by fitting cubic splines to the $\langle U \rangle$, $\langle V \rangle$, and $\langle W \rangle$ velocities for a given (y, z) plane and then evaluating the spline derivatives analytically. In the following discussion, we will focus on the production terms for the (y, z) plane at $x = 2747.6$ mm and $\alpha = 0°$, as this is qualitatively representative of the measurements at the other locations in the trailing-edge region of the junction.

Figure 38 shows contours of the normal-stress components along with contours of the total production for each component. From equation 15, the normal-stress production terms are given by:

$$P_{\langle u^2 \rangle} \approx -2 \langle uv \rangle \frac{\partial \langle U \rangle}{\partial y} - 2 \langle uw \rangle \frac{\partial \langle U \rangle}{\partial z}, \tag{19}$$

$$P_{\langle v^2 \rangle} \approx -2 \langle v^2 \rangle \frac{\partial \langle V \rangle}{\partial y} - 2 \langle vw \rangle \frac{\partial \langle V \rangle}{\partial z}, \tag{20}$$

and

$$P_{\langle w^2 \rangle} \approx -2 \langle w^2 \rangle \frac{\partial \langle W \rangle}{\partial z} - 2 \langle vw \rangle \frac{\partial \langle W \rangle}{\partial y}. \tag{21}$$

54

The production of $\langle u^2 \rangle$ is shown in figure 38b and it has a spatial distribution similar to $\langle u^2 \rangle$, suggesting that production is largely responsible for the high levels of $\langle u^2 \rangle$ that are observed in the corner flow boundary layers. Examining the relative magnitudes of the terms in equation 19 indicates that along the fuselage surface, the $-2 \langle uv \rangle \, \partial \langle U \rangle / \partial y$ term is the dominant contributor to the total production, while along the wing surface and in the upwash region of the corner vortex, the $-2 \langle uw \rangle \, \partial \langle U \rangle / \partial z$ term is the dominant contributor to the total production. In contrast, the production for $\langle v^2 \rangle$ and $\langle w^2 \rangle$ shown in figures 38d and f is essentially zero to within the experimental uncertainty. In a canonical turbulent boundary layer, it is known that all of the turbulent kinetic energy production is in $\langle u^2 \rangle$ and that the fluctuating pressure acts to redistribute the energy from $\langle u^2 \rangle$ to the $\langle v^2 \rangle$ and $\langle w^2 \rangle$ components [44]. This redistributive effect is likely an important source of energy for the $\langle v^2 \rangle$ and $\langle w^2 \rangle$ normal-stress components in the present case as well.

Figure 39 shows contours of the shear-stress components along with contours of the total production for each component. From equation 15, the shear-stress production terms are given by:

$$P_{\langle uv \rangle} \approx - \langle uv \rangle \, \frac{\partial \langle V \rangle}{\partial y} - \langle uw \rangle \, \frac{\partial \langle V \rangle}{\partial z} - \langle v^2 \rangle \, \frac{\partial \langle U \rangle}{\partial y} - \langle vw \rangle \, \frac{\partial \langle U \rangle}{\partial z}, \tag{22}$$

$$P_{\langle uw \rangle} \approx - \langle uv \rangle \, \frac{\partial \langle W \rangle}{\partial y} - \langle uw \rangle \, \frac{\partial \langle W \rangle}{\partial z} - \langle w^2 \rangle \, \frac{\partial \langle U \rangle}{\partial z} - \langle vw \rangle \, \frac{\partial \langle U \rangle}{\partial y}, \tag{23}$$

and

$$P_{\langle vw \rangle} \approx - \langle v^2 \rangle \, \frac{\partial \langle W \rangle}{\partial y} - \langle w^2 \rangle \, \frac{\partial \langle V \rangle}{\partial z} - \langle vw \rangle \left(\frac{\partial \langle W \rangle}{\partial z} + \frac{\partial \langle V \rangle}{\partial y} \right). \tag{24}$$

The production for the primary shear stresses $\langle uv \rangle$ and $\langle uw \rangle$ is shown in figures 39b and d, and both have spatial distributions that are similar to their respective shear-stress components. This suggests that production is largely responsible for the observed spatial distributions of $\langle uv \rangle$ and $\langle uw \rangle$. For $\langle uv \rangle$, the relative magnitudes of the terms in equation 22 indicate that the $- \langle v^2 \rangle \, \partial \langle U \rangle / \partial y$ term is the dominant contributor to the total production. For $\langle uw \rangle$, the relative magnitudes of the production terms indicate that the $- \langle w^2 \rangle \, \partial \langle U \rangle / \partial z$ is the main contributor to the total production. The contours of the production for the secondary shear stress $\langle vw \rangle$ is shown in figure 39f. Here, the production bears some resemblance to the spatial distribution of $\langle vw \rangle$ except in the immediate vicinity of the corner, where there is no positive production that contributes to the observed positive value of $\langle vw \rangle$ along the corner bisector. The generation of the secondary shear-stress levels in this region of the corner flow must be driven by other processes, such as pressure redistribution or turbulent diffusion. An examination of the production terms in equation 24 indicates that the last term $- \langle vw \rangle \left(\partial \langle W \rangle / \partial z + \partial \langle V \rangle / \partial y \right)$ is small relative to the other production terms.

From the oil-flow visualizations presented in section 4.1, we found that the wing-fuselage corner flow was fully attached for $\alpha = 0°$ and $\alpha = 1°$, and a small corner-flow separation occurred for $\alpha = 5°$. In contrast, the CFD predicted a small corner-flow separation for all three angles of incidence. The question then is what differences in the flowfield quantities, if any, contribute to the predicted early onset of corner-flow separation? In the following discussion, we will consider the flowfield measurements and computations for the (y, z) plane at $x = 2747.6$ mm and $\alpha = 0°$. The differences between the experiment and CFD at this location are generally representative of those at other x locations in the trailing-edge region of the junction and at different angles of incidence.

Contours of the mean velocity, normal-stress components, and shear-stress components for the experiment and CFD are compared in figures 40, 41, and 42, respectively. Overall, the predicted quantities shown in these figures are in good qualitative agreement with the experiment, and the similarities in the spatial distributions suggest that the turbulence model used for the CFD (SA-RC-QCR2020) captures the key flow physics of the turbulent corner flow. However, quantitative differences do exist. In terms of the mean-velocity components, the predicted $\langle U \rangle$ contours display less mean-flow distortion, suggesting that the secondary flow associated with the corner and stress-induced vortices is somewhat weaker. This is supported by the secondary-flow components, where the predicted $\langle V \rangle$ velocity deep in the junction corner and the predicted $\langle W \rangle$ velocity in the upwash
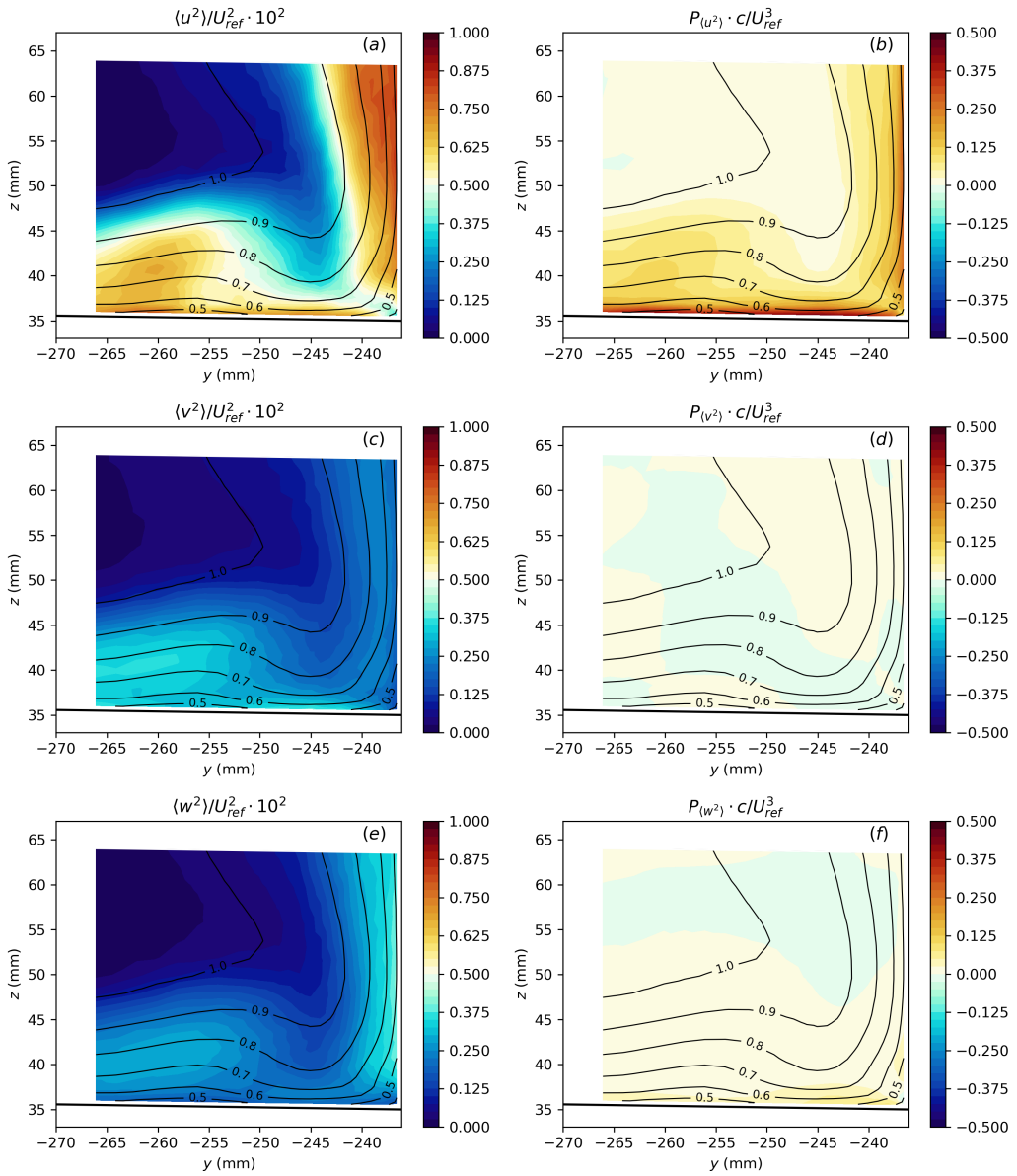
Figure 38: Contours of $\langle u_i^2 \rangle$ and contours of the production of $\langle u_i^2 \rangle$ at $x = 2747.6$ mm and $\alpha = 0°$. (a) $\langle u^2 \rangle / U_{ref}^2 \cdot 10^2$. (b) $P_{\langle u^2 \rangle} c / U_{ref}^3$. (c) $\langle v^2 \rangle / U_{ref}^2 \cdot 10^2$. (d) $P_{\langle v^2 \rangle} c / U_{ref}^3$. (e) $\langle w^2 \rangle / U_{ref}^2 \cdot 10^2$. (f) $P_{\langle w^2 \rangle} c / U_{ref}^3$. The black contours lines denote $\langle U \rangle / U_{ref}$ in increments of 0.1.

region of the corner vortex are both weaker than the experimental measurements. Of particular importance is the weaker secondary flow deep in the junction corner, that implies a weaker stress-induced vortex as compared to the experiment. Since the strength of the stress-induced vortex is expected to play a key role in the onset of corner-flow separation, this difference may partly explain why a small corner-flow separation is predicted further downstream, while the experiment indicates a fully attached corner flow all the way to the junction trailing edge.

In terms of the normal-stress components (figure 41), the $\langle u^2 \rangle$ normal stress is generally under-predicted, and the CFD does not capture the strong enhancement of $\langle u^2 \rangle$ in the upwash region of
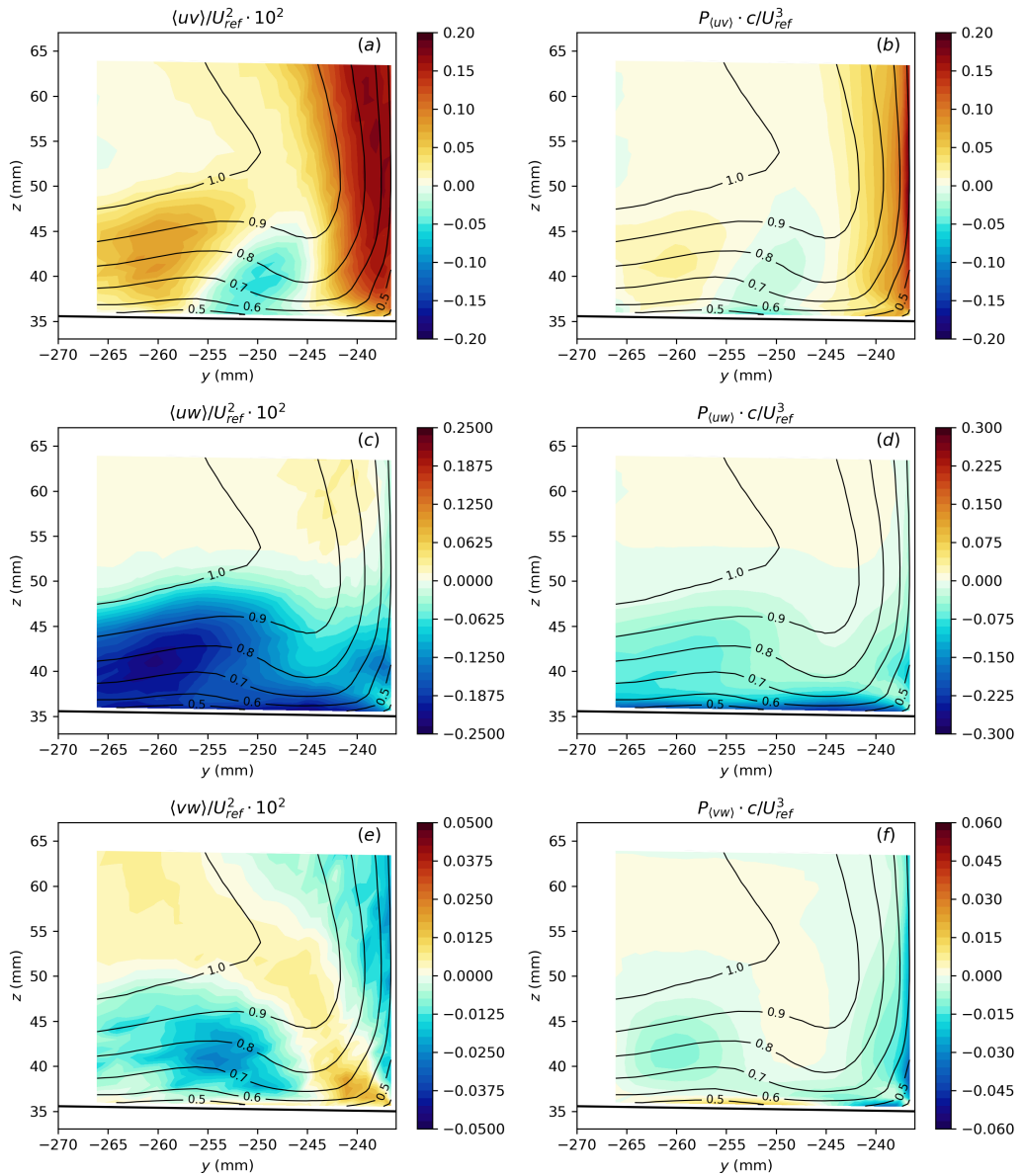
Figure 39: Contours of $\langle u_i u_j \rangle$ and contours of the production of $\langle u_i u_j \rangle$ at $x = 2747.6$ mm and $\alpha = 0°$. (a) $\langle uv \rangle / U_{ref}^2 \cdot 10^2$. (b) $P_{\langle uv \rangle} c / U_{ref}^3$. (c) $\langle uw \rangle / U_{ref}^2 \cdot 10^2$. (d) $P_{\langle uw \rangle} c / U_{ref}^3$. (e) $\langle vw \rangle / U_{ref}^2 \cdot 10^2$. (f) $P_{\langle vw \rangle} c / U_{ref}^3$. The black contours lines denote $\langle U \rangle / U_{ref}$ in increments of 0.1.

the corner vortex. For the $\langle v^2 \rangle$ and $\langle w^2 \rangle$ normal stresses, the CFD qualitatively captures the correct anisotropy across the corner bisector, but it also generally overpredicts the levels of both $\langle v^2 \rangle$ and $\langle w^2 \rangle$. In terms of the shear-stress components (figure 42), the predicted levels of both primary shear stresses, $\langle uv \rangle$ and $\langle uw \rangle$, are generally underpredicted and there are also spatial differences relative to the experiment. For $\langle uw \rangle$, the spatial distribution associated with the stress-induced vortex is not captured even qualitatively. For the secondary shear stress component, the most notable difference between the experiment and CFD is the apparent overprediction of $\langle vw \rangle$ in the vicinity of the corner bisector.
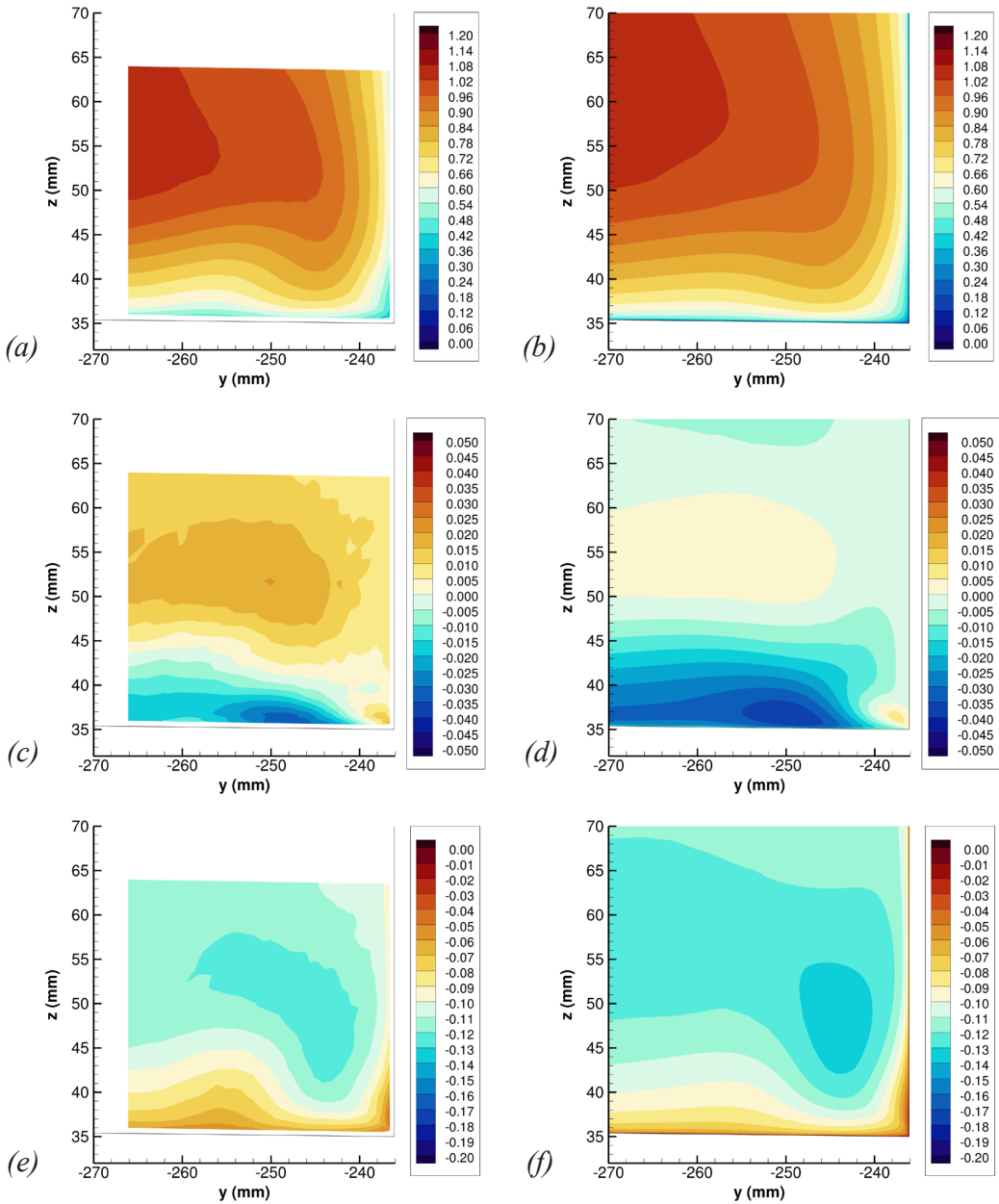
Figure 40: Contours of mean-velocity components at $x = 2747.6$ mm and $\alpha = 0°$. (a) and (b) $\langle U \rangle / U_{ref}$ for experiment and CFD. (c) and (d) $\langle V \rangle / U_{ref}$ for experiment and CFD. (e) and (f) $\langle W \rangle / U_{ref}$ for experiment and CFD.

A more quantitative comparison between the experiment and CFD is provided in figure 43, where z-direction profiles of the mean-velocity components and the Reynolds stresses are plotted at three spanwise locations. Here, the symbols denote the experimental data, the solid lines denote the CFD predictions, and the shaded bands about the experimental data represent the measurement uncertainty. The first location at $y = -237.35$ mm is deep within the fuselage boundary layer and cuts through the stress-induced vortex, the second location at $y = -246.1$ mm is influenced by the down-
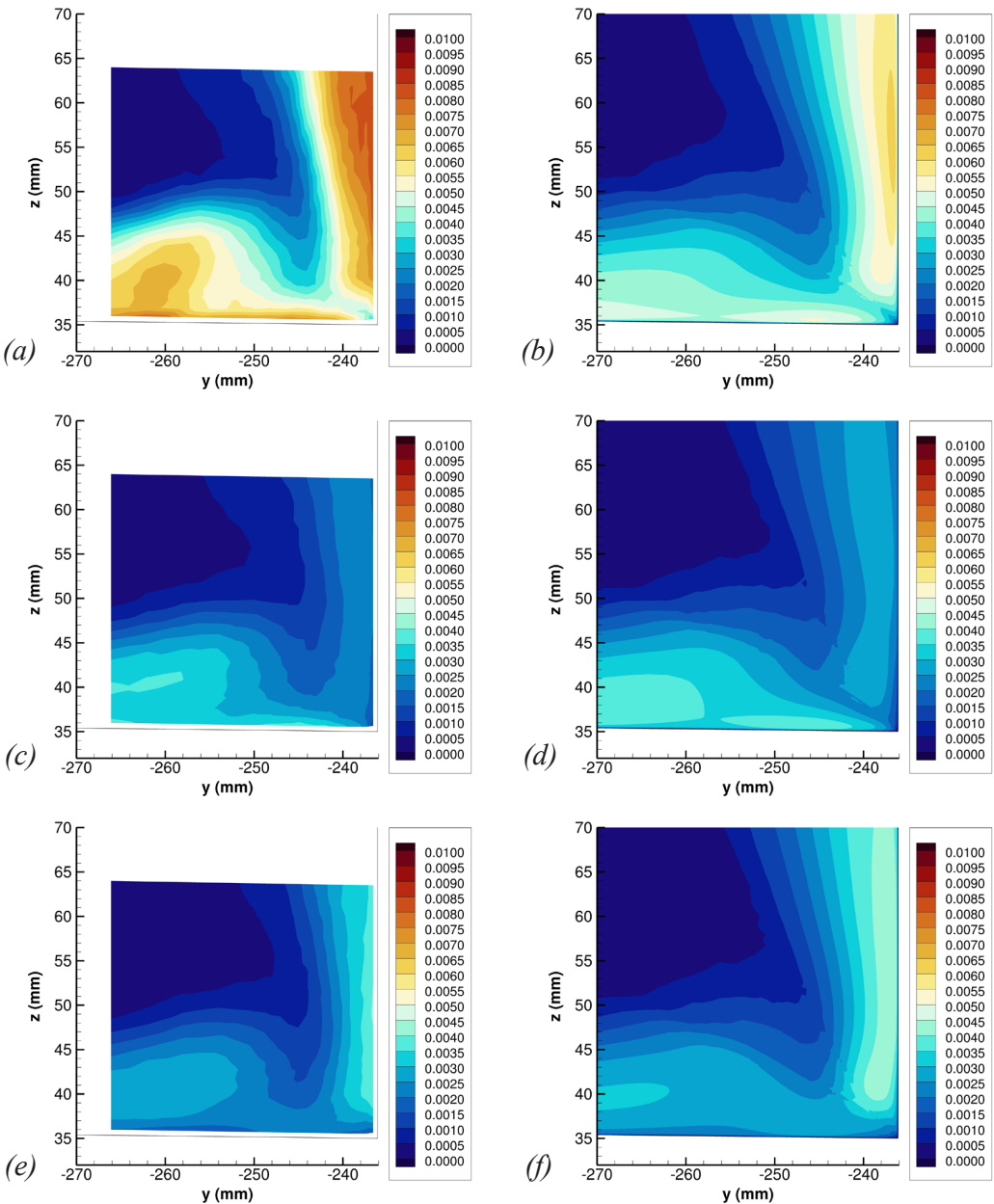
Figure 41: Contours of Reynolds normal-stress components at $x = 2747.6$ mm and $\alpha = 0°$. (*a*) and (*b*) $\langle u^2 \rangle / U_{ref}^2$ for experiment and CFD. (*c*) and (*d*) $\langle v^2 \rangle / U_{ref}^2$ for experiment and CFD. (*e*) and (*f*) $\langle w^2 \rangle / U_{ref}^2$ for experiment and CFD.

wash region of the corner vortex, and the third location at $y = -262.1$ mm is near or just outboard of the upwash region of the corner vortex. In terms of the mean-velocity components, the overall agreement between the experimental data and CFD is good, but small quantitative differences—larger than the measurement uncertainty—can be observed. For the normal-stress profiles, the CFD underpredicts $\langle u^2 \rangle$ and overpredicts both $\langle v^2 \rangle$ and $\langle w^2 \rangle$ relative to the experiment, with differences that are generally larger than the measurement uncertainty. However, there is still good qualitative
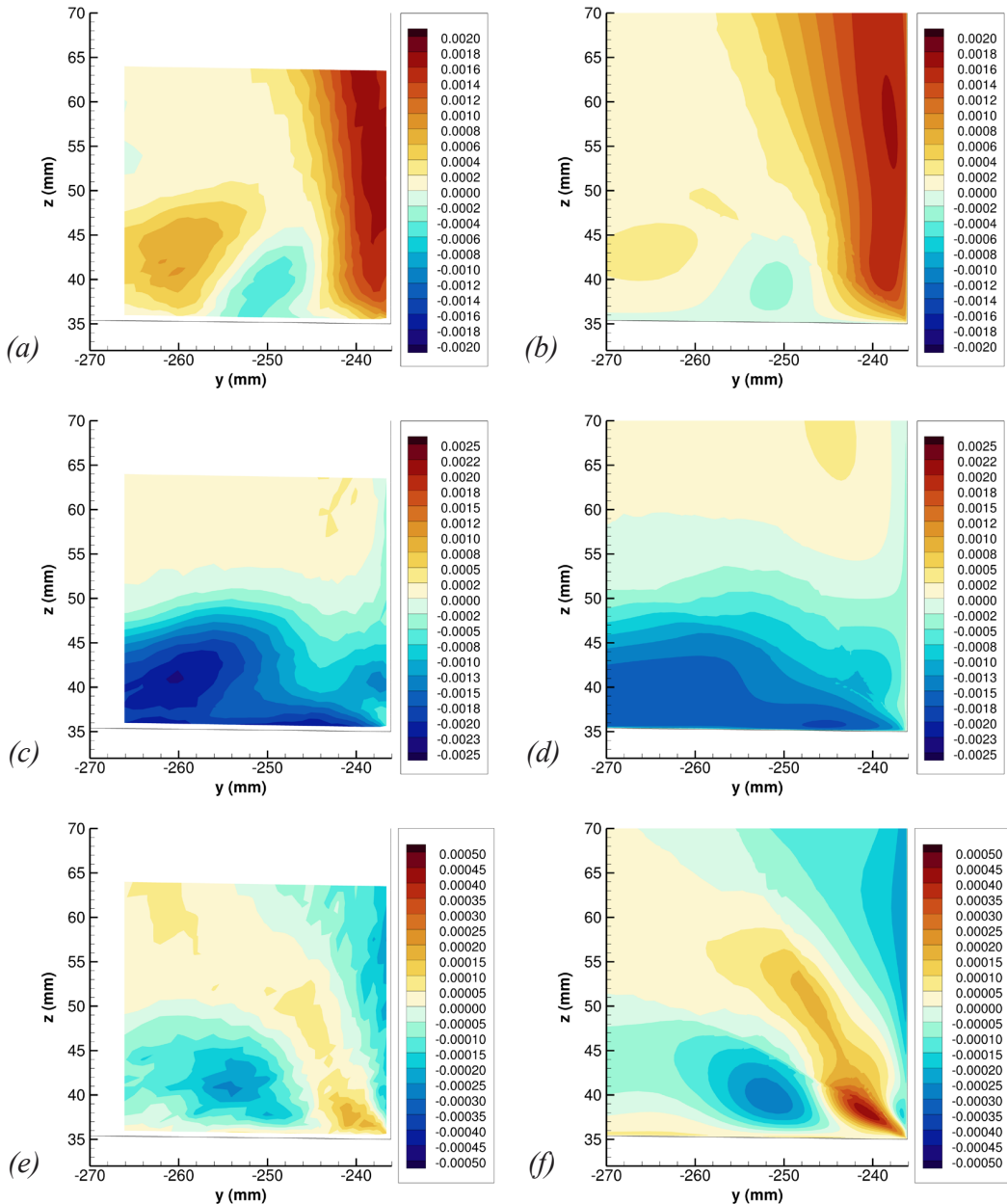
Figure 42: Contours of Reynolds shear-stress components at $x = 2747.6$ mm and $\alpha = 0°$. (*a*) and (*b*) $\langle uv \rangle / U_{ref}^2$ for experiment and CFD. (*c*) and (*d*) $\langle uw \rangle / U_{ref}^2$ for experiment and CFD. (*e*) and (*f*) $\langle vw \rangle / U_{ref}^2$ for experiment and CFD.

agreement between CFD and experiment for all three spanwise locations. The predicted shear-stress profiles show varying levels of agreement with the experimental data and for the most part, qualitatively capture the experimental distributions. For the $\langle vw \rangle$ shear-stress profiles in particular, the CFD generally agrees with the experimental data to within the measurement uncertainty.

In terms of the normal stresses, the observed differences between the CFD and experiment are typical of many RANS turbulence models. It should be noted, however, that the QCR2020 mod-
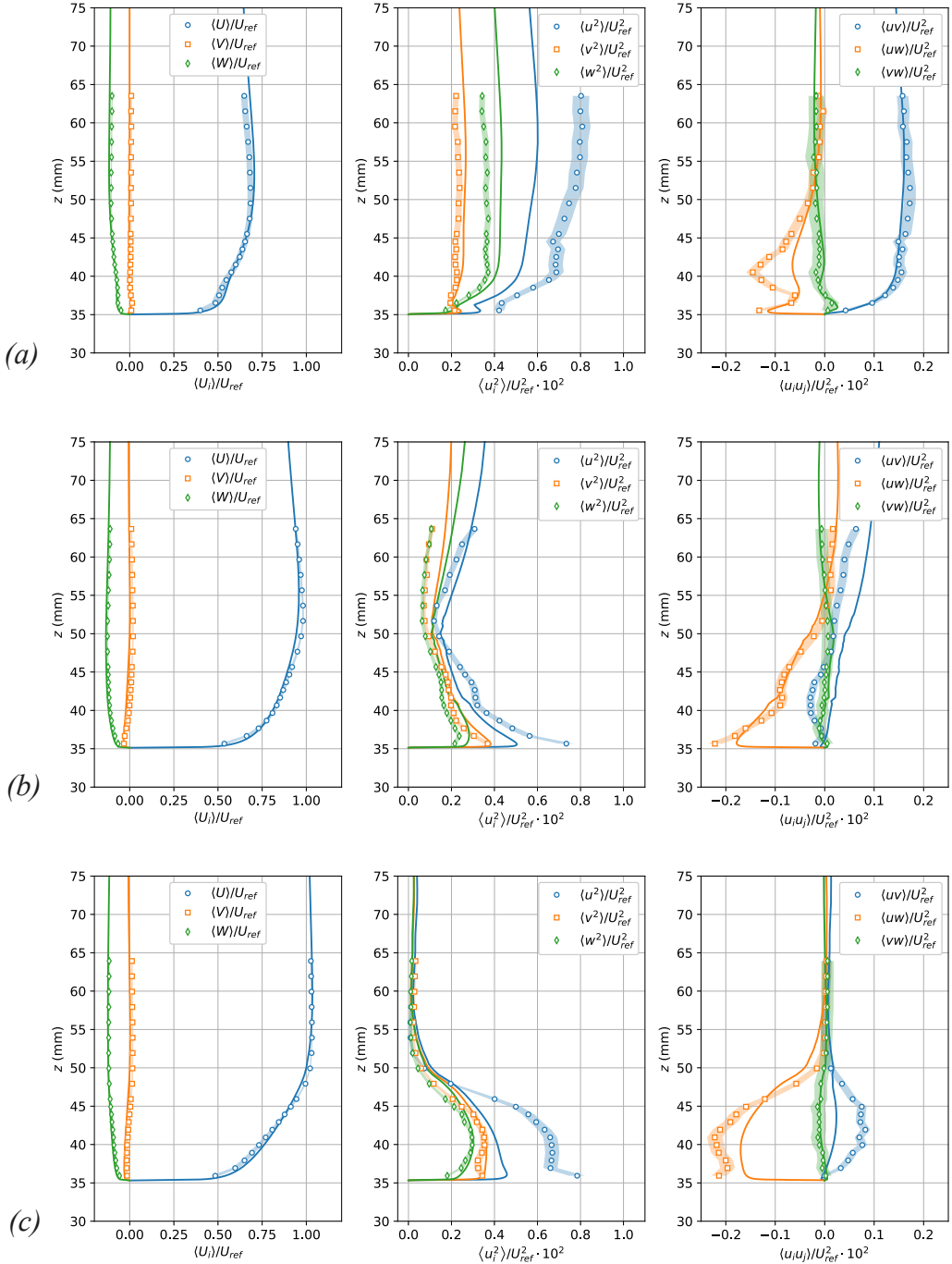
Figure 43: Measured (symbols) and computed (lines) mean-velocity and Reynolds-stress profiles at $x = 2747.6$ mm and $\alpha = 0°$. (a) $y = -237.35$ mm. (b) $y = -246.1$ mm. (c) $y = -262.1$ mm.
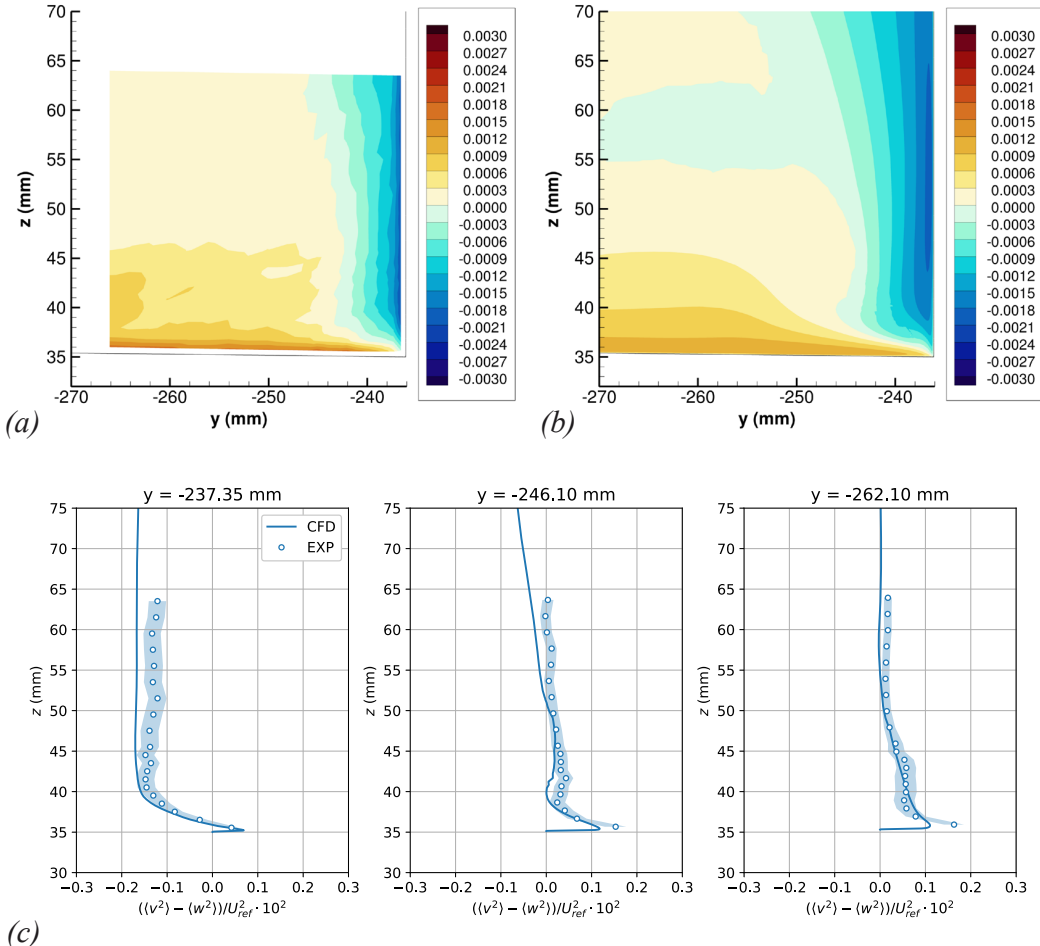
Figure 44: (*a*) Measured and (*b*) computed contours of $\left(\left\langle v^2 \right\rangle - \left\langle w^2 \right\rangle\right)/U_{ref}^2 \cdot 10^2$ for $x = 2747.6$ mm and $\alpha = 0°$. (*c*) Profiles of $\left(\left\langle v^2 \right\rangle - \left\langle w^2 \right\rangle\right)/U_{ref}^2 \cdot 10^2$ for selected y locations.

ification that was used in the present study offers significant improvements in the normal-stress predictions over earlier versions of QCR [12]. In the QCR2020 version, modifications were specifically made to obtain better predictions for the near-wall distribution of $\left\langle u^2 \right\rangle$ and, more importantly, better predictions of the separation between the secondary-flow normal stresses, $\left\langle v^2 \right\rangle - \left\langle w^2 \right\rangle$. As discussed earlier, the latter quantity—and gradients of it—relate to the production of $\left\langle \omega_x \right\rangle$ and ultimately to the strength of the stress-induced vortex. The absolute values of $\left\langle v^2 \right\rangle$ and $\left\langle w^2 \right\rangle$ are thought to play a less important role, and so the relatively small overprediction of these quantities should not be a primary concern. Even with the improvements made in QCR2020, the $\left\langle u^2 \right\rangle$ normal stress is still underpredicted. That can be important when the components of the Reynolds-stress tensor are recalculated in a rotated coordinate system as shown by Rumsey [5]. To assess how QCR2020 improves the prediction of the normal-stress anisotropy $\left\langle v^2 \right\rangle - \left\langle w^2 \right\rangle$, contour plots and profiles of that difference for experiment and CFD are shown in figure 44 for the $x = 2747.6$ mm location at $\alpha = 0°$. Here, we see that the predicted $\left\langle v^2 \right\rangle - \left\langle w^2 \right\rangle$ has a spatial distribution that is qualitatively similar to the experiment. However, as the walls of the corner are approached, there are quantitative differences, with the CFD underpredicting $\left\langle v^2 \right\rangle - \left\langle w^2 \right\rangle$. Gradients in this quantity near the walls also appear to be weaker in the CFD and that may ultimately factor into the strength

of the generated $\langle \omega_x \rangle$ and the associated stress-induced vortex.

5 Summary

In this paper, we reported on a third test campaign with the NASA Juncture Flow model in the 14x22 wind tunnel. The primary objective of that test was to expand the existing Juncture Flow CFD Validation dataset with a symmetric-wing configuration that displayed a progression from fully attached corner flow to separated corner flow near the trailing edge of the wing-fuselage junction, depending on the model angle of incidence. The newly developed dataset includes detailed LDV measurements at three model angles of incidence corresponding to fully attached corner flow ($\alpha = 0°$), incipient corner-flow separation ($\alpha = 1°$), and separated corner flow ($\alpha = 5°$). For each angle, the LDV dataset consists of profile surveys at several locations on the fuselage and y-z planar surveys at several x locations along the wing-fuselage junction. Supporting measurements in the form of model static pressures, tunnel wall static pressures, tunnel wall and ceiling boundary-layer rake pressures, oil-flow visualizations in the wing-fuselage junction region, and laser-based measurements of the as-built geometry and model position in the test section are included in the dataset. All data from the test entry are available on the NASA Langley Turbulence Modeling Resource website [10].

From the LDV measurements at $\alpha = 0°$, two key features of the turbulent corner flow were revealed. First, in the early development of the corner flow on the port side of the test article, just downstream of the wing root leading edge, a corner vortex with clockwise rotation (when looking upstream) forms. As this vortex travels downstream, it slowly migrates outboard. But even as it approaches the wing trailing edge, it remains relatively close to the corner and exerts an influence on the turbulent corner flow. Second, at a somewhat later point in the corner-flow development, a stress-induced vortex with counterclockwise rotation (when looking upstream) forms deep in the corner of the wing-fuselage junction and persists all the way to the junction trailing edge. This vortex brings momentum into the corner, reenergizes the near corner flow, and helps to keep the flow attached there as it progresses through the adverse pressure gradient imposed on the corner by the wing. The LDV measurements at $\alpha = 5°$ revealed the same two vortical flow features, but the strengthened corner vortex migrates further outboard and the corner flow separates a small distance ahead of the junction trailing edge due to the increased adverse pressure gradient imposed by the wing.

Reynolds-stress measurements in the turbulent corner flow revealed strong anisotropy in the secondary flow normal stresses $\langle v^2 \rangle$ and $\langle w^2 \rangle$, and a positive correlation for the secondary shear stress $\langle vw \rangle$ in the vicinity of the corner bisector. For turbulent corner flows, these three Reynolds-stress components are known to play an important role in the production of vorticity in the x direction, $\langle \omega_x \rangle$, and the generation of the stress induced vortex near the junction corner. RANS CFD simulations with linear eddy viscosity models cannot properly predict these Reynolds-stress components and therefore, cannot capture the stress-induced vortex. As a result, these linear models often predict corner-flow separation much earlier than what is observed from experiments.

A companion set of RANS CFD simulations with a non-linear turbulence model (SA-RC-QCR2020) were performed and were used to support the discussion of the experimental results. However, the experimental data from the test entry also serves as a blind test case for the quadratic constitutive relation QCR2020, which was explicitly modified on the basis of previous juncture-flow model test entries. Overall, this turbulence model performs very well in comparison to the experimental dataset. In terms of the model C_p distributions, the CFD was in very good quantitative agreement with the experimental data. In terms of the flowfield quantities (both mean-flow components and Reynolds stresses) the CFD was generally in very good qualitative agreement, displaying spatial distributions that were similar to the experimental data. For profiles on the fuselage, differences in the mean flow between CFD and experiment may be attributed to the way in which boundary-layer transition on the fuselage nose is imposed in the CFD. In the wing-fuselage junction region, the good qualitative agreement in both the mean-flow components and the Reynolds stresses suggests that the

turbulence model is capturing the essential flow physics. In particular, both the corner vortex and the stress-induced vortex are predicted by the CFD. However, quantitative differences between the CFD and the experimental data do exist. The CFD consistently underpredictes the $\langle u^2 \rangle$ component and overpredicts the $\langle v^2 \rangle$ and $\langle w^2 \rangle$ components in all the measurement locations considered. For the fuselage boundary layer, these mispredictions may not be too critical, but they are more important in the wing-fuselage corner-flow region. There, gradients in the difference $\langle v^2 \rangle - \langle w^2 \rangle$ contribute to the production of mean x-component vorticity, $\langle \omega_x \rangle$. As such, a misprediction in that quantity will affect the strength of the secondary flow. That is particularly important deep in the corner where the resulting stress-induced vortex plays a key role in the onset of corner-flow separation. In fact, the predicted secondary flow in the corner was found to be somewhat weaker than the experimental data and that may explain why the CFD predicts a small corner-flow separation for all angles of incidence that were considered, while the experimental data indicates corner-flow separation only for angles of incidence larger than $\alpha = 1°$.

Acknowledgements

Data Availability

The experimental data presented in this report are available at the NASA Langley Research Center Turbulence Modeling Resource website [10].

References

1. Mauery, T.; Alonso, J.; Cary, A.; Lee, V.; Malecki, R.; Mavriplis, D.; Medic, G.; Schaefer, J.; and Slotnick, J.: A Guide for Aircraft Certification by Analysis. NASA CR 20210015404, May 2021.

2. Rumsey, C. L.; Neuhart, D. H.; and Kegerise, M. A.: The NASA Juncture Flow Experiment: Goals, Progress, and Preliminary Testing. AIAA Paper 2016-1557, January 2016.

3. Kegerise, M. A.; and Neuhart, D. H.: An Experimental Investigation of a Wing-Fuselage Junction Model in the NASA Langley 14- by 22-Foot Subsonic Tunnel. NASA TM 2019-220286, June 2019.

4. Kegerise, M. A.; Neuhart, D. H.; Hannon, J. A.; and Rumsey, C. L.: An Experimental Investigation of a Wing-Fuselage Junction Model in the NASA Langley 14- by 22-Foot Subsonic Wind Tunnel. AIAA Paper 2019-0077, January 2019.

5. Rumsey, C. L.; Ahmad, N. N.; Carlson, J. R.; Kegerise, M. A.; Neuhart, D. H.; Hannon, J. A.; Jenkins, L. N.; Yao, C. S.; Balakumar, P.; Gildersleeve, S.; Bartarm, S. M.; Pulliam, T. H.; Olsen, M. E.; and Spalart, P. R.: NASA Juncture Flow Computational Fluid Dynamics Validation Experiment. *AIAA Journal*, vol. 60, no. 8, 2022, pp. 4789–4805.

6. Taylor, N. J.; and Rumsey, C. L.: CFD Validation Experiments: Toward a Broader Perspective. AIAA Paper 2021-1933, January 2021.

7. Brodersen, O.; and Stürmer, A.: Drag Prediction of Engine-Airframe Interference Effects Using Unstructured Navier-Stokes Calculations. AIAA Paper 2001–2414, June 2001.

8. Jenkins, L. N.; Yao, C. S.; and Bartram, S. M.: Flow-Field Measurements in a Wing-Fuselage Junction Using an Embedded Particle Image Velocimetry System. AIAA Paper 2019-0078, January 2019.

9. Rumsey, C. L.; Carlson, J. R.; Hannon, J. A.; Jenkins, L. N.; Bartram, S. M.; Pulliam, T. H.; and Lee, H. C.: Boundary Condition Study for the Juncture Flow Experiment in the NASA Langley 14x22-Foot Subsonic Wind Tunnel. AIAA Paper 2017-4126, June 2017.

10. Rumsey, C. L.: NASA Langley Turbulence Modeling Resource Website. `https://turbmodels.larc.nasa.gov` Accessed: 2023-05-09.

11. Perkins, H. J.: The Formation of Streamwise Vorticity in Turbulent Flow. *Journal of Fluid Mechanics*, vol. 44, 1970, pp. 721–740.

12. Rumsey, C. L.; Carlson, J. R.; Pulliam, T. H.; and Spalart, P. R.: Improvements to the Quadratic Constitutive Relation Based on NASA Juncture Flow Data. *AIAA Journal*, vol. 58, no. 10, October 2020, pp. 4374–4384.

13. Kuester, M. S.; Borgoltz, A.; and Devenport, W. J.: Experimental Visualization of Juncture Separation Bubbles at Low- to Moderate-Reynolds Numbers. AIAA Paper 2016-3880, June 2016.

14. Kegerise, M. A.; and Neuhart, D. H.: Wind Tunnel Test of a Risk-Reduction Wing/Fuselage Model to Examine Juncture-Flow Phenomena. NASA TM 219348, 2016.

15. Leidy, A. N.; Kegerise, M. A.; Hannon, J. A.; Choudhari, M.; Venkatachari, B.; and Paredes, P.: Measurements and Computations of Natural Transition on the NASA Juncture-Flow Model with a Symmetric Wing. AIAA Paper 2023-0441, January 2023.

16. Gentry, G. L.; Quinto, F. P.; Gatlin, G. G.; and Applin, Z. T.: The Langley 14- by 22-Foot Subsonic Tunnel. NASA TP 3008, 1990.

17. Neuhart, D. H.; and McGinley, C. B.: Free-Stream Turbulence Intensity in the Langley 14- by 22-Foot Subsonic Tunnel. NASA TP 213247, 2004.

18. Quinto, F. P.; and Boney, A. D.: Dynamic Pressure Equations Used at the 14- by 22-Foot Subsonic Tunnel. NF 1676l-32662, 2019.

19. Finley, T.; and Tcheng, P.: Model Attitude Measurements at NASA Langley Research Center. AIAA Paper 92-0763, January 1992.

20. Carlson, J. R.: In Pursuit of CFD-based Wind Tunnel Calibrations. AIAA Paper 2024–2136, January 2024.

21. Lowe, K. T.: Design and Application of a Novel Laser-Doppler Velocimeter for Turbulence Structural Measurements in Turbulent Boundary Layers. PhD thesis, Virginia Polytechnic Institute and State University, Blacksburg, VA, September 2006.

22. Lowe, K. T.; and Simpson, R. L.: An Advanced Laser-Doppler Velocimeter for Full-Vector Particle Position and Velocity Measurements. *Meas. Sci. Technol.*, vol. 20, 2009, pp. 1–16.

23. Brooks, D. R.; and Lowe, K. T.: Development and Application of a Compact Spatially Resolving Vector Laser Velocimeter for Near Surface Flow Measurements. *16th Int. Symp. on Applications of Laser Techniques to Fluid Mechanics*, Lisbon, Portugal, 2012.

24. Ölçmen, S. M.; and Simpson, R. L.: An Experimental Study of a Three-Dimensional Pressure-Driven Turbulent Boundary Layer. *Journal of Fluid Mechanics*, vol. 290, 1995, pp. 225–262.

25. Albrecht, H. E.; Borys, M.; Damaschke, N.; and Tropea, C.: *Laser Doppler and Phase Doppler Measurement Techniques*. Springer, Berlin, Germany, 2003.

26. Aeschliman, D. P.; and Oberkampf, W. L.: Experimental Methodology for Computational Fluid Dynamics Code Validation. *AIAA Journal*, vol. 36, no. 5, May 1998, pp. 733–741.

27. Anderson, W.; and Bonhaus, D.: An Implicit Upwind Algorithm for Computing Turbulent Flows on Unstructured Grids. *Computers and Fluids*, vol. 23, no. 1, 1994, pp. 1–22.

28. Anderson, W.; Rausch, R.; and Bonhaus, D. L.: Implicit/Multigrid Algorithms for Incompressible Turbulent Flows on Unstructured Grids. *Journal of Computational Physics*, vol. 128, 1996, pp. 391–408.

29. Roe, P. L.: Approximate Riemann Solvers, Parameter Vectors, and Difference Schemes. *Journal of Computational Physics*, vol. 43, 1981, pp. 357–372.

30. FUN3D User's Manual. `https://fun3d.larc.nasa.gov` Accessed: 2022-08-25.

31. Rumsey, C. L.; Lee, H. C.; and Pulliam, T. H.: Reynolds-Averaged Navier-Stokes Computations of the NASA Juncture Flow Model Using FUN3D and OVERFLOW. AIAA Paper 2020-1304, January 2020.

32. Ahmad, N. N.; Rumsey, C. L.; and Carlson, J. R.: In-Tunnel Simulations of the NASA Juncture Flow Model. AIAA Paper 2021-1428, January 2021.

33. Spalart, P. R.; and Allmaras, S. R.: A One-Equation Turbulence Model for Aerodynamic Flows. *Recherche Aerospatiale*, vol. 1, 1994, pp. 5–21.

34. Shur, M. L.; Strelets, M. K.; Travin, A. K.; and Spalart, P. R.: Turbulence Modeling in Rotating and Curved Channels: Assessing the Spalart-Shur Correction. *AIAA Journal*, vol. 38, no. 5, 2000, pp. 784–792.

35. Fernholz, H. H.; and Finley, P. J.: The Incompressible Zero-Pressure-Gradient Turbulent Boundary Layer: An Assessment of the Data. *Progress in Aerospace Sciences*, vol. 32, 1996, pp. 245–311.

36. Musker, A. J.: Explicit Expression for the Smooth Wall Velocity Distribution in a Turbulent Boundary Layer. *AIAA Journal*, vol. 17, no. 6, June 1979, pp. 655–657.

37. Coles, D. E.: The Turbulent Boundary Layer in a Compressible Flow. RAND Report R-403-PR, September 1962.

38. Tobak, M.; and Peake, D. J.: Topology of Three-Dimensional Separated Flows. *Annual Review of Fluid Mechanics*, vol. 14, 1982, pp. 61–85.

39. Eibeck, P. A.; and Eaton, J. K.: Heat Transfer Effects of a Longitudinal Vortex Imbedded in a Turbulent Boundary Layer. *Journal of Heat Transfer*, vol. 109, 1987, pp. 16–24.

40. Lee, S. H.; Ryou, H. S.; and Choi, Y. K.: Heat Transfer in a Three-Dimensional Turbulent Boundary Layer with Longitudinal Vortices. *International Journal of Heat and Mass Transfer*, vol. 42, 1999, pp. 1521–1534.

41. Hazarika, B. K.; Raj, R.; and Boldman, D. R.: Three-Dimensional Fluid Flow Phenomena in the Blade End Wall Corner Region. *International Journal of Turbo and Jet Engines*, vol. 6, no. 3–4, 1989, pp. 311–326.

42. Bordji, M.; Gand, F.; Deck, S.; and Brunet, V.: Investigation of a Nonlinear Reynolds-Averaged Navier-Stokes Closure for Corner Flows. *AIAA Journal*, vol. 54, no. 2, February 2016, pp. 386–398.

43. Westphal, R. V.; Eaton, J. K.; and Pauley, W. R.: Interaction Between a Vortex and a Turbulent Boundary Layer in a Streamwise Pressure Gradient. 5th International Symposium on Turbulent Shear Flows, Cornell University, Ithaca, NY, 1985.

44. Pope, S. B.: *Turbulent Flows*. Cambridge, Cambridge, United Kingdom, 2000.